Electronic Properties of Assemblies of ZnO Quantum Dots

Electronic Properties of Assemblies of ZnO Quantum Dots

Elektronische eigenschappen van lagen van ZnO nanokristallen

(met een samenvatting in het Nederlands)

Proefschrift

ter verkrijging van de graad van doctor aan de Universiteit Utrecht op gezag van de Rector Magnificus, prof. dr. W. H. Gispen, ingevolge het besluit van het College voor Promoties in het openbaar te verdedigen op woensdag 4 juni 2003 des middags te 2.30 uur

door

Aarnoud Laurens Roest

geboren op 26 maart 1976, te Amersfoort

Promotores: Prof. dr. J.J. Kelly
Prof. dr. D. Vanmaekelbergh

Faculteit Scheikunde
Debye Instituut, Universiteit Utrecht

CIP-GEGEVENS KONINKLIJKE BIBLIOTHEEK, DEN HAAG

Roest, Aarnoud Laurens

Electronic properties of assemblies of ZnO quantum dots
(Elektronische eigenschappen van lagen van ZnO nanokistallen)
Aarnoud Laurens Roest, Utrecht: Universiteit Utrecht,
Physics and Chemistry of Condensed Matter, Debye Instituut.
Proefschrift Universiteit Utrecht. Met een samenvatting in het Nederlands.
ISBN 90-393-3324-6

This research has been financially supported by the Council for Chemical Sciences of the Netherlands Organization for Scientific Research (CW-NWO) .

Contents

Chapter 1

Semiconductor nanostructures

This thesis deals with electron transport in porous semiconductors interpenetrated with an electrolyte solution. Porous semiconductors are interesting because they possess a high surface to bulk ratio. Porous semiconductors permeated with an electrolyte solution have thus a three dimensional interface, and thus a huge capacitance. The porous semiconductor systems are obtained by making assemblies of zinc oxide nanocrystals. If the size of these nanocrystals is in the order of magnitude of the electron or hole wave function or the Bohr-radius, quantum confinement starts to play a role. The confinement of the electron wave functions in a nanocrystal (size quantization) is the origin of a lot of interesting phenomena discussed in this thesis. For example, quantum confinement leads to discrete energy levels instead of bands. The porous quantum-dot assembly can be filled with an electrolyte and used as an electrode in an electrochemical experiment. Electrons can be injected into such an assembly by changing the electrochemical potential. The electrons occupy the delocalized atom-like conduction orbitals. This determines the optical and electrical properties of the ZnO quantum-dot assembly. The nature of the interpenetrating electrolyte solution is important for the degree of screening of the charge of the electrons. The luminescence and absorption change dramatically with the electron occupation. In the last chapter, we consider electron transport in macroporous gallium phosphide. GaP is made porous by (photo)anodic etching. This leads to a porous semiconductor with structural units in the 100 nm range, thus without measurable quantum confinement effects. In GaP the photoinduced charge transport is investigated by the time-resolved photoelectrochemical technique, intensity-modulated photocurrent spectroscopy.

1.1 Introduction

Semiconductors are important building blocks for a scala of (opto)electrical applications. Illumination of a semiconductor with photons with an energy larger than the band gap creates electrons and holes. The separation of photogenerated charge carriers by the electric field of a space-charge region of a semiconductor junction and the subsequent transfer of charge across the junction form the basis for a number of important applications in device technology. The Schottky diode, used as a photodiode or solar cell, is an important example [1].

Porous semiconductors permeated with an electrolyte solution can be used to convert light into electrical energy [2–5]. By making semiconductors porous in a top-down approach by (photo)chemical etching, new interesting effects were found such as an increased photocurrent quantum yield in macroporous *n*-GaP [6]. In a bottom-up approach porous structures can be made by deposition of semiconductor nanocrystals. An important application of this is the dye-sensitized TiO_2 solar cell which may be an interesting alternative for the more expensive silicon-based solar cells [2].

In this work ZnO nanocrystals were investigated. These nanocrystals are so small that quantum size-confinement starts to play an important role; therefore, such nanocrystals are also called quantum dots. The energy bands characteristic of macroscopic semiconducting materials disappear and discrete levels appear. The quantum size effects play an important role in the transport of electrons through assemblies of quantum dots. The energy of the conduction levels depend on the size of the dots. There is a dispersion in the size of the quantum dots in our assemblies and, therefore, a dispersion in the position of the energy levels. Another important effect is Coulomb blockade. The quantum dot is negatively charged if electrons are added and these electrons will repel each other. Transport can become thermally activated if the Coulomb-blockade effect is large enough.

The absorption and luminescence properties in an assembly depend on the electron occupation of the quantum dots. Discrete conduction energy levels filled with electrons cannot be involved in optical transitions of electrons excited from the valence band; the absorption of ultraviolet light thus decreases. The electrons in these energy levels, however, can be excited to higher conduction energy levels by absorption of infrared light.

GaP is made porous by (photo)anodic etching. This leads to a porous semiconductor without quantum confinement effects. Porous GaP is a very efficient photodiode. The electrons which are generated by light absorption on one side of the GaP network have to travel through the porous layer to the back contact.

We investigated long-range transport of electrons through a porous GaP network with a time-resolved photoelectrochemical technique; i.e. intensity-modulated photocurrent spectroscopy.

1.2 Electrons in bulk semiconductor crystals

To discuss the origin of energy bands in bulk semiconductors a single electron in a crystal is considered. The time-independent Schrödinger equation for a *free electron* can be written as:

$$-\frac{\hbar^2}{2m_0}\nabla^2\Psi(x,y,z) = E\Psi(x,y,z) \tag{1.1}$$

Here m_0 is the mass of the free electron, E is the kinetic energy, and $\nabla^2 = (\frac{\partial^2}{\partial x^2} + \frac{\partial^2}{\partial y^2} + \frac{\partial^2}{\partial z^2})$. The solution of Equation 1.1 for Ψ is given by:

$$\Psi_{\mathbf{k}}(\mathbf{r}) = \frac{1}{\sqrt{V}}e^{i\mathbf{k}\cdot\mathbf{r}} \tag{1.2}$$

Here $\mathbf{r}$ is the position vector (x, y, z), and $\mathbf{k}$ the wave-vector (k_x, k_y, k_z). The prefactor $\frac{1}{\sqrt{V}}$ is due to the normalization condition, which requires that the particle must be present in the sample volume V. The linear momentum of the electrons is $\mathbf{p} = \hbar\,\mathbf{k}$ and the kinetic energy is given by [7]:

$$E(\mathbf{k}) = \frac{\hbar^2 k^2}{2m_0} \tag{1.3}$$

In a *crystal*, electrons interact with core ions. This is described by a potential $U(\mathbf{r})$. Because of the periodicity of the lattice, $U(\mathbf{r} + \mathbf{R}) = U(\mathbf{r})$ for each vector $\mathbf{R}$ between two lattice points. The electron energy levels in a crystal can often be described by a nearly-free electron model for which the periodic potential of the ion cores represents only a weak perturbation. Figure 1.1 shows a plot of the energy versus wave vector for an electron in a linear lattice of lattice constant a.

For a wave vector $k = \pm\pi/a$, the curve splits up. The energy levels are arranged in bands separated by regions in energy for which there are no solutions of the Schrödinger equation. Such forbidden regions are called band gaps. The physical reason for the band gap is Bragg scattering at the lattice for wave functions with a wave vector:

$$k = \pm n\pi/a \tag{1.4}$$

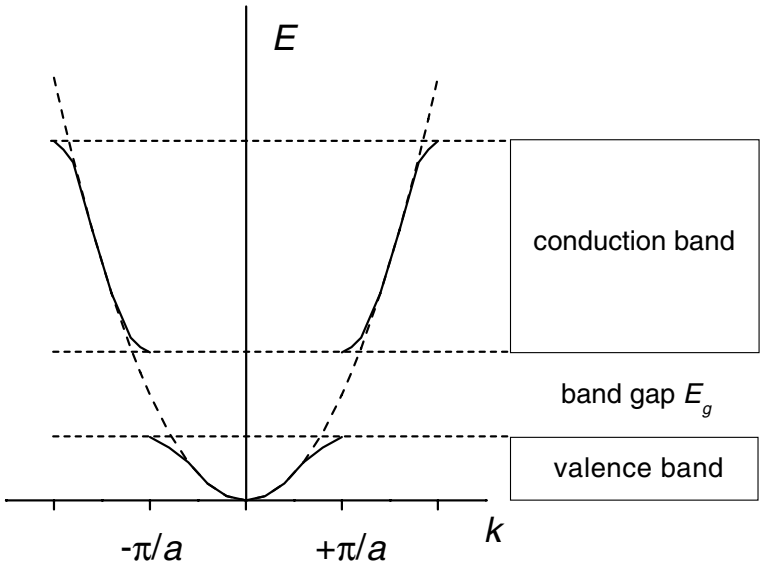

Figure 1.1: Schematic plot of the energy E versus the wave vector k for an electron in a linear lattice of lattice constant a. If the lowest band is completely filled with electrons and the second band empty, this material would be a semiconductor or insulator. The filled band is called the valence band and the empty band the conduction band. The energy gap or the band gap, E_g, is associated with the first Bragg reflection at $k = \pm\pi/a$.

Here n is an integer. If a band is partially filled, the material would be a metal. If a band is completely filled with electrons and the following band is empty the material is a semiconductor or insulator. The filled band is then called the valence band and the empty band the conduction band. These two bands are now separated by a forbidden zone, the band gap with an energy E_g.

The probability that an energy level E is occupied by an electron is given by the Fermi-Dirac function:

$$f(E) = \frac{1}{1 + e^{(E-\mu_e)/k_B T}} \tag{1.5}$$

Here μ_e is the electrochemical potential (Fermi-level) and k_B the Boltzmann constant. The electrical transport properties of a semiconductor are completely determined by the electrons at the bottom of the conduction band and the holes at the top of the valence band, since only these charge carriers can move to empty states with a similar energy.

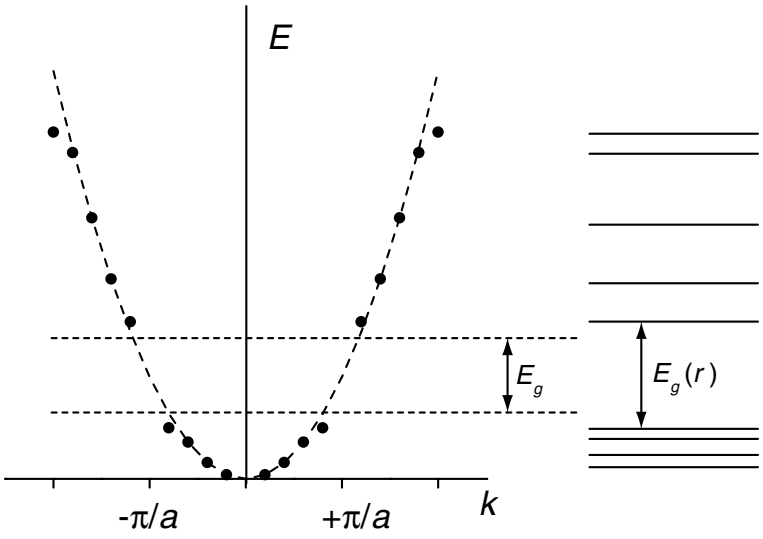

Figure 1.2: Schematic plot of the energy E versus the wavevector k for an electron in a semiconductor nanocrystal with diameter $2r$. The band gap of the macroscopic semiconductor and the nanocrystal are indicated.

In a semiconductor crystal, the Fermi level with an energy E_F lies in the band gap. At low temperatures, the valence band is completely filled with electrons and the conduction band is completely empty. At higher temperatures, the lower levels in the conduction band become occupied with electrons by thermal activation, leaving empty states at the top of the valence band.

Atoms or dangling bonds at the surface of a crystal can have energy levels in the band gap. Trapping of free carriers in such surface states can lead to a depletion layer characterized by a potential barrier (see Section 1.7). In particular, surface states with an energy close to the Fermi-level E_F can act as traps for charge carriers, reducing their mobility.

1.3 Quantum size effects

The first part of this thesis deals with ZnO layers formed from colloidal ZnO nanocrystals. In these small crystals with a diameter between 3 and 6 nanometer, the energy levels are affected by *quantum confinement*.

A (Wannier) exciton can be defined as the bound state of an electron-hole pair, which is due to a Coulomb interaction between the charge carriers [8]. The

distance between the electron and the hole is the Bohr radius of the exciton a_B and is given by:

$$a_B = \frac{4\pi\varepsilon_0\varepsilon_\infty\hbar^2}{m_0 e^2}\left(\frac{1}{m_e^*} + \frac{1}{m_h^*}\right) \tag{1.6}$$

Here m_e^* and m_h^* are the effective electron and hole masses, respectively, and ε_∞ the high-frequency relative dielectric constant of the medium. The resulting Bohr radius is much larger than that of a hydrogen atom, since the effective masses are considerably smaller than the mass of the free electron m_0 and ε_∞ is considerably larger than 1. Values for a_B for the common semiconductors are in the range of 1-10 nm.

Confinement of an electron in a crystalline material with nanometer dimensions requires that its wave function vanishes outside the crystallite. Due to quantum size-confinement the electron energy levels are considerably separated in energy and the crystallite is called a quantum dot. As an example, for an electron confined in a cube with side L, the only wave functions $e^{i\mathbf{k}\cdot\mathbf{r}}$ which comply with the boundary condition are characterized by $k_i = \frac{n_i\pi}{L}\ \ (i = x, y, z)$ where n_i is an integer. These discrete wave vectors $\mathbf{k}$ correspond to discrete energy levels:

$$E = \frac{\hbar^2(k_x^2 + k_y^2 + k_z^2)}{2m_0} \tag{1.7}$$

The energy levels can be represented by discrete points on the (E, k) surface. A one-dimensional representation is given in Figure 1.2.

Brus has modelled electron confinement in a spherical box by using the effective mass approximation [9, 10]. This leads to an expression for the energy difference between the first electron and hole level (the HOMO-LUMO single-particle gap) of a nanocrystal with radius r:

$$E_g(r) = E_g(r \to \infty) + \frac{\pi^2\hbar^2}{2m_0 r^2}\left(\frac{1}{m_e^*} + \frac{1}{m_h^*}\right) \tag{1.8}$$

The first term is just the macroscopic band gap and the second term describes the confinement. Equation 1.8 is valid for a quantum dot without electrons, holes or excitons. The optical band gap, however, will differ from the single-particle gap due to dielectric polarization of the dot (and surroundings) by the charge of the electron and hole, and the electron-hole charge interaction. Using the model proposed by Zunger, the optical gap can be written as [11]:

$$E_g^{opt}(r) = E_g(r \to \infty) + \frac{\pi^2\hbar^2}{2m_0r^2}(\frac{1}{m_e^*} + \frac{1}{m_h^*}) + (E_e^{pol} + E_h^{pol} - J_{e,h}) \qquad (1.9)$$

Here E_e^{pol} is the self-polarization of the electron and E_h^{pol} that of the hole; both depend on the dielectric constants of the quantum dot ϵ_{dot} and the surrounding medium ϵ_{out}. $J_{e,h}$ is the Coulomb interaction between the electron and the hole. The three terms between brackets almost cancel [11]. The result is that the *optical* gap $E_g^{opt}(r)$ is close to the single-particle band gap and almost independent of ϵ_{dot} and ϵ_{out}. This strongly contrasts with the zero-conductivity gap E_g^{stm} or quasi-particle gap measured by scanning tunnelling microscopy (STM) for single charge carriers [12]:

$$E_g^{stm}(r) = E_g(r \to \infty) + \frac{\pi^2\hbar^2}{2m_0r^2}(\frac{1}{m_e^*} + \frac{1}{m_h^*}) + E_e^{pol} + E_h^{pol} \qquad (1.10)$$

The difference between the optical and quasi-particle gap gives the electron-hole attraction energy $J_{e,h}$. Such measurements were performed for the first time with CdSe quantum dots [12]. The increase of the band gap and the transition from continuous energy bands to discrete energy levels upon a decrease of particle size (see Figure 1.2) has been observed by optical absorption spectroscopy in many colloidal semiconductor systems [13, 14].

The discrete levels of quantum dots can be observed directly in a so-called shell-tunnelling experiment. In Figure 1.3 the result is shown for a resonant tunnelling experiment on a CdSe quantum dot [12]. The electron and hole levels of the quantum dot are measured directly with a STM. The quantum dot is attached to a conducting gold substrate and the tip of the STM is used as the second contact. The conditions are chosen such that the rate of electron transfer from the dot to the electrode is faster than that of electron transfer from the tip to the dot (i.e. $\Gamma_{out} > \Gamma_{in}$). In this way the quantum dot is not charged and electron tunnelling from the tip to the dot can occur if the Fermi level of the tip (E_F^{tip}) is resonant with an electron or hole level in the quantum dot. Each electron and hole level is observed as a peak in the conductance spectrum (i.e. $dI/d\Delta\mu$ versus $\Delta\mu$ where $\Delta\mu$ is $\mu_{e,tip} - \mu_{e,substrate}$).

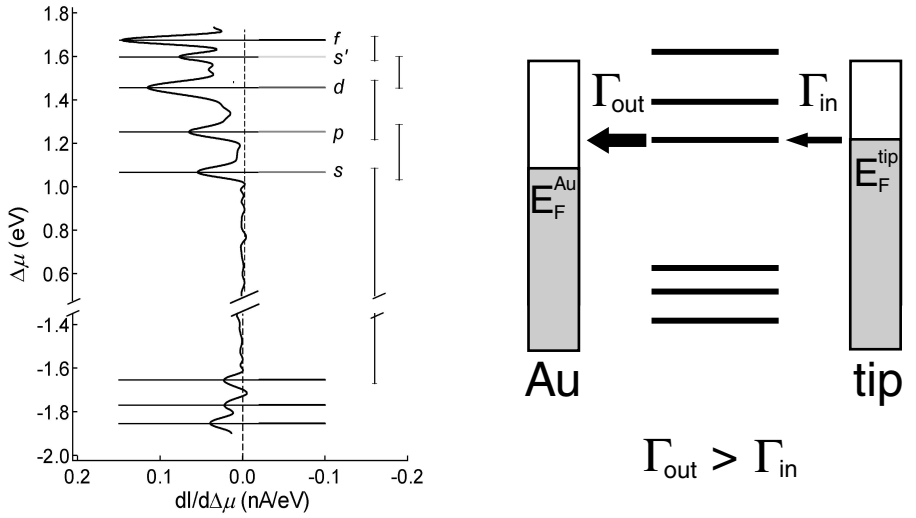

Figure 1.3: The energy levels which are observed in a resonant tunnelling experiment on a CdSe quantum dot (Bakkers et al. [12]). For resonant shell-tunnelling electron transfer from the dot to the electrode has to be faster than electron transfer from the tip to the dot (i.e. $\Gamma_{out} > \Gamma_{in}$. Electron tunnelling from tip-to-dot can occur if the Fermi level of the tip (E_F^{tip}) is resonant with an electron or hole level in the quantum dot. Each electron and hole level is observed as a peak in the $dI/d\Delta\mu$ versus $\Delta\mu$ diagram.

1.4 Quantum-dot assemblies and Coulomb repulsion

In this work we consider assemblies of quantum dots, also called quantum-dot solids, consisting of about 10^{15} nanocrystals. In such an assembly there will always be a dispersion in the size of the quantum dots. Consequently there will also be a dispersion in the energy of the levels in the quantum dots. The effect of this is schematically shown in Figure 1.4. The dispersion in the size of the quantum dots and therefore the dispersion in the energy increases from the lower to the upper part of the figure. Peaks are observed with an area ratio of 2:6:10 corresponding to the two-fold degenerate *S* level, the six-fold degenerate *P* level and the ten-fold degenerate *D* level. In the case of size dispersion, the relative magnitude of the surfaces under the curves is still the same. The density of states of the quantum dot can be measured by the electron capacitance in an electrochemical charging experiment as is described in Chapter 2. The electrochemical potential of a ZnO quantum-dot assembly is changed with respect to a reference potential and the ZnO assembly equilibrates by accepting electrons in the conduction energy lev-

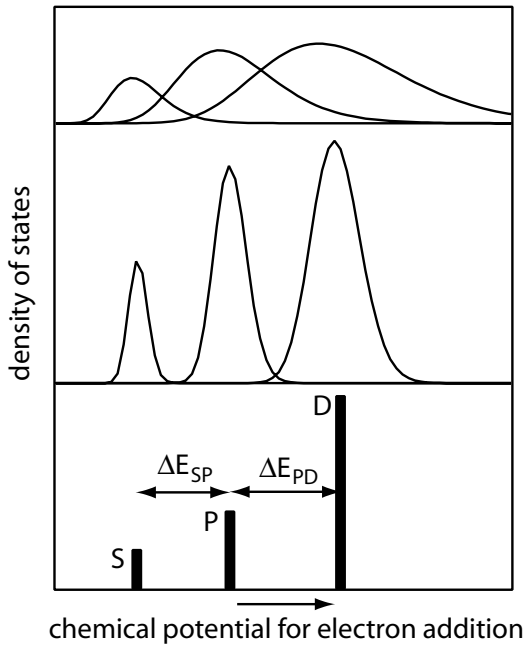

Figure 1.4: The influence of size dispersion on the distribution of the energy levels. There is an increase in the size dispersion on going from the lower to the top figure.

els.

In the previous discussion we disregarded Coulomb repulsion between the electrons in the quantum dot. If there is Coulomb repulsion, the energy to add a second electron will be increased by one electron-electron interaction energy (ΔE_{ee}). If there is no size dispersion this will lead to single-electron energy levels as shown in Figure 1.5. The two *S* levels and the six *P* levels are now separated by the electron-electron repulsion energy. The distance between the second *S* level and the first *P* level is now ΔE_{SP} + ΔE_{ee}. In the upper part of Figure 1.5 the situation is shown for quantum dots with a small distribution in size. The *S* and *P* energy level distributions have now become much broader in energy compared to Figure 1.4.

1.5 Electron transport in ZnO quantum-dot assemblies

In a completely monodisperse assembly of ZnO quantum dots electron transport from dot to dot would be resonant. With an increasing occupation of the energy

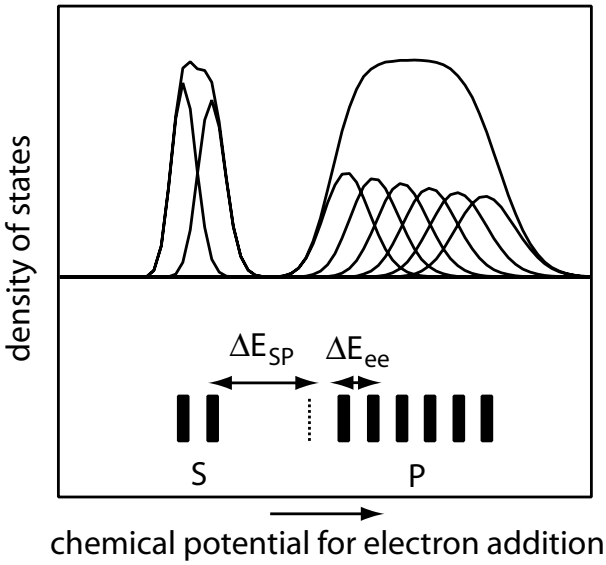

Figure 1.5: The influence of electron-electron interaction on the charging characteristic of a quantum-dot assembly. The single-electron energy levels are now separated by the electron-electron interaction energy ΔE_{ee}. Fewer electrons can now be stored in the same range of chemical potential.

levels the assembly would alternate between conducting and insulating states depending on the number of electrons in the energy levels. This is equivalent to the resonant tunnelling experiment on a single dot. For coherent transport the overlap of the quantum dot orbitals must be very strong. In the assemblies studied here, transport is *non-coherent*; i.e. occurring by a sequence of tunnelling events between adjacent quantum dots [15].

The ZnO quantum dots used for the assemblies in this work are not monodisperse; this results in a dispersion in the energy of the electron levels. There will, therefore, always be a mismatch between the energy levels of two adjacent quantum dots. Because of the energy mismatch, the electron travelling through the quantum-dot assembly will gain or lose some energy in each transfer step. If this energy difference ΔE is smaller than $k_B T$ (which is 25 meV at room temperature) electron transport is almost resonant, and the temperature dependence of electron transport will be very weak.

Another effect which can play an important role in non-coherent transport

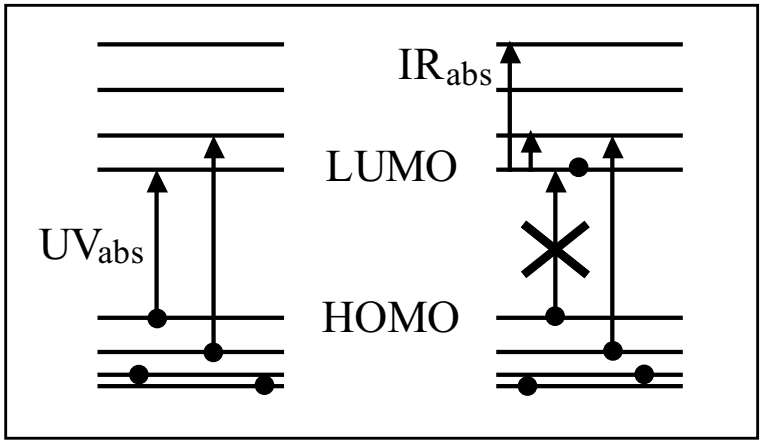

Figure 1.6: The influence of the filling of the single-electron energy levels with electrons on the UV and IR absorbance of ZnO quantum dots. If the quantum dot is neutral (left), UV-absorbance is observed due to the HOMO-LUMO transition. Higher energy transitions are also possible. If the LUMO is occupied with one electron, the HOMO-LUMO transition is quenched but the higher energy transitions are still allowed. Additionally, an IR transition is possible between the completely filled LUMO and higher energy levels.

is the *Coulomb-blockade* effect which is due to the electrostatic charging of a quantum dot in the assembly. In studies of electron transport in assemblies of molecules and quantum dots, Coulomb blockade leads to a temperature dependence of the electron mobility [15–18]. The chemical potential to add an electron to an energy level ε_N in a quantum dot containing N-1 conduction electrons is:

$$\mu_N = \varepsilon_N + (2N - 1)\Sigma \tag{1.11}$$

Here Σ is given by $\frac{e^2}{2C_{dot}}$ (C_{dot} is the capacitance of a quantum dot in the assembly).

1.6 UV and IR absorbance by ZnO quantum dots

In this section we will briefly discuss the effect of the filling of the single-electron energy levels of (ZnO) quantum dots with electrons on the absorbance of ultraviolet (UV) and infrared (IR) light. In Figure 1.6 the single-electron energy levels of a quantum dot are shown schematically. For simplicity, we assume that each level can only be occupied by one electron. We discuss the situation in which

the quantum dot has no electron (left) or a single electron (right) in a conduction level. If the conduction levels of the quantum dot are unoccupied, photons can be absorbed with the energy of the HOMO-LUMO and higher energy transitions. The band gap of ZnO is 3.2 eV and therefore the HOMO-LUMO absorption is in the UV part of the spectrum. If an electron is added to the neutral quantum dot, the LUMO will be occupied with this electron. The HOMO-LUMO transition is completely quenched. With an electron in the LUMO a transition can be made from the LUMO to higher-lying electron energy levels. The energy separations are typically in the order of 250 meV which is in the near IR. More UV transitions will be quenched and more IR transitions become possible if additional electrons are added to the quantum dot. The optical properties of charged ZnO quantum dots (i.e. artificial atoms) are the subject of Chapter 4 in this thesis.

1.7 *n*-Type GaP

In Chapter 6 we consider a porous *n*-type GaP semiconductor with structure dimensions of about 150 nm. This is not a size-quantized system; the conduction electron energy levels are described by the bulk energy bands. The porous GaP material is used as an electrode in (opto)electrochemical experiments. GaP is immersed in an electrolyte which permeates the porous structure.

The current-potential curves of an *n*-type GaP electrode in an electrochemical cell with a 0.5 M H_2SO_4 electrolyte solution are shown in Figure 1.7. The junction displays typical diode characteristics: in the dark, a cathodic current which depends exponentially on the applied potential U is measured if $U <$ -0.85 V (I in Figure 1.7), and practically no current is measured in the potential range where $U >$ - 0.85 V (II). In the latter potential range, an anodic photocurrent is measured under illumination (III).

The diode characteristics of the semiconductor/electrolyte interface may be understood in terms of the band diagrams drawn in the lower part of Figure 1.7. In contrast to metal electrodes, changes in the potential applied to a semiconductor generally cause the electric field to vary on the solid state side of the interface. This affects the bending of the bands near the surface. The surface concentration of conduction band electrons, the majority charge carriers in an *n*-type material, depends strongly on the band bending. At potentials close to the flat-band potential U_{fb} (I), the concentration of electrons at the surface is high, so that electron transfer to the solution takes place and a cathodic current is measured; generally, when the electrolyte is aqueous, hydrogen gas evolves. At more positive poten-

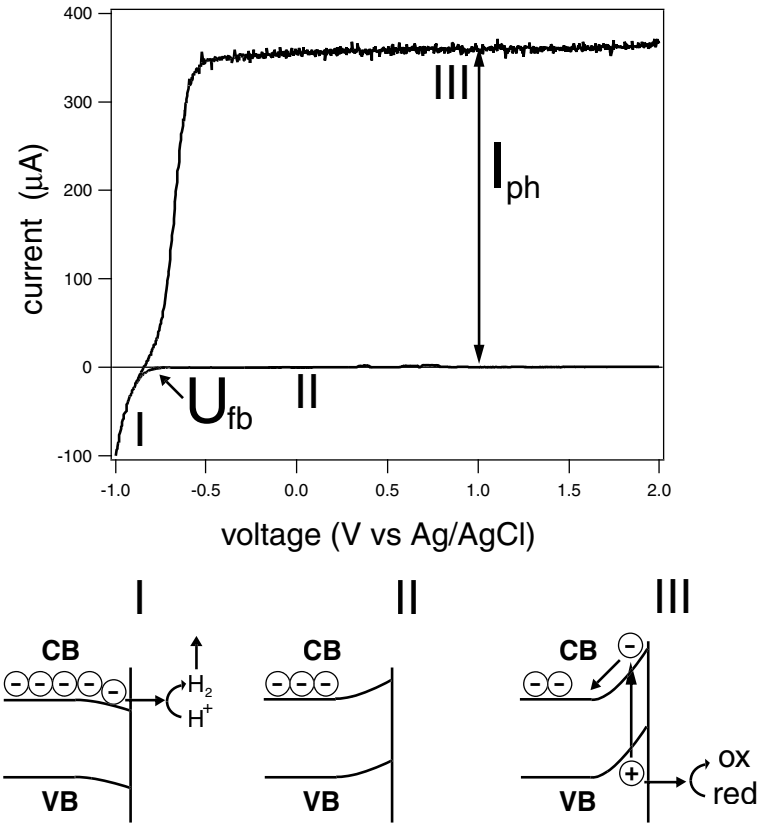

Figure 1.7: The I-V characteristics are shown for *n*-GaP in contact with a 0.5 M H_2SO_4 electrolyte solution with an without illumination. At potentials more negative than the flat-band potential a cathodic current occurs which increases with increasing negative potential (I). The current is almost zero if the potential is positive relative to the flat band potential Due to the band bending there are no electrons available in the conduction band (CB) for a chemical reaction with the electrolyte (II). If the GaP electrode is illuminated an anodic photocurrent will flow which is indicated as I_{ph} (III). Holes in the valence band (VB) can oxidize species in the electrolyte.

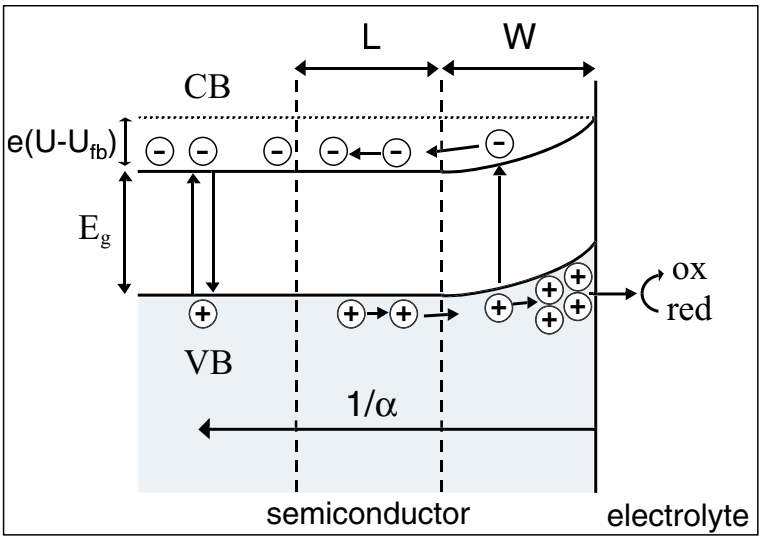

Figure 1.8: A schematic picture of *n*-GaP under illumination at a potential more positive than the flat-band potential. The band bending is given by $e(U - U_{fb})$. Electron-hole pairs can be generated with light with an energy larger than the band gap E_g. The electrons in the conduction band CB will move into the bulk of the GaP and the holes in the valence band VB to the surface, due to the band bending. Electron-hole pairs which are generated in the depletion layer (W) or the diffusion layer (L) are separated effectively. Electron-hole pairs which are created further into the bulk recombine. Holes can react at the surface with a reducing species in the solution or they can be used to etch the semiconductor (photo-etching). $1/\alpha$ is a measure for the penetration depth of the light.

tials, the surface electron concentration decreases and the cathodic current drops to zero (II). Absorption of a photon promotes an electron from the valence band to the conduction band, leaving a hole in the valence band; holes are the minority carriers in *n*-type semiconductors. Positive of the flat-band potential, the electric field due to the band bending drives photogenerated electrons into the bulk of the semiconductor and photogenerated holes toward the surface (see Figure 1.8).

In Figure 1.8, a schematic picture of *n*-GaP under illumination is shown. The potential is positive relative to the flat-band value. Due to this potential difference the energy bands are bent. The band bending is denoted as $e(U - U_{fb})$. Electron-hole pairs can be generated with light with an energy larger than the band gap E_g. The electrons in the conduction band move into the bulk of the GaP and the holes in the valence band to the surface, due to the band bending. Electron-hole

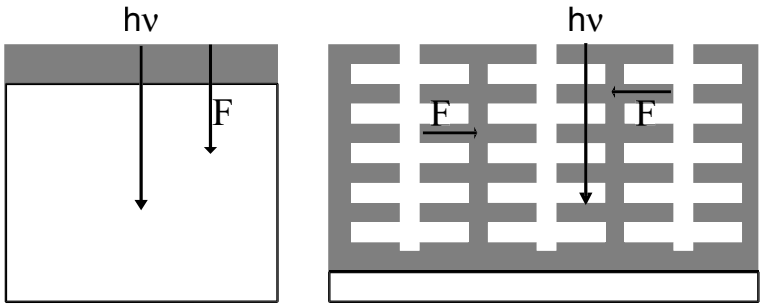

Figure 1.9: Schematic picture of porous (right) and non porous (left) GaP. If the thickness of the porous layer is larger than the penetration depth of the light, each absorbed photon create an electron-hole pair which is separated effectively. The driving force F for the electrons to reach the non-depleted area is due to the band bending and therefore perpendicular to the surface. In the case of the porous material F is orientated in all directions because of the random nature of the internal surface.

pairs generated in the depletion or the diffusion layer (i.e. in the region $W + L$) are separated effectively. The width of the diffusion layer L is determined by the diffusion length of the holes in GaP. Electron-hole pairs created further into the bulk recombine. Holes can react at the surface with a reducing species in the solution or they can be used to etch the structure (photo-etching). The reciprocal absorption coefficient $1/\alpha$ is a measure for the penetration depth of the light (for light with λ = 514.8 nm used in this work, $1/\alpha < 3$ μm).

If the potential of a GaP electrode in the dark is much higher than the flat-band potential, the bands bend more extremely and holes will be introduced in the valence band due to inter-band tunnelling. At this point the GaP starts to dissolve and can be made porous by anodic etching. In this work the GaP electrodes are made porous by electrochemical etching in 0.5 M H_2SO_4 at a potential of 10 V vs. Ag/AgCl.

The structure of the porous GaP samples used in this work have dimensions similar to the width of the depletion layer W (about 150 nm at +4 V). Therefore the complete porous layer will be depleted of electrons as is schematically shown in Figure 1.9 [6]. In this situation the concentration of free electrons is completely determined by the illumination intensity. By changing the intensity of illumination the location of the electron Fermi-level can be tuned in the band gap. Each absorbed photon will create an electron-hole pair which is separated effectively. The holes react at the surface. There is no electric field in the direction perpendicular to the interface with the bulk GaP (the electron collector). There-

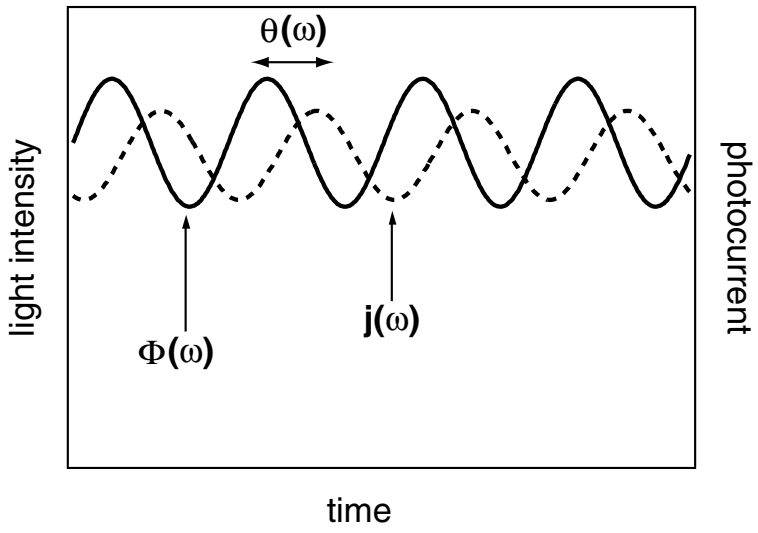

Figure 1.10: The principle of IMPS: The modulated light intensity and photocurrent are shown as a function of time. The modulation depth is about 10% of the base light intensity. The photocurrent in this figure has a phase shift relative to the light intensity.

fore, transport of the photogenerated electrons to the non-porous substrate, where they are collected, occurs by diffusion [19].

1.8 Intensity-modulated photocurrent spectroscopy

Intensity-modulated photocurrent spectroscopy (IMPS) is a time-resolved opto-electrical method. In this work the technique is used in a photoelectrochemical context to determine the origin of the transit time for transport of electrons through a macroporous GaP network. IMPS has been used before to study electron transport in macroporous semiconductor electrodes [20–22], electron-hole recombination processes, majority carrier injection at the bulk semiconductor/electrolyte interface [23], and the kinetics of electron tunnelling between semiconductor quantum dots and a metal or redox system in solution [24, 25].

In IMPS, a small-amplitude modulated light intensity $\tilde{\Phi}(\omega)$ (with modulation frequency ω) is superimposed on a steady-state light intensity Φ (see Figure 1.10), giving a modulated photocurrent $\tilde{j}(\omega)$ superimposed on the background steady-state photocurrent j. The modulated photocurrent $\tilde{j}(\omega)$ is measured at frequen-

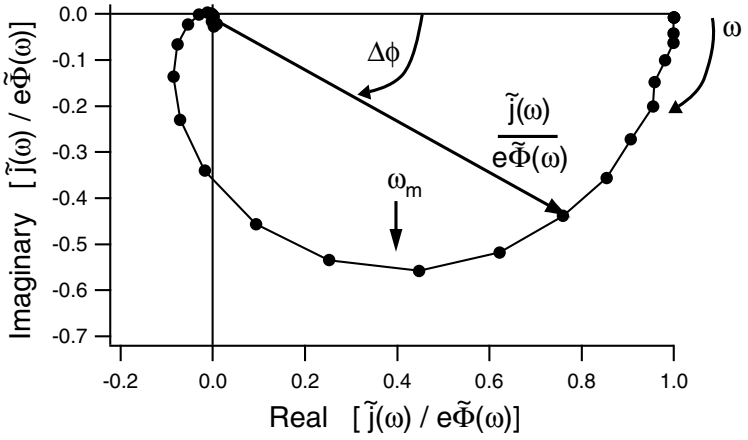

Figure 1.11: Complex plane plot of the electron transport in macroporous GaP. The optoelectrical transfer function $\tilde{j}(\omega)/e\tilde{\Phi}(\omega)$, the phase shift $\theta(\omega)$ between $\tilde{\Phi}(\omega)$ and $\tilde{j}(\omega)$, and the typical frequency of the electron transport process ω_m, are indicated in the figure.

cies lower than the RC time-constant of the electrochemical setup. The ratio $\tilde{j}(\omega)/e\tilde{\Phi}(\omega)$ is called the optoelectrical transfer function. Slow processes contributing to the total photocurrent will lead to a phase shift, $\theta(\omega)$, between $\tilde{\Phi}(\omega)$ and $\tilde{j}(\omega)$, as is shown schematically in Figure 1.10. The transfer function, determined by the amplitude ratio and the phase shift, can be plotted in the complex plane (the imaginary component versus the real component) or in a Bode plot (the imaginary or the real component versus the frequency ω). In the experimental set-up used here, consisting of an illuminated macroporous GaP electrode, the frequency at which the imaginary part of the function shows an extremum is related to the average transit time of an electron through the macroporous GaP network. The experimental determination and the theoretical derivation of $\tilde{j}(\omega)/e\tilde{\Phi}(\omega)$ are the subject of Chapter 6.

In Figure 1.11 the optoelectrical transfer function for a typical experiment on GaP is shown in the complex plane with the frequency as a parameter. In the high-frequency limit, electron transfer is slower than the light modulation and both the real and the imaginary components are zero. When the frequency is decreased, the phase shift between $\tilde{\Phi}(\omega)$ and $\tilde{j}(\omega)$ decreases, and a signal is observed. The frequency at the minimum of this distorted semicircle ω_m corresponds to the reciprocal of the average transit time of the photogenerated electrons through the macroporous GaP network. This transit time may depend on the steady-state il-

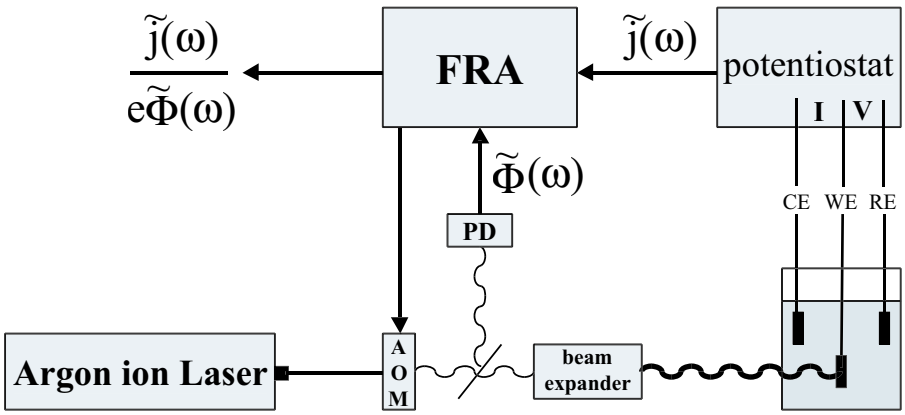

Figure 1.12: The experimental IMPS set-up. The components are described in the text.

lumination intensity. In the low-frequency limit the function is real with a value close to one which means that all photogenerated electrons are collected at the back contact (i.e. there is no loss due to recombination).

The experimental IMPS set-up is schematically represented in Figure 1.12. The green line of an argon laser (Coherent Innova), 514.5 nm or 2.41 eV, was used for electron-hole pair generation. A 10% sinusoidal modulation was superimposed on the background light intensity using an Isomet 1211 Acousto-Optic Modulator (AOM), which was controlled by a Solatron 1250 Frequency Response Analyser (FRA). About 10% of the light was directed onto a silicon photodiode (PD), which measures the background and modulated light intensity. The laser beam was expanded using a Newport beam expander to a spot of 12 cm^2 incident on the porous GaP electrode which had a geometrical surface area of 0.2 cm^2. The porous GaP electrode served as the working electrode (WE) in a standard three-electrode cell with a platinum counter electrode (CE) and a Ag/AgCl electrode as reference (RE). The electrolyte was generally a 0.2 M H_2SO_4 solution and the potential between the RE and the WE was kept at a value of 3 V. The signal due to the modulated photocurrent was passed from the potentiostat to the FRA. The FRA was used to analyze the incoming modulated photocurrent and light intensity signals and to calculate the optoelectrical admittance.

1.9 Outline of this thesis

The main emphasis of this thesis is the study of the electronic properties of ZnO quantum-dot assemblies. A ZnO assembly on a conducting substrate immersed in an electrolyte can be charged with electrons. In Chapter 2 the assembly is permeated with an aqueous electrolyte. The characteristics of long-range transport are investigated as a function of the electron occupation of the quantum dots.

In Chapter 3 the effect of the nature of the electrolyte solution permeating the quantum-dot assembly is investigated. The ZnO assembly is immersed in propylene carbonate or water in order to study the effect of the electrolyte solution on the storage and long-range transport in the quantum-dot assembly. In addition, the ultraviolet absorbance of ZnO assemblies was measured and related to the electron occupation.

ZnO assemblies absorb infrared light when the conduction levels are occupied with electrons. This infrared absorbance strongly depends on the electron occupation number and the size of the quantum dots. Chapter 4 deals with the interpretation of the infrared absorption spectra obtained from ZnO quantum-dot assemblies and colloidal solutions charged with electrons.

The luminescence properties of ZnO materials are known for more than a century. In Chapter 5 the luminescence of ZnO quantum-dot assemblies under UV-excitation is investigated as a function of the electron occupation of the quantum dots.

In the final chapter, Chapter 6, another semiconducting material is investigated, macroporous *n*-type GaP. Quantum size-confinement is not important here. The electron transport under illumination is investigated with a technique called intensity-modulated photocurrent spectroscopy.

References

[1] S.M. Sze, *Semiconductor Devices: Physics and Technology*, John Wiley & Sons, New York (1985).

[2] B. O'Regan and M. Grätzel, *Nature* **353**, 737 (1991).

[3] G. Hodes, I.D. Howell and L.M. Peter, *J. Electrochem. Soc.* **139**, 3136 (1992).

[4] A. Köhler, D.A. dos Santos, D. Beljonne, Z. Shuai, J.-L. Bredas, A.B. Holmes, A. Kraus, K. Mullen and R.H. Friend, *Nature* **392**, 903 (1998).

[5] U. Bach, D. Lupo, P. Comte, J.E. Moser, F. Weissortel, J. Salbeck, H. Spreitzer and M. Grätzel, *Nature* **395**, 583 (1998).

[6] B.H. Erné, Ph.D. Thesis, Utrecht University (1995).

[7] C. Kittel, *Introduction to Solid State Physics*, Camebridge University Press, United States of Amerika (1998).

[8] S.V. Gaponenko, *Optical Properties of Semiconductor Nanocrystals*, John Wiley & Sons, New York (1986).

[9] L.E. Brus, *J. Phys. Chem.* **80**, 4403 (1984).

[10] L.E. Brus, *J. Phys. Chem.* **90**, 2555 (1986).

[11] A. Franceschetti, A. Williamson and A. Zunger, *J. Phys. Chem. B* **104**, 3398 (2000).

[12] E.P.A.M. Bakkers, Z. Hens, A. Zunger, A. Franceschetti, L.P. Kouwenhoven, L. Gurevich and D. Vanmaekelbergh, *Nano Lett.* **1**, 551 (2001).

[13] C.B. Murray, D.J. Norris and M.G. Bawendi, *J. Am. Chem. Soc.* **115**, 8706 (1993).

[14] A. Henglein, *Topics in Current Chemistry* **143**, 115 (1988).

[15] W.A. Schoonveld, J. Wildeman, D. Fichou, P.A. Bobbert, B.J. van Wees and T.M. Klapwijk, *Nature* **404**, 977 (2000).

[16] D.S. Ginger and N.C. Greenham, *J. Appl. Phys.* **87**, 1361 (2000).

[17] R.P Andres, J.D. Bielefeld, J.I. Henderson, D.B. Janes, V.R. Kolagunta, C.P. Kubiak, W.J. Mahoney and R.G. Osifchin, *Science* **273**, 1690 (1996).

[18] C.T Black, C.B. Murray, R.L. Sandstrom and S. Sun, *Science* **290**, 1131 (2000).

[19] D. Vanmaekelbergh and P.E. de Jongh, *J. Phys. Chem. B* **103**, 747 (1999).

[20] P.E. de Jongh and D. Vanmaekelbergh, *Phys. Rev. Lett.* **77**, 3427 (1996).

[21] D. Vanmaekelbergh, F. Iranzo Marin and J. van de Lagemaat, *Ber. Bunsenges. Phys. Chem.* **100**, 616 (1996).

[22] L.M. Peter and D. Vanmaekelbergh, *Advances in Electrochemical Science and Engeneering*, John Wiley and Sons, Weinheim, Germany, 77 (1999).

[23] D. Vanmaekelbergh, A.R. de Wit and F. Cardon, *J. Appl. Phys.* **73**, 5049 (1993).

[24] E.P.A.M. Bakkers, J.J. Kelly and D. Vanmaekelberg, *J. Electroanal. Chem.* **482**, 48 (2000).

[25] E.P.A.M. Bakkers, A.L. Roest, A.W. Marsman, L.W. Jenneskens, L.I. de Jongh-van Steensel, J.J. Kelly and D. Vanmaekelberg, *J. Phys. Chem. B* **104**, 7266 (2000).

Chapter 2

A staircase in the electron mobility of a ZnO quantum-dot assembly due to shell filling

Electron transport in an assembly of ZnO quantum dots has been studied using an electrochemically gated transistor. The electron mobility shows a step-wise increase as a function of the electron occupation per quantum dot. When the occupation number is below two, transport occurs by tunnelling between the S orbitals. Transport becomes three times faster when the occupation number is between two and eight; tunnelling now occurs between the P orbitals. Electron transport is thus critically determined by the quantum properties of the building blocks.

2.1 Introduction

For many II-VI and III-V compounds synthetic routes have been developed which yield nearly monodisperse colloidal nanocrystals with a well-controlled size in the 1-10 nm range. These insulating nanocrystals show discrete atom-like valence (hole) and conduction (electron) levels due to quantum size-confinement; the energy level spectrum can be tuned, within certain limits, by variation of the size of the dots. They are, therefore, called artificial atoms or quantum dots.

Nanocrystalline quantum dots with their tunable energy levels [1, 2] are promising building blocks for novel electrical and opto-electrical devices. A field-effect transistor (FET) based on a single colloidal CdSe quantum dot 5 nm in diameter, has been studied [3]; this work forms an extension of studies of electron transport through quantum dots [4–6] and quantum dot molecules [7–9] with larger dimensions, in the 10-100 nm range as defined by lithography. In addition, electroluminescent [10, 11] and electrochromic [12] devices based on assemblies of quantum dots have been described. The performance of such devices is critically dependent on the electronic properties of the active film. Despite this, the characteristics of electron transport in an assembly of quantum dots has not received much attention.

The electronic conductivity in an assembly of nanocrystalline quantum dots will be determined by the coupling between the atom-like orbitals of neighbouring nanocrystals. If the electronic coupling is weak, electron-transport is non-coherent. In this regime, electron transport can be thermally activated due to the charging energy involved in adding an electron to a quantum dot, the so-called Coulomb-blockade effect [13–15]. For an experimental study of possible quantum effects in the electronic conduction it is of key importance to be able to vary the number of charge carriers per quantum dot in a controlled way. Furthermore, the effects of structural and electronic disorder must be small. This means that in the ideal case there should be no electronic states in the HOMO-LUMO gap and all nanocrystals should have the same size and shape. The absence of electronic disorder and the precise control of the number of charge carriers per building block have proved to be a great asset for fundamental investigations of charge carrier transport in crystals of organic molecules [15].

Electrochemical injection of electrons into an assembly consisting of ZnO nanocrystals has been studied before [16]. There were, however, indications for storage of electrons in band gap states (traps), and for electrochemical reduction of the ZnO colloids. The work of Meulenkamp formed a great step forward in this field. He developed a method for preparing homogeneous films consisting of ZnO

quantum dots with diameters in the 3-6 nm range [17]. These assemblies could reversibly store up to 10 electrons per quantum dot without any sign of chemical degradation [18]. We have built on the work of Meulenkamp to perform a study of possible quantum effects in the storage and transport of electrons in quantum-dot solids.

In this chapter, we report a study on the storage and long-range transport of electrons in assemblies of ZnO quantum dots permeated with an aqueous electrolyte (a 0.2 M PO_4^{3-} buffer with pH 8). The electron transport properties of ZnO quantum-dot films, consisting of nanocrystals, 3.9 and 4.3 nm in diameter, were studied as a function of the electron occupation. A transistor with an electrochemical gate, which will be discussed later, was used for this purpose.

2.2 Experimental

2.2.1 Preparation of the ZnO quantum-dot film

The general method to prepare ZnO quantum dots, used in this work, is based on the method originally developed by Spanhel and Anderson [19] and subsequently used by other groups [16, 20]. In this work, the method of Meulenkamp [17] is used.

A 1.1 g (5 mmol) sample of zinc acetate dihydrate ($ZnAc_2{\cdot}2H_2O$) was dissolved in 50 mL of boiling ethanol at atmospheric pressure. In contrast to the approach of Spanhel and Anderson and other workers [16, 19, 20], the solution was not refluxed for a few hours but directly cooled to 0°C. A white powder precipitated close to room temperature. X-ray diffraction showed that this was anhydrous zinc acetate ($ZnAc_2$).

A 0.29 g (7 mmol) sample of lithium hydroxide ($LiOH{\cdot}H_2O$) was dissolved in 50 mL of ethanol at room temperature in an ultrasonic bath and cooled to 0°C. ZnO quantum dots were made by adding the solution of the hydroxide in ethanol dropwise to the ethanol with precipitated $ZnAc_2$ under vigorous stirring at 0°C. The reaction mixture was stored at 0-10°C and the desired particle size was obtained by aging the ZnO sol. Other groups add water to the ZnO solution to accelerate the particle growth [16, 19, 20]. It is proven that water plays an important role in the formation of ZnO quantum dots [17]. The advantage of letting the particles grow more slowly at low temperatures and without the addition of extra water is twofold. ZnO quantum dots can be obtained with sizes in a range of 3-6 nm in diameter and the slow growth prevents the formation of defects.

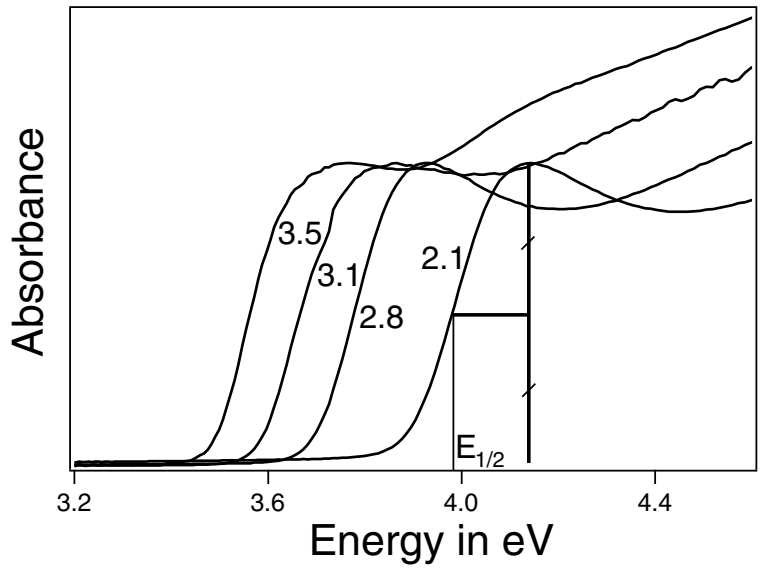

Figure 2.1: Absorption spectra of a ZnO sol at different stages of growth of the particles. Samples were taken at regular time intervals while the ZnO particles were growing in solution at 10°C. The mean diameter of the ZnO quantum dots (in nm) obtained from XRD and TEM is indicated in the figure.

Depending on the temperature of storage, the ZnO particles grow within days to weeks to a diameter of about 5 nm. In Figure 2.1 absorption spectra are shown for four different stages of the growth of ZnO nanocrystals in solution. The sizes of the quantum dots are obtained by the empirical relationship between $E_{1/2}$ and the diameter of the dots [17].

The ZnO colloids were precipitated with heptane and redissolved in water-free ethanol to remove lithium, acetate and water. With this method it is possible to remove all contaminants from the original ZnO sol. The particle size of the washed ZnO quantum dots was determined with X-ray diffraction (XRD) and transmission electron microscopy (TEM). The degree of polydispersity was obtained from TEM size histograms; 85-90$\%$ of the nanocrystals have a diameter within 20$\%$ of the mean value (see also the appendix at the end of this chapter, Section 2.5).

In Figure 2.2 the optical band gap $E_{1/2}$ of the ZnO quantum dots is shown as a function of the average diameter $\langle d \rangle$ of the dots. $E_{1/2}$ is defined as the energy at half the intensity of the first maximum in the absorbance of the ZnO sol (see Figure 2.1). From similar measurements with particles in the diameter range of 2.5-6.5 nm, Meulenkamp has established an empirical correlation:

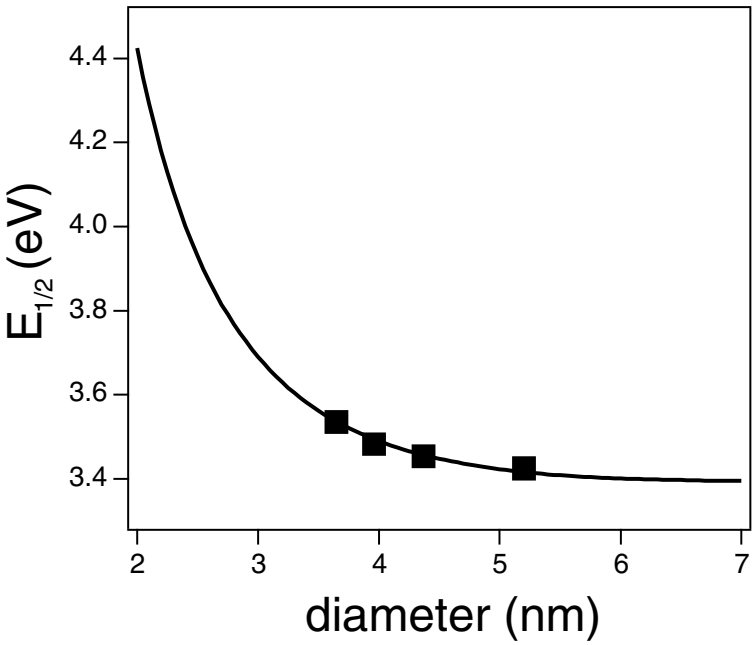

Figure 2.2: Size dependence of the optical band gap, defined as $E_{1/2}$ (see figure 2.1). The correlation between $E_{1/2}$ and $\langle d \rangle$ is taken from Meulenkamp [17] (solid line). The squares correspond to the four samples of ZnO quantum dots used for the work in this thesis.

$$E_{1/2} = 3.556 - 22.64/\langle d \rangle + 799.9/\langle d \rangle^2 \tag{2.1}$$

This equation describes very well the dependence of $E_{1/2}$ on $\langle d \rangle$. The result is plotted in Figure 2.2 as a solid line. From the squares in this figure it is clear that the four samples prepared in the present work agree well with this empirical correlation.

Films of pure wurtzite ZnO quantum dots were made by spin-coating the solution of ZnO particles on a (transparent) conducting substrate. Very flat and optically transparent films are formed with this technique (see Figure 2.3) [18]. The film was heated after each spin-coating step for 15 minutes to remove the solvent. Low temperatures of 90-110°C were used to prevent neck formation.

The fact that neck formation is not important can also be concluded from the absorption spectra: the absorption spectrum of the ZnO layer shows only a slight red-shift with respect that of the original washed ZnO sol (Figure 2.4). This con-

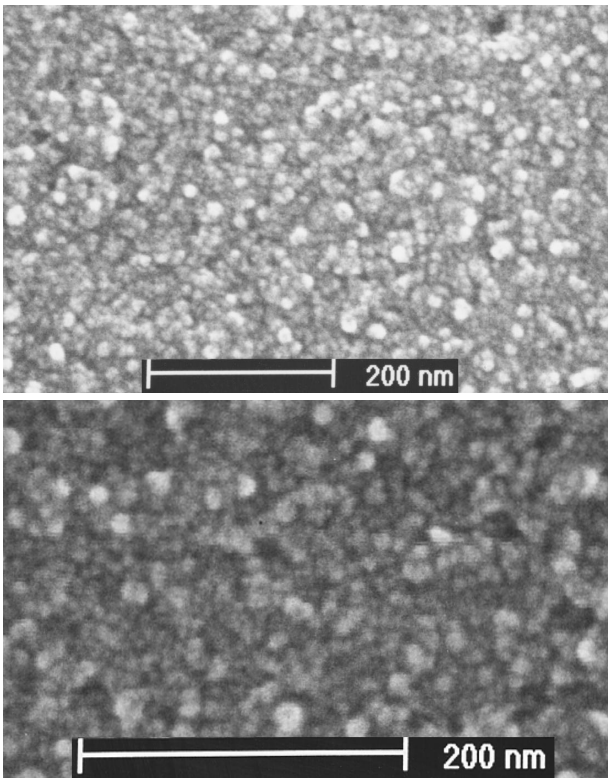

Figure 2.3: SEM images (Philips XL30 S FEG) of flat ZnO quantum-dot assemblies. The instrumental magnification used was 200,000× (upper image) and 300,000× (lower image).

firms that the quantum properties of the individual ZnO nanocrystals are preserved in the film. A slight red-shift was also seen when the layer was not heated but only dried under ambient air conditions. The film preparation and properties are different from much of the published work in which a high-temperature anneal (400°C) was often used to sinter the as-deposited film. This always resulted in an increase of the particle size and a coarser structure and sometimes substantial light scattering could not be avoided. The low temperature and the thorough washing procedure of the sol are essential in order to observe the phenomena which are described in the present work.

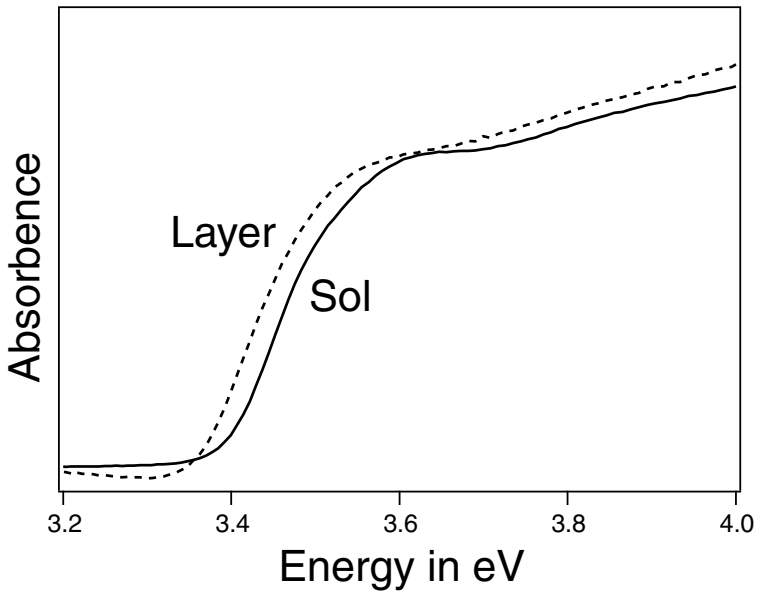

Figure 2.4: Absorption spectra of the ZnO quantum dots (diameter = 3.9 nm) in suspension (solid line) and in the active layer of the transistor (dashed line). The red-shift of the absorbance of the ZnO layer is due to a small overlap of the quantum dot orbitals. Heating for longer times and at higher temperatures can increase this effect very strongly.

2.2.2 Characterization of the ZnO quantum-dot film

The zinc and lithium content of the films was determined by inductively coupled plasma optical emission spectrometry (ICP-OES) after dissolution of the ZnO film in diluted HCl. This chemical analysis showed that lithium was not present above its detection limit (0.5 at.% relative to zinc) after the washing procedure. With the zinc content and the particle size, obtained from TEM and XRD, the number of ZnO quantum dots in the layers could be determined (see Section 2.5). The thickness of the layer was obtained by profilometry (Tencor Instruments alpha-step 500). The thickness of the various ZnO layers was approximately 200 nm in the present work.

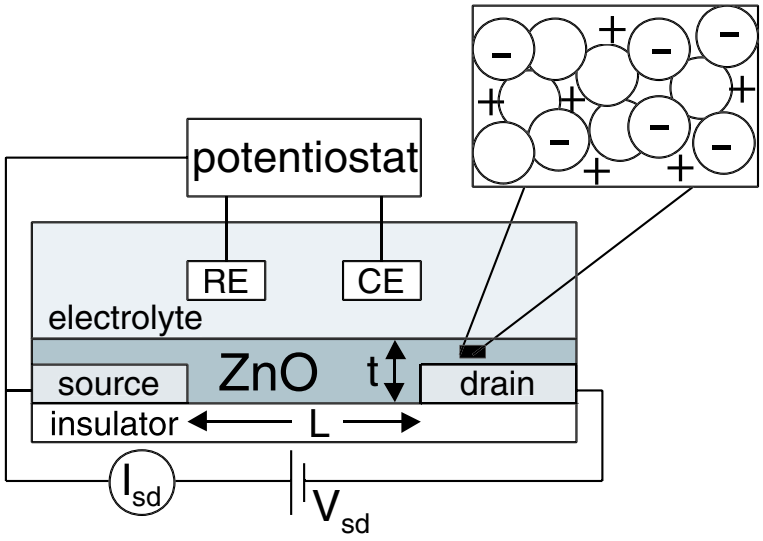

Figure 2.5: Schematic view of the electrochemically gated transistor. The source-drain distance is denoted by L (ca. 10 μm), and the thickness of the conductive channel is denoted by t (ca. 200 nm). The length of the conductive channel d (perpendicular to L and t) was ca. 1 cm. The electrochemical potential of the active ZnO layer is controlled with respect to a Ag/AgCl reference electrode (RE) using a bipotentiostat. The insert shows a detail of the active layer; the charge of the excess electrons in the quantum dots is counter-balanced by positive ions in the electrolyte. The conductance of the ZnO assembly is obtained by measurement of the source-drain current I_{sd}: $R_{sd}^{-1} = I_{sd}/V_{sd}$.

2.2.3 The transistor electrode set-up

The electrode geometry which was used in this work to measure the resistance of the ZnO quantum-dot assemblies is shown schematically in Figure 2.5. Effectively, the working electrode is divided into two separate electrodes by the introduction of a non-conducting gap (L in Figure 2.5; L is ca. 10 μm). These two electrodes are referred to as the source and drain. Source and drain consisted of gold layers of 30 nm height deposited on a flat glass substrate with a 5 nm thick layer of chromium. The ZnO film is spin-coated over the entire surface of the working electrode, covering the source, drain and non-conducting gap as can be seen in the schematic picture of the electrochemically gated transistor.

The electrochemical potentials, $\tilde{\mu}_e$, of the source and drain electrodes were controlled with respect to a Ag/AgCl reference electrode by means of a bi-poten-

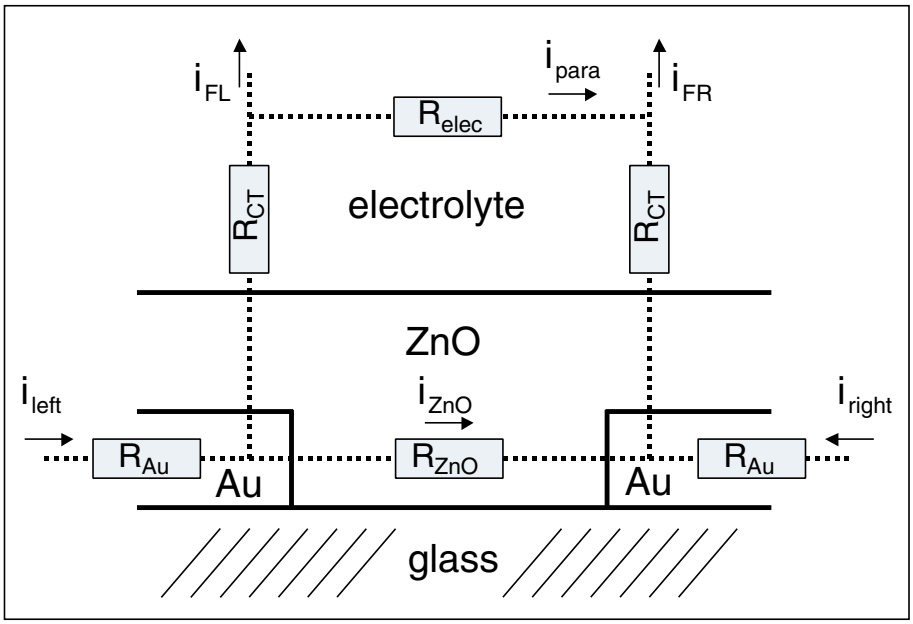

Figure 2.6: DC equivalent electric scheme of the electrode geometry used for resistance measurements. Two gold electrodes are separated by a narrow gap which is filled by ZnO. The whole system is immersed in a liquid electrolyte. The dashed lines represent possible current paths. Note that $i_{left} = i_{FL} + i_{ZnO} + i_{para}$ and that $i_{right} = i_{FR} - i_{ZnO} - i_{para}$. See the text for further details.

tiostat. A platinum foil served as the counter electrode. A small potential difference V_{sd} (1-10 mV) was maintained between source and drain to allow measurement of the conductance ($R_{sd}^{-1} = I_{sd}/V_{sd}$) of the ZnO film. The ZnO quantum-dot film equilibrates with the source (drain) electrode by adjustment of the electron density; the charge of the injected electrons is counterbalanced by incorporation of extra positive ions into the pores of the film (Figure 2.5 insert). Here the entire film is uniformly charged with electrons in contrast to the two dimensional charging occurring in a conventional field effect transistor.

2.2.4 Boundary conditions for a successful use of the transistor

The boundary conditions for the successful use of the electrochemical transistor have been discussed by Meulenkamp [18]. A brief summary is given here.

The ZnO film across the gap must be representative of the whole film. The results of the charging of the ZnO assemblies refer to the complete layer while the

measured resistance refers only to the small section of the layer within the gap. Therefore, the film (in the gap) must be uniform and its thickness must be known accurately.

The current measured between source and drain I_{sd} should be due to electrons transported through the ZnO film (i_{ZnO}) and not due to a parasitic process, e.g. motion of ions through the electrolyte (i_{para}). An equivalent electrical scheme of the set-up is given in Figure 2.6 [18]. The dashed lines represent possible current paths. Only resistances are shown because the dc conductivity was investigated. The contact resistance between the Au substrate and ZnO could be disregarded because the measured source-drain current scaled with the ZnO layer thickness.

The parasitic pathway through the electrolyte is characterized by the charge transfer resistance R_{CT} and the bulk electrolyte resistance R_{elec}. A possible parasitic pathway along the surface of the glass substrate can be disregarded because the associated resistance is expected to be much higher than R_{elec}. i_{left} and i_{right} are the measured currents through the source and drain working electrodes. i_{FL} and i_{FR} are the parasitic Faradaic currents through these electrodes. Thus:

$$i_{left} = i_{FL} + i_{ZnO} + i_{para} \tag{2.2}$$

and

$$i_{right} = i_{FR} - i_{ZnO} - i_{para} \tag{2.3}$$

R_{CT} and R_{Au} are the electrochemical charge-transfer resistance and the Au sheet resistance, respectively. There are two main requirements; the first is:

$$2 \times R_{Au} \ll R_{ZnO} \tag{2.4}$$

The current between the conductors should be determined only by the resistance of the bridge between them. Otherwise, a correction has to be introduced. In this case, R_{Au} was about 5 Ω. The (relatively high) resistance for the gold layer is due to the small layer thickness (30 nm). The second requirement is:

$$2 \times R_{CT} + R_{elec} \gg R_{ZnO} \tag{2.5}$$

This is equivalent to $i_{para} \ll i_{ZnO}$. The electrolyte resistance is small in view of its ionic conductivity and the width of the bridge. Electrochemical impedance measurements showed that R_{CT} at the highest potential used was of the order of $10^5\Omega$ for 1 cm^2 surface area [18]. A reference measurement using an electrode not covered by ZnO showed a gap resistance in accordance with this.

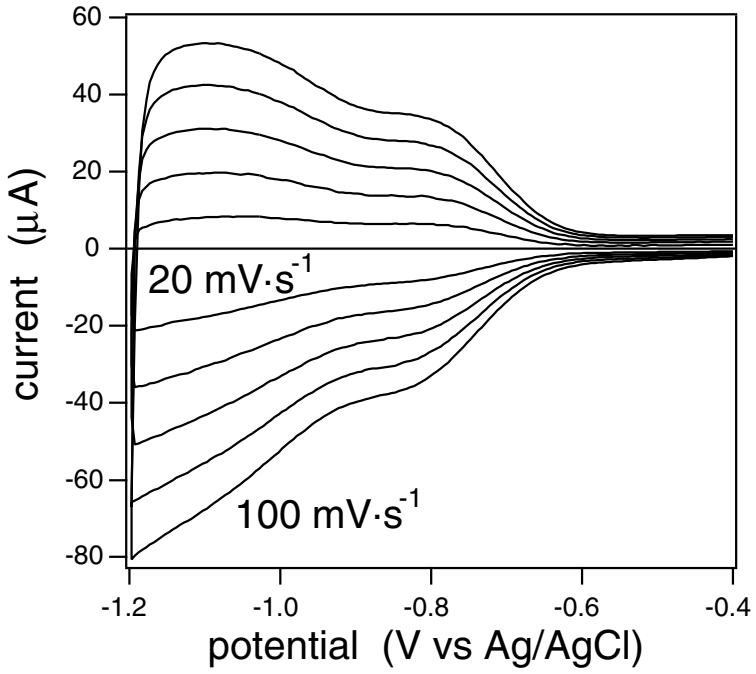

Figure 2.7: Current-potential curves of a ZnO film made from 3.9 nm nanocrystals on a gold electrode. The potential is scanned from 0 V to -1.2 V and back to 0 V again. The scan rate is varied from 20 mV·s^{-1} to 100 mV·s^{-1} in steps of 20 mV·s^{-1}. The current increases linearly with increasing scan rate.

Summarizing, we can conclude that the dimensions of the electrode enable resistance measurements between about 10 Ω and $10^5\Omega$, well-suited for the ZnO films studied in this chapter. The resistance was measured of ZnO layers with different thicknesses and a different width of the gap. The resistance was inversely proportional to the ZnO film thickness and proportional to the width of the gap. This shows that with certain boundary conditions the current which is measured between the counter electrode and the source (or drain) is the current through the ZnO film.

2.3 Results and Discussion

2.3.1 Electron storage

The characteristics of electron accumulation were studied with conventional electrodes without a gap or with the source-drain electrodes short-circuited. Figure 2.7 shows the cyclic voltammograms of a ZnO quantum-dot film in a 0.2 M phosphate buffer electrolyte (pH = 8). The current was measured while the potential was scanned from 0 V to -1.2 V and back to 0 V. Five scan rates were used, from 20 mV·s^{-1} to 100 mV·s^{-1} in steps of 20 mV·s^{-1}.

The fact that the current at a given potential increases linearly with the scan rate indicates capacitive charging of the ZnO layer. At potentials more positive than -0.65 V the curves are virtually identical. Here the underlying gold substrate is responsible for the observed current. Clearly, two distinct steps can be seen in the cyclic voltammogram of the ZnO layer at more negative potentials. A large current is observed, which changes sign as the scan direction is reversed at -1.2 V; the ZnO quantum dots are filled with electrons and emptied again in the reverse scan.

The differential capacitance C of the film (measured by the charge $\Delta Q(\tilde{\mu}_e)$ injected into the quantum-dot layer per 50 meV increase of the electrochemical potential $\tilde{\mu}_e$) reflects the quantum properties of the ZnO nanocrystalline building blocks. The results for nanocrystals 3.9 nm in diameter are shown in Figure 2.8. The onset of electron injection is at a potential $V \leq$ -0.65 V ($\tilde{\mu}_e \geq$ 0.65 eV); the capacitance function $C(\tilde{\mu}_e)$ shows two pronounced steps. Similar results were obtained with 4.3 nm ZnO quantum-dot layers for which the onset occurs at a somewhat lower electrochemical potential of about -0.60 V (Figure 2.8). Here three steps can be seen, that are, however, less pronounced than those observed with smaller ZnO nanocrystals. Integration of the differential capacitance gives the cumulative charge in the quantum dots:

$$Q(\tilde{\mu}_e) = \frac{1}{e}\int_{\tilde{\mu}_{e,onset}}^{\tilde{\mu}_e} C(\tilde{\mu}_e)d(\tilde{\mu}_e) \tag{2.6}$$

Since we know the number of nanocrystals in the film, we can calculate the average number of electrons per dot (i.e. the average occupation number $\langle n \rangle$) as a function of the electrochemical potential (see Section 2.5). Figure 2.9 shows that with dots of 3.9 nm in diameter, $\langle n \rangle$ is 1 when $\tilde{\mu}_e$ is 0.8 eV, and that close to eight electrons are present when $\tilde{\mu}_e$ is 1.2 eV. For the assembly consisting of 4.3 nm quantum dots about eleven electrons per quantum dot are present when $\tilde{\mu}_e$ is 1.2

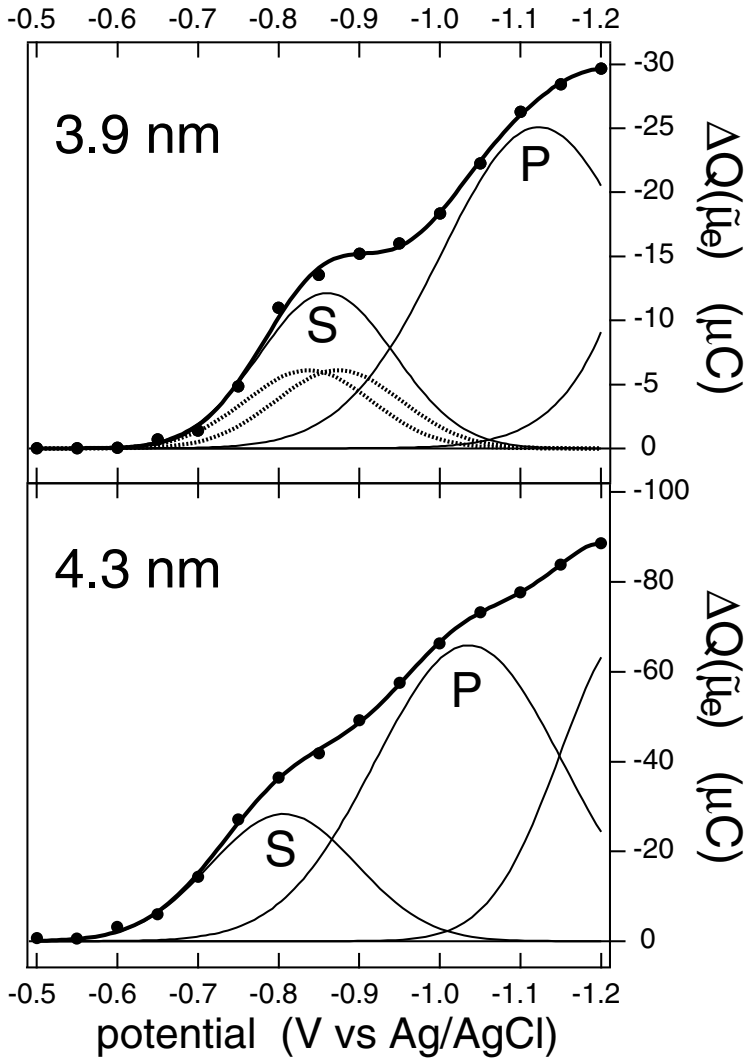

Figure 2.8: Electrochemical injection of electrons into films of ZnO quantum dots. The average diameter of the quantum dots is indicated in the figure. The dots (•) present the *differential* charge $\Delta Q(\tilde{\mu}_e)$, measured upon successive potential steps of 50 mV as a function of the electrochemical potential. The fit of the differential charge function (black lines) is explained by the filling of single-electron energy levels. The differential charge due to the filling of the *S*, *P* and *D* levels is shown in both graphs (thin black lines); filling of the two *S* levels of the 3.9 nm quantum dots is presented with dotted lines.

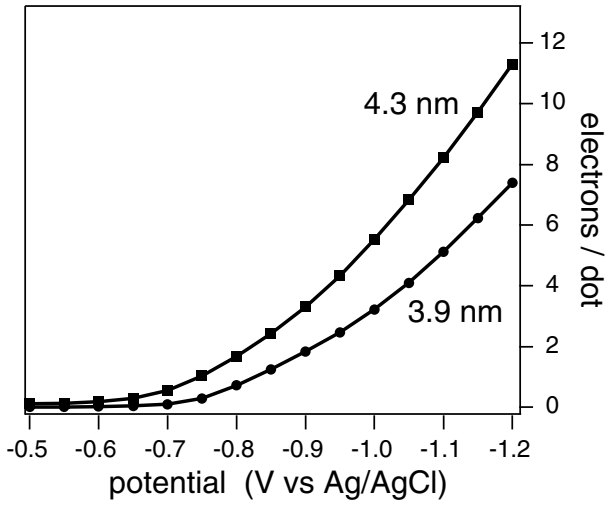

Figure 2.9: The average number of electrons per dot (i.e. occupation number $\langle n \rangle$) as a function of the electrochemical potential. The diameter of the quantum dots is indicated in the figure.

eV.

The electrons in the ZnO quantum dots may occupy the delocalized *S*, *P*, and higher conduction orbitals or be located in traps. In order to learn about the importance of traps, the light absorbance by the ZnO layer was measured under electron accumulation (Figure 2.10 and Figure 2.11). As soon as electrons are present in the film, an absorption decrease (ΔA) is found in a limited photon energy range between 3.4 and 4.0 eV. The absorbance difference increases and shifts to higher energy with increasing electron occupation.

In Figure 2.11 the integrated absorbance difference is shown as a function of the average number of electrons per quantum dot. The numbers are obtained by integrating the absorbance difference of Figure 2.10 for the 3.9 nm ZnO quantum dots and of similar plots for the 4.3 nm dots. The y-axis is in arbitrary units. The decrease of the absorbance is proportional to the occupation number at low electron concentrations:

$$-\int \Delta A(h\nu) d(h\nu) = constant \times \langle n \rangle \tag{2.7}$$

The fact that $\langle n \rangle$ goes to zero as $-\int \Delta A(h\nu) d(h\nu)$ goes to zero proves that electron storage in traps is not important. A similar conclusion can be drawn from

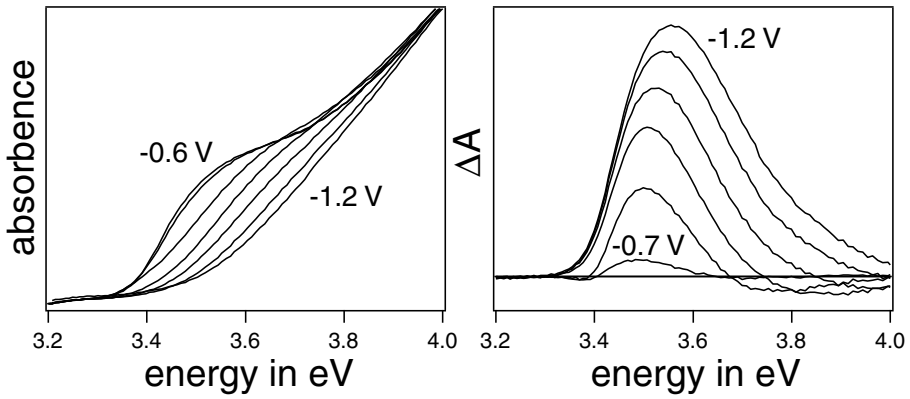

Figure 2.10: On the left side absorption spectra are shown, measured when electrons were electrochemically injected into the active layer of the transistor (made of 3.9 nm quantum dots). Six absorption spectra are depicted taken at potentials going from V = -0.6 volt (no electrons present) to V = -1.2 volt (approximately eight electrons present) in steps of 0.1 V. On the right, the corresponding absorbance difference spectra are shown. The absorbance difference is obtained by subtracting the spectra under electron accumulation from the spectrum at -0.6 volt. It is clear from these spectra that the absorbance decreases ongoing to more negative potentials i.e. with increasing electron density.

the IR absorption at $h\nu \approx 250$ meV, corresponding to the optical transition of an electron from an *S* level to a *P* level. The onset of IR absorption coincides with the onset of quenching of the UV-absorption. The results of IR measurements on layers of ZnO quantum dots will be discussed in Chapter 4.

We remark that trap-free storage of electrons in quantum-dot films has also been observed with capped CdSe quantum dots [12]. The absence of electron trapping is further supported by the prompt and strong increase of the conductance of the quantum-dot film as soon as electrons are present in the dots (Figure 2.13). This will be discussed in Section 2.3.2.

The discrete steps in the plot of the differential capacitance as a function of the potential (Figure 2.8) must reflect the atom-like energy levels of the ZnO nanocrystals. The differential capacitance function can be fitted with a sum of single-electron Gaussian functions; each Gaussian function corresponds to the occupancy of one single-electron orbital. The width of the single-electron Gaussian function reflects the size-distribution of the nanocrystals in the assembly. In Figure 2.8, the solid curves indicated by 'S' is the sum of two Gaussian single-electron functions, accounting for the occupation of the *S* orbitals. The curves

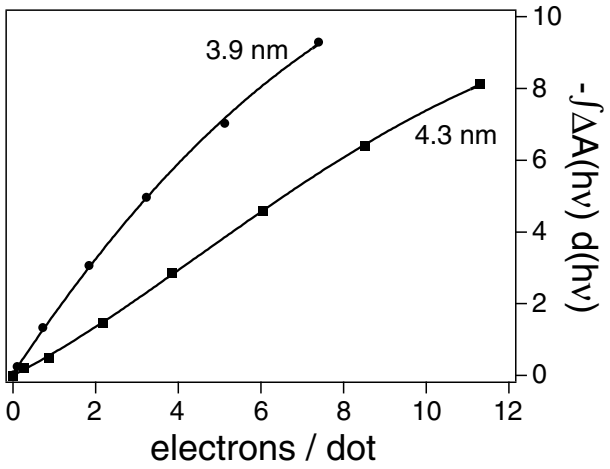

Figure 2.11: The integrated absorbance difference (obtained from results such as presented in Figure 2.10) as a function of the average number of electrons per quantum dot. The average diameter of the quantum dots is indicated in the picture.

indicated by 'P' account for the occupation of the *P* orbitals (six electrons). From the spacing between the single-electron Gaussian functions in the fit (dotted lines), it is found that the average electron-electron repulsion energy is < 30 meV. This is considerably smaller than that observed for an isolated nanocrystal (100-200 meV) [21]. This shows the effective screening of the electronic charge by the positive ions when the pores of the film are filled with an aqueous electrolyte solution. For the films consisting of 3.9 nm dots, the separation between the maxima of the *S* and *P* level distributions is 250 meV, in agreement with the results of IR absorption spectroscopy. Due to the dispersion in particle size, we find an overlap of the *S* and *P* level distributions; this has important consequences for electron transport in the film.

2.3.2 Long-range transport

In Figure 2.12 resistance measurements are shown for a ZnO layer consisting of 3.9 nm quantum dots at various electrochemical potentials. The source-drain current I_{sd} is given as a function of the source-drain potential difference V_{sd} for four potentials as indicated in the figure. The current-potential plots give straight lines which means that the resistance between source and drain R_{sd} is Ohmic. The fact that the current-potential plots go through the origin means that parasitic

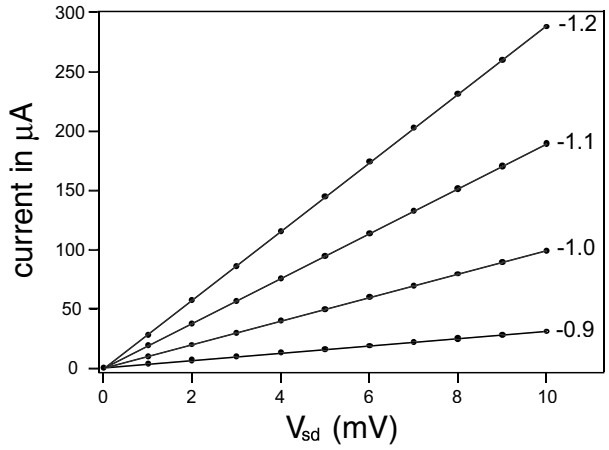

Figure 2.12: The source-drain current I_{sd} as a function of the source-drain potential difference V_{sd} for four values of the electrochemical potential (indicated in V vs. Ag/AgCl).

pathways are not important in the ZnO transistor ($i_{para} \ll i_{ZnO}$) and thus the measured resistance is due to the ZnO quantum-dot layer.

In Figure 2.13 the conductance of the ZnO film R_{sd}^{-1} and the average number of electrons per quantum dot are shown as a function of the electrochemical potential. It can be clearly seen that R_{sd}^{-1} increases over orders of magnitude as electrons are injected into the ZnO film. The resistance of the ZnO layer decreases from about $3{\times}10^5$ Ω to about 100 Ω as the potential is decreased from -0.7 V to -1.2 V; This is within the boundary conditions for a successful use of the electrochemical transistor (see Section 2.2.4).

Figure 2.14A presents R_{sd}^{-1} of the film (3.9 nm quantum dots) as a function of the occupation number $\langle n \rangle$. The conductance increases linearly with $\langle n \rangle$ for $0 \leq \langle n \rangle \leq 1.5$, and for $2.5 \leq \langle n \rangle \leq 8$; note that in the second range the slope of the $R_{sd}^{-1} - \langle n \rangle$ plot is steeper, showing that there are two regimes of transport characterized by a different electron mobility. We calculated the electron mobility from the measured conductance, using:

$$\mu = \frac{d}{eLt} \times \frac{\partial R_{sd}^{-1}}{\partial N} \tag{2.8}$$

Here d is the channel length (source-drain distance), L is the width and t the thickness of the conductive channel, and N is the electron density. We found μ = 0.017 cm^2/Vs for $0 \leq \langle n \rangle \leq 1.5$ and μ = 0.066 cm^2/Vs for $2.5 \leq \langle n \rangle \leq 8$. The variation

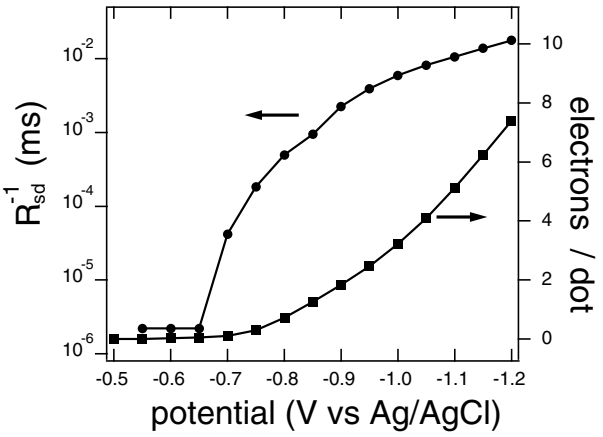

Figure 2.13: The source-drain conductance R_{sd}^{-1} as a function of the electrochemical potential (dots and line) and the average number of electrons per quantum dot (squares and line). It can be clearly seen that R_{sd}^{-1} starts to increase as soon as electrons are injected into the ZnO film.

in these values for different samples of the same quantum dots was about 10%. Similar results were obtained with films of 4.3 nm nanocrystals (Figure 2.14B); in this case μ shows three discrete steps. The fact that the observed mobilities are at least three orders of magnitude smaller than the critical mobility

$$\frac{e\Delta^2}{h} = 40\ cm^2/Vs, \tag{2.9}$$

(Δ being the diameter of the dots) shows that electronic coupling between the quantum dots is weak and transport is non-coherent [15]. This is in agreement with the observation that the optical properties of the quantum-dot film are nearly identical to those of the quantum-dot sol as can be seen in Figure 2.4. The slight red shift in the absorption spectrum of the layer relative to the suspension indicates a weak coupling of the quantum dots in the assembly. This weak coupling is essential to preserve the quantum properties of the nanocrystals. If higher temperatures and longer heating times are applied, the porosity decreases, quantum effects disappear and the bulk absorption edge is observed.

We found that the mobilities are unaffected by the temperature of the electrochemical system in the accessible range between 5 and $35°$C. This observation is in accordance with the small Coulomb charging energy of about k_BT at room temperature. Thus, electron transport occurs in the weak coupling regime, but is

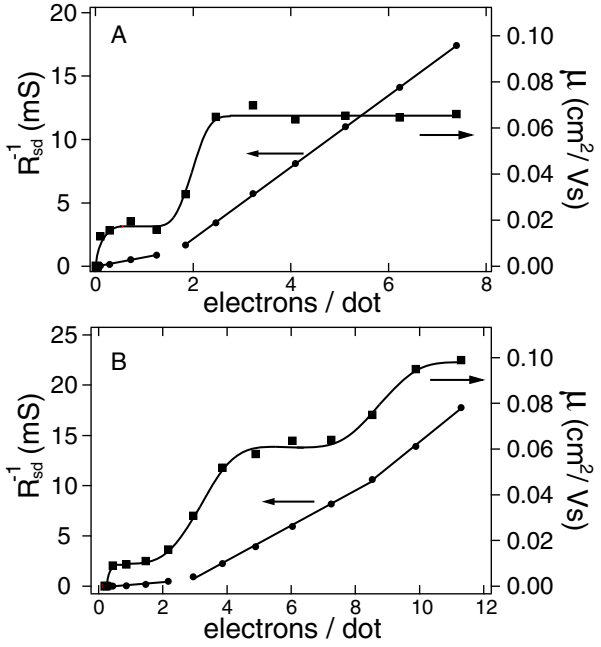

Figure 2.14: Transport properties of the ZnO films consisting of quantum dots 3.9 (A) and 4.3 nm (B) in diameter. The conductance R_{sd}^{-1} (dots and line) and the corresponding electron mobility (squares and line) are shown as a function of the average number of electrons per quantum dot $\langle n \rangle$. The uncertainty in $\langle n \rangle$ and R_{sd}^{-1} for both experiments is about 20%.

not attenuated by Coulomb-blockade effects.

In the range $0 \leq \langle n \rangle \leq 2$, the electrons occupy predominantly the *S* levels, while in the range $2 \leq \langle n \rangle \leq 8$ nearly all *S* levels are occupied and the *P* levels become progressively filled. We infer that the mobility in the range $0 \leq \langle n \rangle \leq 1.5$ corresponds to resonant tunnelling between *S* orbitals of adjacent quantum dots (μ_{S-S}= 0.017 cm^2/Vs), while the constant mobility in the range $2.5 \leq \langle n \rangle \leq 8$ reflects tunnelling between *P* orbitals (μ_{P-P}= 0.066 cm^2/Vs). Note that we do not observe a conducting-to-insulating transition at $\langle n \rangle$= 2; this is due to the overlap of the distributions of the *S* and *P* energy levels. The significance of these tunnel mobilities can be appreciated by applying the Einstein-Smoluchowski formalism. Electron transport by *S* to *S* and *P* to *P* orbital tunnelling corresponds to the following mobilities, respectively:

$$\mu_{S-S} = (e/k_B T)\frac{\Delta^2}{\tau_{S-S}} \tag{2.10}$$

$$\mu_{P-P} = (e/k_B T)\frac{\gamma\Delta^2}{\tau_{P-P}} \tag{2.11}$$

Here Δ is the length over which the electron is transferred in one tunnelling event, thus the diameter of the dot; τ^{-1} is the rate of tunnelling between two orbitals of adjacent dots, and γ accounts for the higher density of the *P* orbitals per unit energy. The fact that μ_{P-P} is slightly larger than three times μ_{S-S} is in agreement with the above equations: γ must be close to three. Moreover, because of better orbital overlap, $1/\tau_{P-P}$ is expected to be somewhat larger than $1/\tau_{S-S}$. In accordance with this idea resonant tunnelling via the *P* orbitals of a single CdSe quantum dot is found to be slightly faster than via the *S* orbitals [22]. From $\mu_{S-S} = (e/k_B T)\frac{\Delta^2}{\tau_{S-S}} = 0.017$ cm^2/Vs it follows that the tunnel rate between *S* orbitals of adjacent ZnO dots $1/\tau_{S-S}$ is $3{\times}10^9 s^{-1}$. By comparison, the rates of resonant tunnelling in a single-dot device with metal/dot tunnel barriers of 1 nm width are two orders of magnitude smaller [22].

The role of structural and electronic disorder in quantum-dot solids has been anticipated theoretically [13]. In the ZnO quantum-dot films studied here, the disorder is related to the size-distribution of the dots and their random assembly in the film (they are not close-packed). These factors of inherent disorder may lead to variations in the degree of orbital overlap between the dots and the Coulomb charging energy. Experimental studies of the effects of disorder on the optical and electronic properties of quantum-dot solids will be an important scientific issue in the coming years.

2.4 Conclusions

In this chapter the storage and transport of electrons in an assembly of ZnO quantum dots was discussed. An electrochemically gated transistor was used which allows one to charge the quantum-dot assembly uniformly, controlling the average number of electrons per quantum dot. The increasing capacitance of the film during the injection of electrons reflects the sequential filling of the *S* and *P* atom-like orbitals of the ZnO quantum dots. The electron mobility, derived from the source-drain conductance, shows a step-wise increase (staircase) as a function of the electron occupation per dot. The lowest discrete mobility is observed for an

electron occupation number per dot smaller than two, thus corresponding to *S-S* orbital tunnelling. The second discrete mobility, which is about a factor of three higher, corresponds to *P-P* orbital tunnelling and is observed for an electron occupation between two and eight. The results suggest a third regime if there are more than eight electrons per quantum dot. It is thus shown that electron transport in a nanocrystalline assembly can be determined by the orbital set of the quantum dot building blocks. Solids that offer different quantum regimes of electrical transport are very promising for novel electrical and opto-electrical devices.

2.5 Appendix

The average number of electrons per quantum dot, $\langle n \rangle$, is a very important quantity in this work. This was obtained from the *total charge* injected into the layer and the *number of quantum dots* in the layer. The injected charge was obtained from potential-step experiments; the potential was raised by 50 mV and the current due to this increase of the potential was measured and subsequently integrated, providing the charge (see Section 2.3.1). The number of ZnO quantum dots in the layer was calculated from the total volume of ZnO divided by the average volume of a quantum dot. The total volume was obtained from the mass of the ZnO divided by the density of ZnO.

To measure the amount of ZnO in the quantum-dot assemblies, the oxide was dissolved in diluted HCl (pH = 1). Because the zinc concentration of these solutions was very low (about 10 ppm), Inductively Coupled Plasma Optical Emission Spectrometry was used to determine the zinc concentration. The detection limit of ICP-OES was 0.05 ppm for zinc. With the amount of zinc obtained from ICP-OES the total volume of ZnO was calculated. The calculated number of injected electrons *per unit volume ZnO* was very reproducible with this method. A maximum deviation of 10% was found in samples which were made from the same starting ZnO suspension. The number of electrons per unit volume ZnO was in the order of $10^{20}/\mathrm{cm}^3$, which was similar to that found in other work [16, 18].

The average number of ZnO nanocrystals which were present in the assembly was obtained by dividing the total volume of ZnO by the average volume of a nanocrystal The average volume of a nanocrystal is the most critical variable in the determination of $\langle n \rangle$. *Transmission electron microscopy* (TEM) and *X-ray diffraction* (XRD) were used to determine the (average) size of the quantum dots. With TEM a two-dimensional picture is obtained (see Figure 2.15). Samples were prepared by dipping a grid with a film of amorphous carbon into the ZnO sol. A

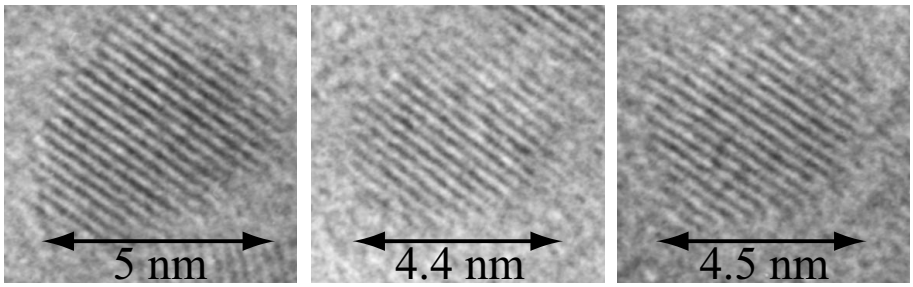

Figure 2.15: TEM pictures of three quantum dots are shown, taken from one ZnO batch. The size is indicated in the figure.

Philips CM30 HRTEM was used at an operating voltage of 200 kV.

In Figure 2.15 three ZnO quantum dots are shown. The crystal planes can be seen quite accurately in the three pictures. The size of these dots is indicated in the figure. To determine the average quantum dot size a representative collection of dots must be measured. Because the dispersion in size can be quite high, hundreds of dots must be used to get a good estimate of the average size and size-dispersion. The size of the quantum dots obtained from the TEM pictures was taken as the distance between the outer crystal planes of a single dot as is indicated in the figure. The three examples also show that our quantum dots were not perfectly spherical. Surface atoms do not contribute to the crystal planes observed in the TEM signal because of surface relaxation. The result of this surface relaxation is a displacement of the surface atoms from the 'normal' lattice positions and therefore a lack of translational symmetry. As a consequence, the real dot size can be underestimated with TEM.

A size-histogram can be made by counting the dots in a certain size-interval. Such a histogram represents the size-dispersion of the dots (see Figure 2.16). The size-histograms in Figure 2.16 were fitted with lognormal functions. It can be seen that the width at half-height in most size-dispersions is about 40%.

XRD was also used to determine the average size of quantum dots. X-ray powder diffractograms were measured with a Philips PW 1729 X-ray generator using Cu K_α radiation at a wavelength of 1.542 Å. The broadening of the lines in the X-ray diffractograms is attributed to the nanocrystalline nature of the samples and can be used to calculate the average diameter $\langle d \rangle$ of the nanocrystals by means of the Debye-Scherrer equation [23, 24]:

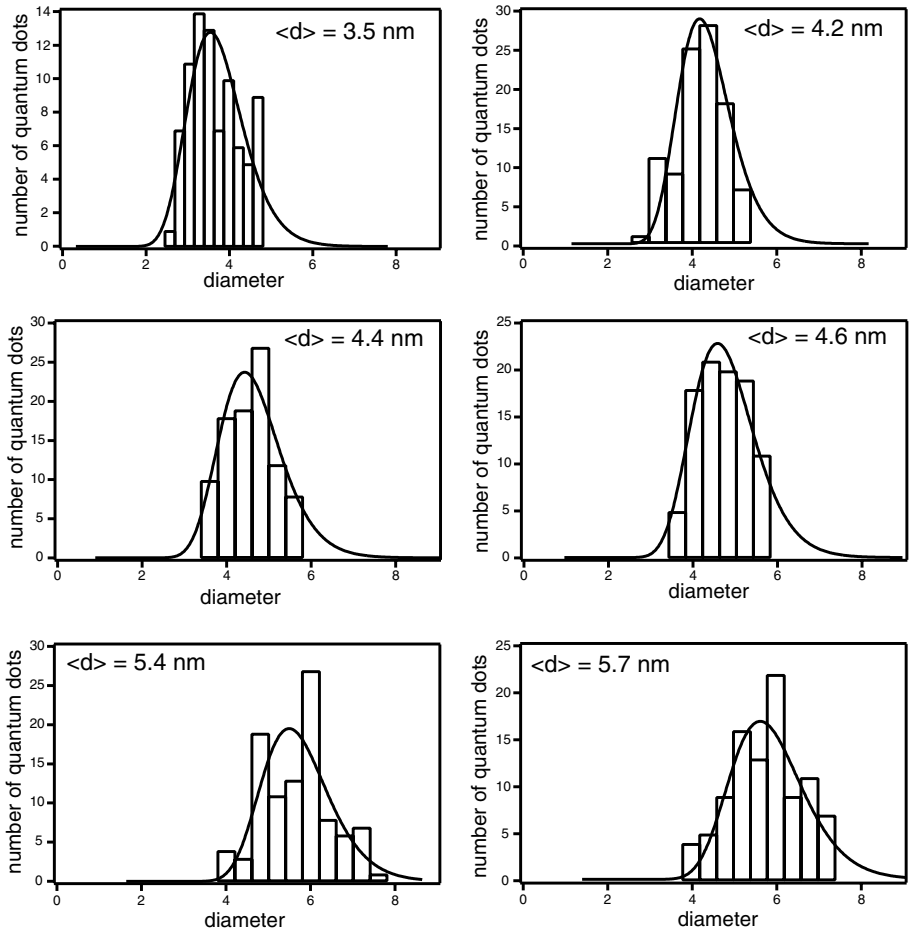

Figure 2.16: In this figure six size-histograms are shown which were obtained from several quantum dot sols. About a hundred quantum dots were used for each histogram. The data were fitted with a lognormal line shape. The average diameter found with this method $\langle d \rangle$ is indicated in the figure. The width at half-height is about 40% nm for each sample. The results were obtained by Eric Meulenkamp (Philips Research).

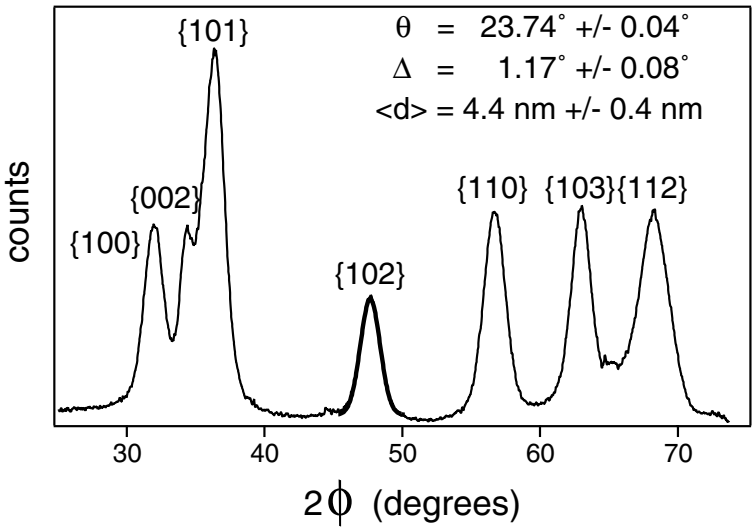

Figure 2.17: A typical XRD diffractogram of ZnO quantum dots. The peaks are broadened due to the nanocrystalline nature of the dots. The $\{102\}$ peak was used for the calculation of the average size $\langle d \rangle$; this is the most isolated peak in the diffractogram but the $\{110\}$ peak gave similar results. The values for Δ and ϕ obtained from the fit and the calculated value for $\langle d \rangle$ are indicated in the figure.

$$\langle d \rangle = \frac{0.95\,\lambda}{B\,\cos\theta} \tag{2.12}$$

Here λ denotes the wavelength of the X-ray radiation, B the full width at half maximum of the diffraction peak (in radians) and θ the maximum scatter angle. From the literature it is known that the Debye-Scherrer equation gives reasonably accurate values for the particle diameter, comparable to values obtained via high-resolution TEM measurements (i.e. to within 10%) [17, 19, 20, 25, 26].

We used the $\{102\}$ peak in the XRD diffractogram to calculate the average diameter of our nanocrystals. This is the most isolated peak in the diffractogram of ZnO as can be seen in Figure 2.17. The $\{110\}$ peak, however, gives similar results. The peaks in the diffractogram are assigned to crystal planes in wurtzite ZnO as can be found in literature [23]. The $\{102\}$ peak is simulated with a Gaussian line shape $G(\phi)$ to find the scatter angel θ and the width of the peak B:

$$G(\phi) = C \cdot exp\left[-\left(\frac{\phi-\theta}{\Delta}\right)^2\right] \tag{2.13}$$

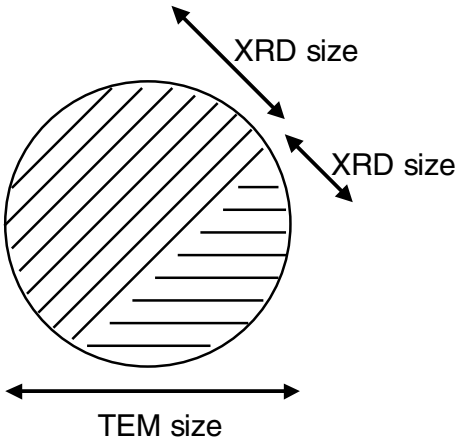

Figure 2.18: The consequences of two crystal domains for the determination of size of a quantum dot. With TEM one nanocrystal is seen in a TEM picture. With XRD two nanocrystals are observed with a smaller size than the actual one.

The results for this fitting procedure are indicated in Figure 2.17. In this fitting procedure the maximum uncertainty in the average diameter was 10%. The fitting parameter Δ is a measure for the width of the Gaussian fit and is given in degrees. C gives the height of the Gaussian fit and the width B of the peak is given by:

$$B = \frac{2\pi}{360} 2\Delta\sqrt{ln2} \tag{2.14}$$

The factor $\frac{2\pi}{360}$ is needed to convert the value for B from degrees to radians. For the example shown in Figure 2.17, the average diameter of the quantum dot can now be calculated to be 4.4 nm.

Up to now we have assumed that each quantum dot has one single crystal domain. This was quite reasonable to assume because of the small size of the nanocrystals used in this work. It is, however, possible that a quantum dot contains more than one crystal domain as is schematically drawn in Figure 2.18. If such a two-domain nanocrystal was found in a TEM experiment it was counted as one dot but XRD is only sensitive to single-crystal domains and will indicate two dots. XRD can therefore make an underestimation of the average quantum-dot size. For the same reason as in TEM, XRD will also give a slight underestimate of the average quantum dot size because of surface imperfections and therefore a loss of translational symmetry.

The pre-factor used in the Debye-Scherrer equation depends on the shape of

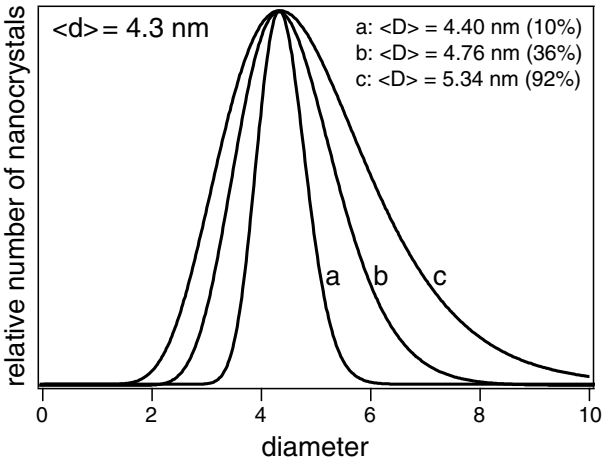

Figure 2.19: The effect of size dispersion is indicated in this figure as the volume-averaged diameter $\langle D \rangle$. Between brackets the increase in average volume of the quantum dots is indicated relative to monodisperse 4.3 nm quantum dots.

the quantum dots; the pre-factor has a value between 0.89 and 1.0 depending on the shape of the crystal (for example cubic or spherical) and the approximations that are made [17, 19]. It is clear from the TEM pictures that the two-dimensional representation of the nanocrystals is not perfectly circular and therefore the nanocrystals were not spherical. This is expected because crystals of such a small size are likely to have crystal facets at their surface. We take the pre-factor to be 0.95 with a maximum error of 5%.

With a combination of TEM and XRD we have now obtained a reasonable measure for the average diameter of our nanocrystals and the size-distribution. With this average diameter and the size-distribution we can now calculate the volume-weighted average diameter. Larger quantum dots will contribute relatively more to the total volume of ZnO than the smaller dots. The volume-weighted diameter $\langle D \rangle$ is found by calculating the average volume $\langle V \rangle$ of the quantum dots ($\langle V \rangle = \frac{\pi}{6} \langle D \rangle^3$). The average volume is found by taking a collection of quantum dots with the size-dispersion obtained from TEM, calculating the total volume of such a collection and dividing this by the total number of quantum dots. In Figure 2.19 the effect of the dispersion in the size is shown on the volume-weighted diameter at a fixed average diameter of 4.3 nm. The values in percent give the error which is made in the average volume if the average diameter is used instead of the volume-weighted diameter.

The average number of electrons per quantum dot $\langle n \rangle$ can be calculated with the following equation:

$$\langle n \rangle = \frac{n_{total}}{\frac{V_{ZnO}}{\langle V \rangle}} = \frac{\pi \langle D \rangle^3 Q \rho}{6\, e\, m_{ZnO}} \tag{2.15}$$

Here n_{total} (Q/e) is the total number of electrons and V_{ZnO} (m_{ZnO}/ρ) the total volume of the ZnO. Q is the charge in coulomb obtained from the potential step experiments, m_{ZnO} the mass of the ZnO obtained from the ICP-OES analysis and ρ the density of wurtzite ZnO (5.6 g/cm^3). Hoyer and Weller presented their average electron occupation number with an uncertainty of 50% [16]. They related this to a maximum error of 15% in the diameter of their nanocrystals obtained with TEM. From our own experience with TEM and XRD we assume the same maximum uncertainty in the average (volume-weighted) diameter we obtain. From Equation 2.15 it can be shown that the *maximum* uncertainty in $\langle n \rangle$ for a nanocrystal with a *perfectly spherical* shape and an uncertainty in the diameter of 15% is 50%.

The uncertainty in the average electron occupation number $\langle n \rangle$ must be reminded in the rest of this thesis because the average electron occupation number is a very important quantity in this work.

References

[1] H. Weller, *Adv. Mater.* **5**, 88 (1993).

[2] A.P. Alivisatios, *J. Phys. Chem.* **100**, 13226 (1996).

[3] D.L. Klein, R. Roth, A.K.L. Lim, A.P. Alivisatos and P.L. McEuen, *Nature* **389**, 669 (1997).

[4] R.C. Ashoori, H.L. Stormer, J.S. Weiner, L.N. Pfeiffer, K.W. Baldwin and K.W. West, *Phys. Rev. Lett.* **68**, 3088 (1992).

[5] S. Tarucha, D.G. Austing, T. Honda, R.J. van der Hage and L.P. Kouwenhoven, *Phys. Rev. Lett.* **77**, 3613 (1996).

[6] M. Ciorga, A.S. Sachrajda, P. Hawrylak, C. Gould, P. Zawadzke, S. Jullian, Y. Feng and Z. Wasilewski, *Phys. Rev. B* **61**, R16315 (2000).

[7] F.R. Waugh, M.J. Berry, D.J. Mar, R.M. Westervelt, K.L. Campman and A.C. Gossard, *Phys. Rev. Lett.* **75**, 705 (1995).

[8] T.H. Oosterkamp, T. Fujisawa, W.G. van der Wiel, K. Ishibashi, R.V. Hijman, S. Tarucha and L.P. Kouwenhoven, *Nature* **395**, 873 (1998).

[9] R.H. Blick, D. Pfannkuche, R.J. Haug, K.v. Klitzing and K. Eberl, *Phys. Rev. Lett.* **80**, 4032 (1998).

[10] V.L. Colvin, M.C. Schlamp and A.P. Alivisatos, *Nature* **370**, 354 (1994).

[11] B.O. Dabbousi, M.G. Bawendi, O. Onitsuka and M.F. Rubner, *Appl. Phys. Lett.* **66**, 1316 (1995).

[12] C. Wang, M. Shim and P. Guyot-Sionnest, *Science* **291**, 2390 (2001).

[13] F. Remacle and R.D. Levine, *ChemPhysChem* **2**, 20 (2001).

[14] C.W.J. Beenakker, *Phys. Rev. B* **44**, 1646 (1991).

[15] W.A. Schoonveld, J. Wildeman, D. Fichou, P.A. Bobbert, B.J. van Wees and T.M. Klapwijk, *Nature* **404**, 977 (2000).

[16] P. Hoyer and H. Weller, *J. Phys. Chem.* **99**, 14096 (1995).

[17] E.A. Meulenkamp, *J. Phys. Chem. B* **102**, 5566 (1998).

[18] E.A. Meulenkamp, *J. Phys. Chem. B* **103**, 7831 (1999).

[19] L. Spanhel and M.A. Anderson, *J. Am. Chem. Soc.* **113**, 2826 (1991).

[20] G. Redmond, A. O'Keeffe, C. Burgess, C. MacHale and D. Fitzmaurice, *J. Phys. Chem.* **97**, 11081 (1993).

[21] A. Franceschetti, A. Williamson and A. Zunger, *J. Phys. Chem. B* **104**, 3398 (2000).

[22] E.P.A.M. Bakkers, Z. Hens, A. Zunger, A. Franceschetti, L.P. Kouwenhoven, L. Gurevich, and D. Vanmaekelbergh, *Nano Lett.* **1**, 551 (2001).

[23] B.D. Cullity, *Elements of X-ray Diffraction*, Addison-Wesley, Massachusetts (1987).

[24] B.E. Warren, *X-ray Diffraction*, Addison-Wesley, Massachusetts (1969).

[25] I. Yu, *J. Phys. Chem. Solids* **57**, 373 (1996).

[26] V. Noack and A. Eychmüller, *Chem. Mater.* **14**, 1411 (2002).

Chapter 3

Long-range electron transport in assemblies of ZnO quantum dots: the effects of quantum confinement, Coulomb repulsion and structural disorder

In this chapter we compare the results for aqueous electrolytes described in the previous chapter with the results obtained with propylene carbonate solutions. The storage and long-range transport of electrons in a porous assembly of ZnO quantum dots is found to depend strongly on the interpenetrating electrolyte. The screening of the electron charge is less effective in the case of an assembly permeated with a propylene carbonate electrolyte solution. The effect of temperature on the conductance of ZnO assemblies permeated with propylene carbonate and ethanol is reported.

3.1 Introduction

When an electron is added to an otherwise neutral nanocrystal it will occupy the lowest conduction level; the corresponding orbital is strongly delocalized with respect to the atomic scale and occupies the space of the nanocrystal. Insulating nanocrystals with a diameter in the 1-10 nm range, therefore, possess discrete conduction (and valence) energy levels corresponding to orbitals with atom-like symmetry (denoted as *S*, *P*, *D*). The set of discrete energy levels depends both on the chemistry and on the size and shape of the nanocrystal. For a number of insulating nanocrystals, such as InAs, CdSe and PbS, these discrete energy levels have been studied with resonant electron tunnelling spectroscopy using an STM [1, 2]. The results are found to be in fair agreement with sophisticated electronic structure calculations based on the pseudopotential [3] or tight-binding methods [4].

Colloidal nanocrystals can be assembled to form solids. In most cases the Van der Waals interactions between the surface molecules of the nanocrystals form the driving force for self-assembly. If the size-distribution of the nanocrystals is sufficiently small, ordered arrays (also called superlattices), quantum-dot solids or artificial solids are formed by self-assembly [5, 6]. These arrays represent the analogue of crystals consisting of ordinary atoms. The optical and electrical properties of quantum-dot solids will be determined by the energy levels of the individual nanocrystal building blocks and the degree of overlap of these orbitals in the solid [7].

Figure 3.1 shows the set of energy levels (*S*, *P*, *D*, etc.) and the *S* and *P* conduction orbitals of a nearly spherical, but faceted ZnO quantum dot with a diameter of 3.9 nm, calculated by a tight-binding model. The energy separation between the conduction orbitals in such a small nanocrystal is about 300 meV. This means that quantum confinement effects should play a role in the optical and electrical properties of such systems, also at room temperature. The contour plots of the squared *S* and *P* wave functions show atom-like symmetry. They also give an idea of the degree of electronic coupling that can occur if the nanocrystals are assembled into a solid.

Experimental research on the electronic and optical properties of quantum-dot solids requires that the number of electrons (holes) per nanocrystal building block (further denoted as the electron number n) can be varied in a controlled way. We have used an electrochemical gating principle to control the electron number in porous assemblies of nanocrystals. Briefly, the nanocrystal assembly forms the bridge between a source and a drain electrode and the source-nanocrystal assembly-drain system forms a polarizable working electrode in an electrochem-

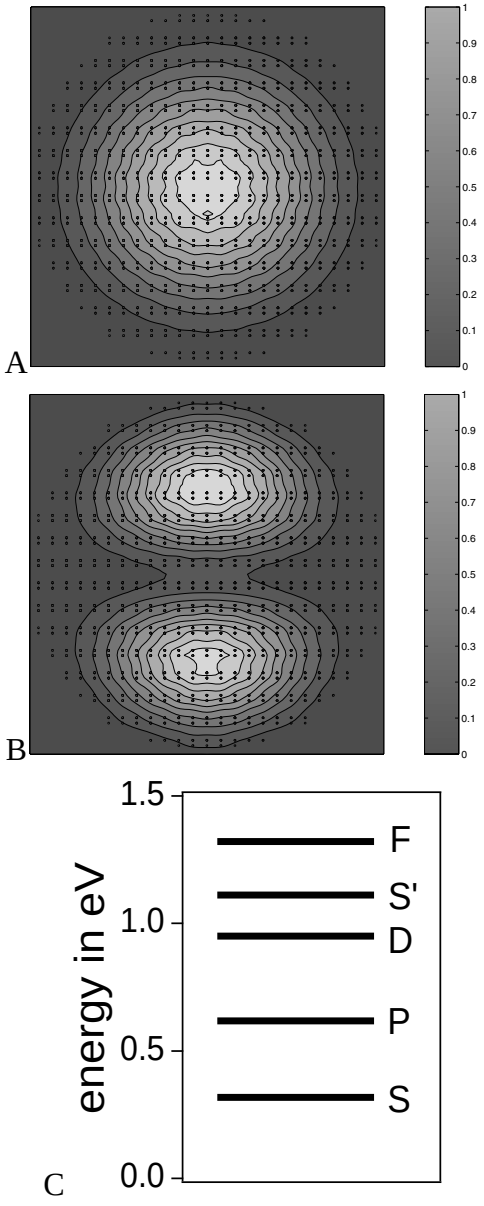

Figure 3.1: Atom-like *S* (A) and *P* (B) electron orbitals for a ZnO quantum dot (the black dots present the Zn and O atoms). (C): The energy levels calculated for a 3.9 nm quantum dot. The energy of the levels is relative to the conduction band of bulk wurtzite ZnO. The results are obtained with the *S*, *P*, *D*, *S*' tight-binding method.

ical cell. The electron number can be gradually increased from zero by changing the electrochemical potential to more negative values with respect to a reference electrode. The positive ions in the electrolyte solution in the pores of the assembly provide the counter charges for the electrons present in the nanocrystals. Electrochemical gating is an example of three-dimensional charge compensation which is of central importance for the electronic properties of single-phase solids and permeated two-phase solids [8, 9]. The electron density in the sample can be varied from zero to high values. Thus, studies with an electrochemical gate form a valuable addition to previous studies performed with a simple two-electrode set-up in which electron transport was investigated applying large electric fields [10–12]. We remark that in our case the entire film is uniformly charged with electrons in contrast to two-dimensional charging in a conventional field effect transistor or a strongly biased two-electrode system.

In Chapter 2 we described a study of the storage of electrons in an assembly of ZnO quantum dots permeated with an *aqueous electrolyte* [8]. We found that in this case the average electron number $\langle n \rangle$ could be varied in a controlled way between zero and twelve in a potential range in which ZnO is chemically stable. Clearly, the charging energy for the addition of one electron is very small due to the very effective screening of the Coulomb repulsion between the electrons present in one ZnO quantum dot. Furthermore, it was shown that long-range electron transport in such assemblies is determined by the overlap of the atom-like orbitals. A first quantum regime in which transport occurs by tunnelling between the *S* orbitals is found for $\langle n \rangle < 2$; it could be distinguished from a second regime, for $\langle n \rangle > 2$, where tunnelling between the *P* orbitals prevails.

In aqueous electrolytes the storage and transport of electrons is determined by the quantum-confined energy levels of the ZnO nanocrystals; the charging energy can be neglected. It is, at present, not clear why the charging energy is so small. Furthermore, it is not clear to what extent the chemistry at the ZnO nanocrystal/electrolyte internal interface is important. In order to address these issues, we have performed an extensive study of the storage and electron transport in a ZnO quantum-dot assembly permeated with a propylene carbonate (PC) electrolyte. Our choice for PC was determined by the fact that it cannot form hydrogen bonds with the ZnO surface molecules and solvates positive ions less strongly than water. We have used similar assemblies as in the previous study consisting of ZnO nanocrystals with diameters in the 3-5 nm range. Here, we present a detailed comparison between the characteristics of electron storage and transport in a ZnO quantum-dot assembly permeated with water and propylene carbonate. For the sake of comparison we include in this chapter results and some discussion from

the previous chapter.

3.2 Experimental

The synthesis of the colloidal ZnO nanocrystals [13] has been described in detail in Section 2.2.1. The particle size of the washed ZnO quantum dots was determined with X-ray diffraction (XRD) and transmission electron microscopy (TEM). The diameter of the quantum dots used in the present work is 3.9$\pm$ 0.9 and 4.3$\pm$ 1.0 nm. The maximum error which is made in the determination of the diameter of the quantum dots with TEM and XRD is estimated to be 15% in accordance with the value stated by Hoyer and Weller [14].

Transparent films of pure wurtzite ZnO quantum dots were made by spin-coating the solution of ZnO particles on a (transparent) conducting substrate. Very flat and optically transparent films are formed with this technique [15]. The thickness of the layer was obtained by profilometry (Tencor Instruments alpha-step 500). The thickness of the various ZnO layers is about 200 nm in the present work. For the measurements of the long-range transport gold substrates were used (30 nm thick gold deposited on a 5 nm thick adhesion layer of chromium on a flat glass substrate). Between the electrodes there was a non-conducting gap, 10 μm wide and 1 cm long.

The film was heated after each spin-coating step for 15 minutes to remove the solvent. Low temperatures (90-110°C) were used to prevent neck formation between the dots. The low temperature and the thorough washing procedure of the sol are necessary to observe the phenomena which are described in the present work. The absorption spectrum of the ZnO layer shows a slight red-shift with respect to the absorption spectrum of the original washed ZnO sol (see Section 2.2.1). This confirms that the quantum properties of the individual ZnO nanocrystals are preserved in the film. A slight red-shift was also seen if the layer was not heated but only dried in ambient air conditions. The film preparation and properties are different from much of the work that has been published, where often a high-temperature anneal (400°C) was used to convert the as-deposited film to a porous ZnO film. This always resulted in an increase of the particle size and a coarser structure and, sometimes, substantial light scattering could not be avoided.

The zinc and lithium content of the films was determined by inductively coupled plasma optical emission spectrometry (ICP-OES) after dissolution of the films in diluted HCl. This chemical analysis showed that lithium was not present above its detection limit (0.5 at.% relative to zinc) after the washing procedure.

From the amount of ZnO and the average volume per quantum dot the number of quantum dots in the film is estimated. From this number and the injected charge, the average number of electrons per dot $\langle n \rangle$ is obtained (see also Section 2.5).

The aqueous electrolyte was an argon-purged 0.2 M phosphate buffer (pH = 8) and was made by adding pure NaOH to phosphoric acid. Here the reference electrode was a Ag/AgCl electrode, and the counter electrode a platinum sheet. Otherwise, anhydrous propylene carbonate (PC) with 0.1 M tetrabutylammonium perchlorate ($TBAClO_4$) was used. In this electrolyte a silver rod served as a quasi reference electrode. The quasi reference electrode potential was calibrated with the ferrocene/ferrocinium couple and was found to be 200 mV vs. Ag/AgCl. The experiments in PC were carried out in a nitrogen-filled glovebox to keep the electrolyte free of oxygen and water. The ethanol and propylene carbonate were used without further purification. The water content of the pure solvents was 0.2% and 0.3% respectively.

The low-temperature electrochemical measurements were performed using a liquid-helium flow-cryostat equipped with a sample heater to stabilize the temperature between 150 K and room temperature.

3.3 Results and Discussion

3.3.1 Electron Storage

We have investigated the storage and long-range transport of electrons in ZnO quantum-dot assemblies permeated with aqueous and non-aqueous electrolyte solutions. The differential charge $\Delta Q(\mu_e)$ injected into the quantum-dot layer was measured per 50 meV increase of the electrochemical potential μ_e of the source-drain electrode system (the source and drain electrodes are kept at the same potential). The differential charge is shown for the injection of electrons into ZnO quantum-dot layers permeated with the phosphate buffer (Figure 3.2A) and the propylene carbonate electrolyte (Figure 3.2B). Nanocrystals with a mean diameter of 3.9 and 4.3 nm were used.

If a sufficiently negative potential is applied, electrons can be stored in the ZnO nanocrystals. The onset potential of electron injection depends on the average size of the quantum-dot building blocks in the ZnO layer. Electron injection occurs at potentials of about -0.65 and -0.60 V in water, and -0.30 and -0.20 V in PC for the 3.9 and 4.3 nm diameter particles, respectively. A variation of the pH of the phosphate buffer in the range 7-10 did not change the charging characteristics apart from a shift of the onset potential, which corresponded nicely to

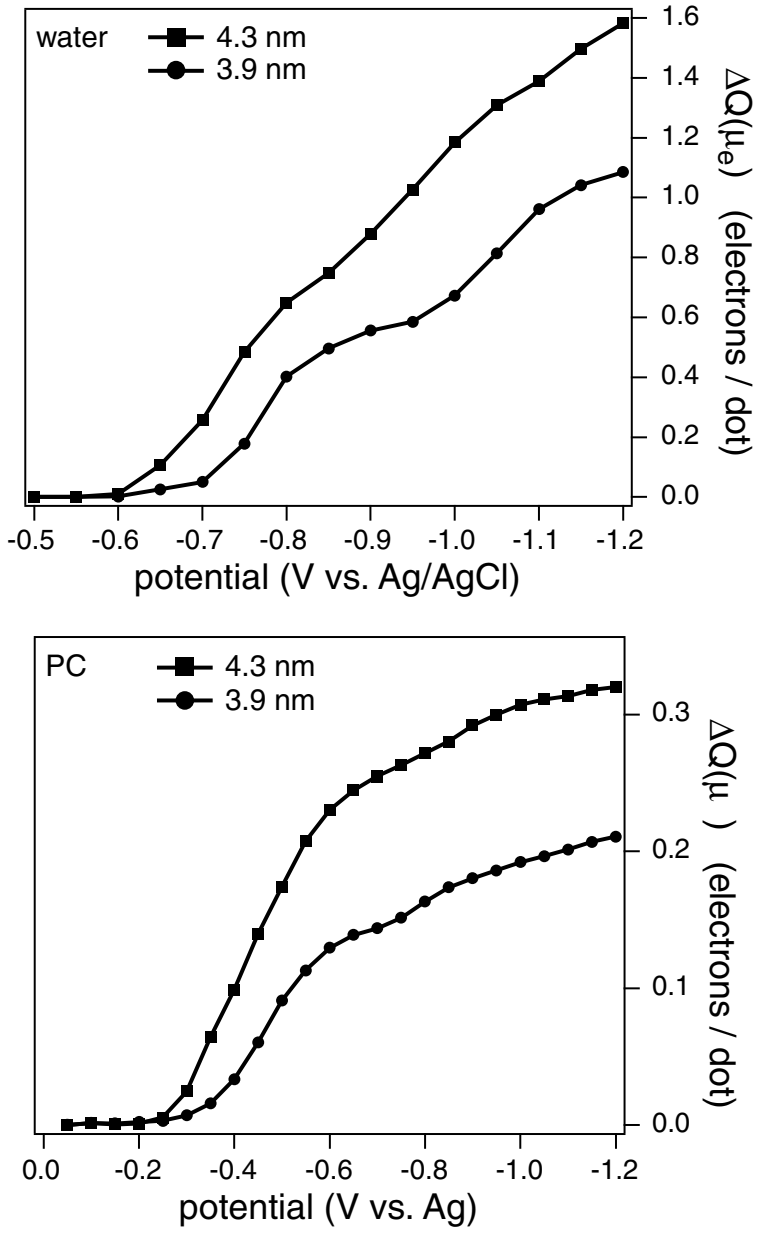

Figure 3.2: The differential charge $\Delta Q(\mu_e)$, expressed as electrons per dot, measured upon successive potential steps of 50 mV, in a ZnO quantum-dot assembly permeated with an aqueous phosphate buffer or 0.1 M $TBAClO_4$ in PC as a function of the electrochemical potential. The average diameter of the quantum dots is indicated in the figure.

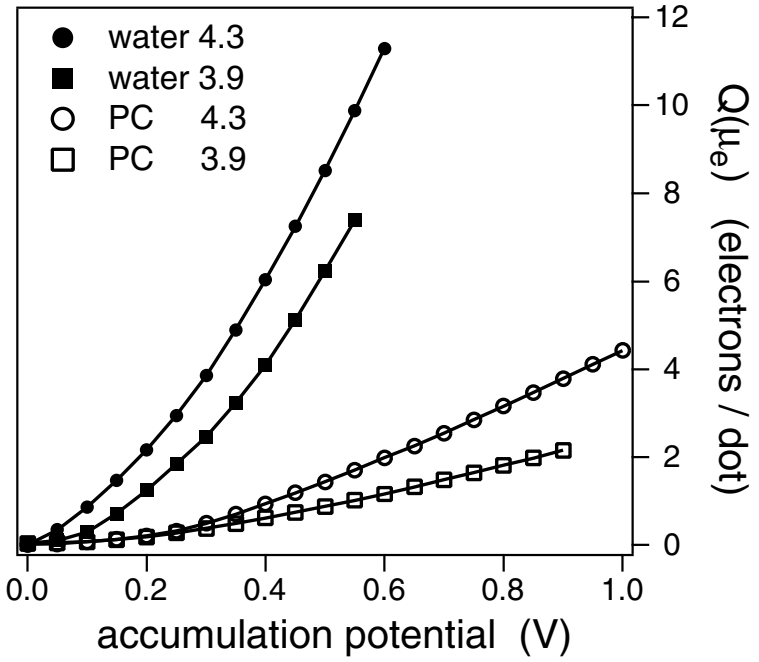

Figure 3.3: The average number of electrons per quantum dot in a ZnO quantum-dot assembly permeated with a phosphate buffer and 0.1 M $TBAClO_4$ in PC as a function of the accumulation potential. The average diameter of the quantum dots is indicated in the figure.

Nerstian behaviour. Similar results were found by Noack et al. [16]. The differential capacitance function of the quantum-dot layers permeated with water, shows two waves for an assembly of 3.9 nm quantum dots; the function suggests three waves in the case of an assembly with 4.3 nm quantum dots. The significance of these steps was already discussed in Chapter 2. In PC some small steps can also be seen for both sizes of quantum dot. Integration of the differential charge from Figure 3.2 gives the cumulative charge, Q(μ_e), in the quantum dots:

$$Q(\mu_e) = \frac{1}{\Delta V} \int_{\mu_{e,onset}}^{\mu_e} \Delta Q(\mu_e) d\mu_e \tag{3.1}$$

Here ΔV is the size of the potential step. From the cumulative charge and the known number of quantum dots in the film (see Section 3.2), the average number of electrons per ZnO quantum dot $\langle n \rangle$ can be obtained as a function of the electrochemical potential (see Figure 3.3). It is evident that the larger nanocrystals

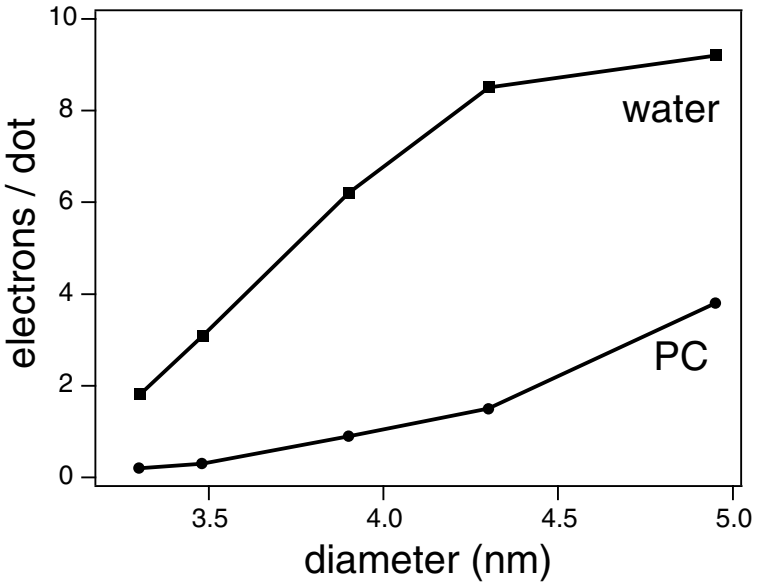

Figure 3.4: The average number of electrons per quantum dot at an accumulation potential of -500 mV. The results are shown for ZnO films, prepared from nanocrystals of several sizes, permeated with water and PC.

contain more electrons than the smaller ones at the same accumulation potential (i.e. the potential versus the onset potential of electron injection). For example, in the assemblies permeated with water, at an accumulation potential of 0.5 V, the larger nanocrystals contain about 8 electrons per quantum dot whereas the smaller ones have about 6 electrons per dot. This efficient electrochemical 'gating' is typical for the case in which the transistor layer is permeated with an aqueous electrolyte [14, 15, 17]. At the same accumulation potential in PC about 1.5 and 1.0 electrons can be stored in the ZnO quantum dots for the 4.3 and 3.9 nm quantum dots, respectively. This is much less than in water. The electrochemical gating is, therefore, much less effective in PC. Furthermore, we found that the charging characteristics in aqueous and non-aqueous electrolyte solutions are independent of the cation that was used as a counter charge; i.e. the differential charge function did not change on replacing Na^+ with the tetrabutyl- or tetramethylammonium cation.

Figure 3.4 summarizes the capability of electron storage in ZnO assemblies permeated with water or PC. We plot the average number of electrons per dot for an accumulation potential of -0.5 V. It is clear that considerably more electrons

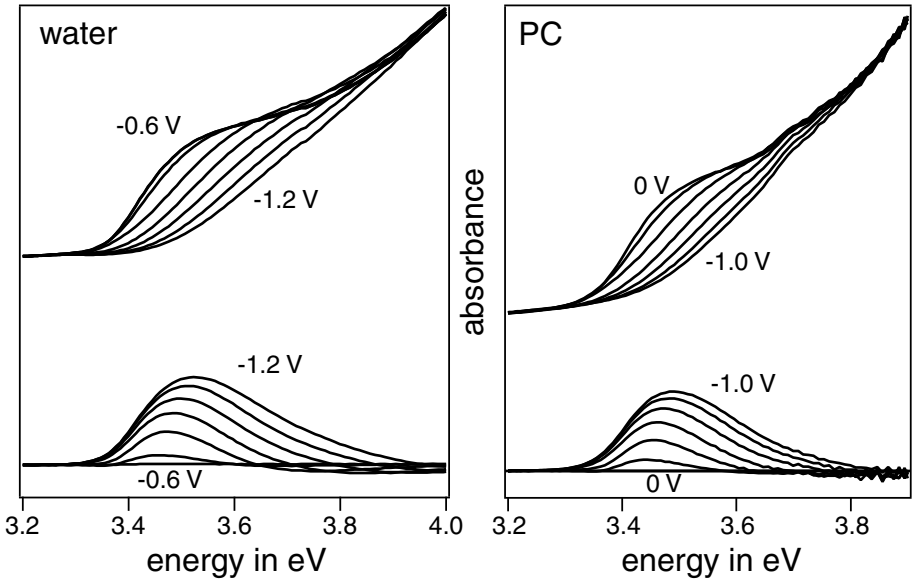

Figure 3.5: Absorption spectra are shown, measured as electrons are electrochemically injected into the active layer of the transistor (made of 4.3 nm dots). The measurements were performed in the phosphate buffer (left) and PC (right). Seven absorption spectra are depicted taken at potentials going from V = -0.6 volt (no electrons present) to V = -1.2 volt for the phosphate buffer and -0.5 to V = -1.0 volt for PC, in steps of 0.1 V. The lower figures show the corresponding absorbance difference spectra. The absorbance difference was obtained by subtracting the spectra under electron accumulation from the spectrum at -0.6 and 0.0 volt for the phosphate buffer and PC respectively. It is clear from these spectra that the absorbance decreases on going to more negative potentials i.e. as more electrons are present in the layer.

per quantum dot can be stored using water as compared to PC at the same accumulation potential. This difference becomes relatively larger as the size of the quantum dots becomes smaller. We conjecture that the high electrochemical gating efficiency in water is due to the presence of protons (10^{13} cm^{-3} at pH = 8). The concentration of protons in the aprotic electrolytes used in this work is many orders of magnitude lower. Protons can adsorb on the ZnO surface or even be inserted into the ZnO nanocrystals [18]; the cations are, therefore, very close to the electrons in the ZnO dots which results in an efficient screening of the electron charge.

The electrons in the ZnO nanocrystals can be located in delocalized *S*, *P*, and higher energy conduction orbitals, or in trap states. In order to investigate the

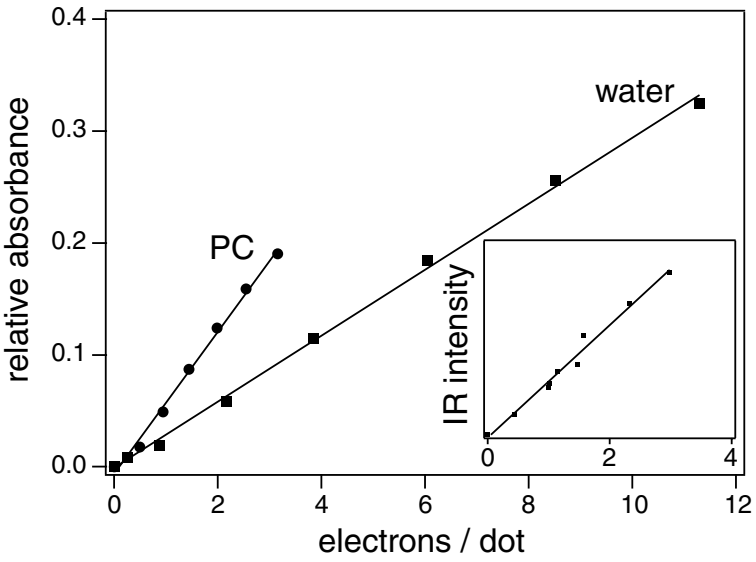

Figure 3.6: The relative absorbance as a function of the average number of electrons for the water and PC systems. The relative absorbance is defined as the quenching of the absorbance between 3.3 and 4.0 eV divided by the total absorbance between 3.3 and 4.0 eV without quenching. The IR absorbance is shown in the inset as a function of $\langle n \rangle$ (the measurement was performed in PC).

possibility of trapping, we measured the quenching of the optical absorbance of the HOMO-LUMO and higher energy transitions of the ZnO quantum-dot layers on varying the electron occupation. The absorbance in the energy range between 3.3 and 4 eV is quenched significantly when electrons are present in the films (Figure 3.5).

The quenching signal $-\Delta A(h\nu)$ becomes broader in energy at higher energies and increases in intensity when the electron density increases. At low electron occupation ($\langle n \rangle < 2$) the HOMO-LUMO is quenched, while at higher electron occupation optical transitions between other energy levels are also quenched. In Figure 3.6, the integrated absorbance difference, $-\int \Delta A(h\nu) d(h\nu)$, is plotted as a function of the average number of electrons per quantum dot $\langle n \rangle$, in the ZnO layers prepared from 4.3 nm quantum dots. Similar results are obtained when films are used with quantum dots of a different size. The results are shown for a layer permeated with water (■) and with PC (●). The relative absorbance is defined as the decrease of the absorbance between 3.3 and 4.0 eV divided by the total absorbance between 3.3 and 4.0 eV at 0.0 V (i.e. at zero quenching). The

total absorbance between 3.3 and 4.0 V was the same for assemblies permeated with PC or the phosphate buffer.

The integrated absorbance difference increases almost linearly with the injected charge and the process is completely reversible in the potential range between 0 and - 1.2 V in water and between 0 and -1 V in PC. A striking result is that in water approximately twice the number of electrons per dot are needed to obtain the same quenching of the absorbance. We do not have an explanation for this effect. Furthermore, the quenching of the UV-absorbance vanishes only when $\langle n \rangle$ goes to zero and the IR absorbance increases as soon as electrons are injected into the ZnO assembly permeated with PC as shown in the insert of Figure 3.6. The details of the IR measurements are discussed in Chapter 4. This shows that all electrons are located in *S*, *P* and higher energy atom-like conduction orbitals and that electron localization in surface states is not important. The idea that electron trapping in localized band gap states is not important is further supported by the prompt and strong increase of the conductance of the quantum-dot layer observed as soon as electrons are present in the dots (see Section 2.3.2). In agreement with this, electrochemical results obtained with ZnO single crystals have shown no or only minor effects of interfacial band gap states [18]. Still, our results with quantum-dot assemblies are surprising, since the number of ZnO surface sites in a quantum dot is very large.

The differential charge (i.e. capacitance) functions presented in Figure 3.2 reflect the consecutive filling of the two-fold degenerate *S* and six-fold degenerate *P* orbitals by electrons. These results can be understood on the basis of the thermodynamic framework for electron addition to quantum dots proposed by Zunger and co-workers [3]. In this framework, the electrochemical potential for electron addition to a quantum dot is considered, taking into account the quantum-confined single-particle energy levels, the dielectric polarization due to the electron charge and Coulomb repulsion between the electrons occupying delocalized conduction orbitals. Addition of the first three electrons to an otherwise neutral quantum dot can be described by:

$$S^0 + e \rightarrow S^1 \qquad \mu_e(S^{0/1}) = \epsilon_S + E_{pol} \tag{3.2}$$

$$S^1 + e \rightarrow S^2 \qquad \mu_e(S^{1/2}) = \epsilon_S + E_{ee} + E_{pol} \tag{3.3}$$

$$S^2P^0 + e \rightarrow S^2P^1 \qquad \mu_e(P^{0/1}) = \epsilon_P + 2E_{ee} + E_{pol} \tag{3.4}$$

Equations 3.2 to 3.4 give the electrochemical potentials for injection of the first, second and third electron in a ZnO quantum dot. These electrochemical potentials

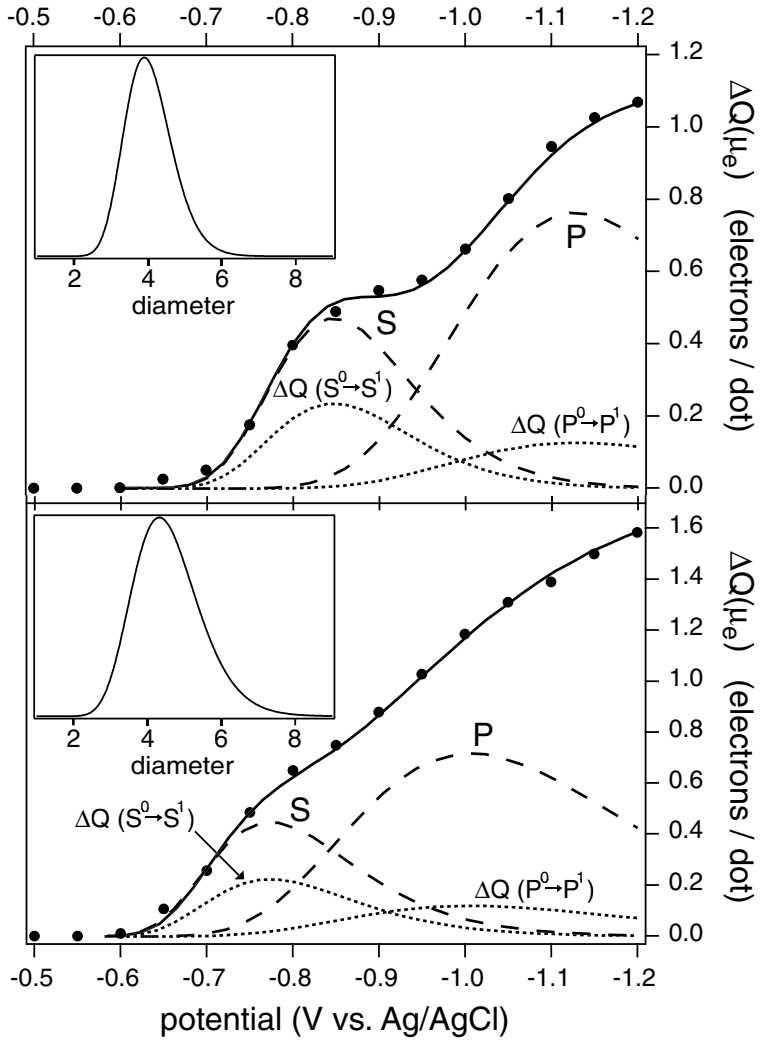

Figure 3.7: Fit of the potential dependence of the differential charge (experimental data are indicated by •'s), normalized as the number of added electrons per 50 mV per quantum dot, as a function of the electrochemical potential. The ZnO assembly is permeated with an aqueous solution. The experimental results are obtained with an assembly of 3.9 (upper figure) and 4.3 nm (lower figure) nanocrystals. The solid lines give the best fit obtained with the sum of single-electron addition functions. The addition functions $\Delta Q(S^0 \rightarrow S^1)$ and $\Delta Q(S^2P^0 \rightarrow S^2P^1)$ (dotted lines) are calculated with a model that takes into account the quantum-confined single-particle energy levels, $\varepsilon_S(d)$, $\varepsilon_P(d)$, ... and a very small Coulomb repulsion ($E_{ee}(d) < kT$). The overall *S* and *P* energy levels are also shown (dashed lines). The *D* energy levels are omitted for clarity. The size-distribution used for the best fit is shown in the insert.

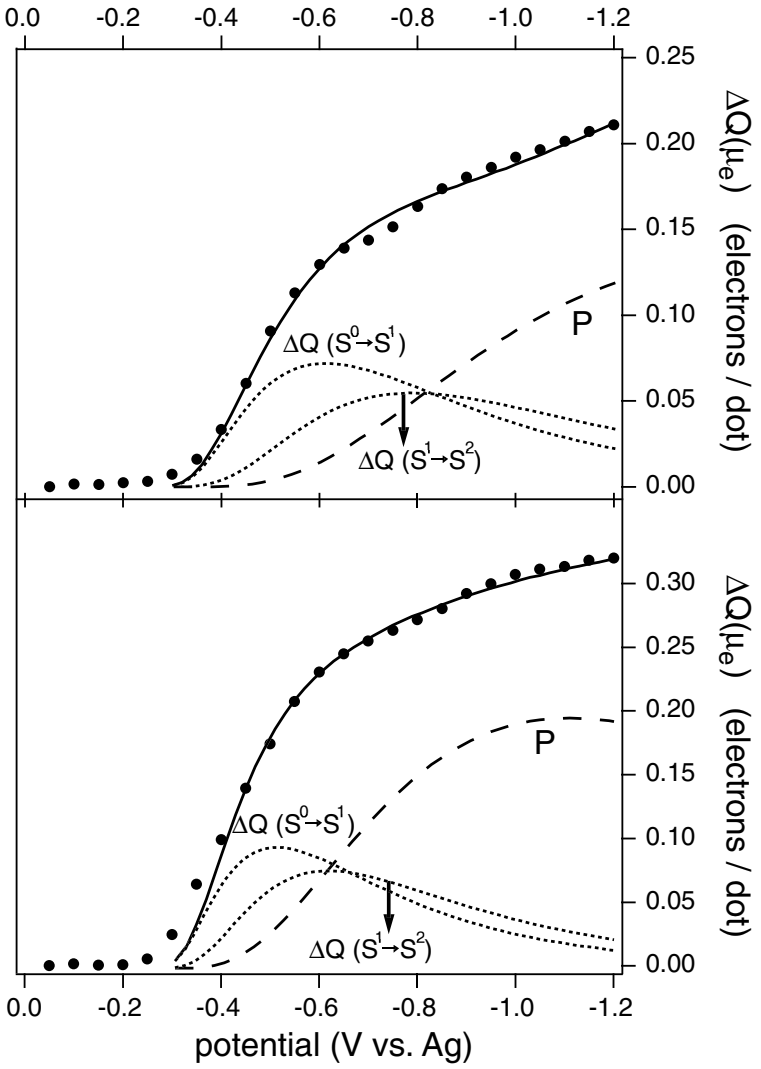

Figure 3.8: Fit of the potential dependence of the differential charge (experimental data are indicated by •'s), normalized as the number of added electrons per 50 mV per quantum dot, as a function of the electrochemical potential. The ZnO assembly is permeated with a propylene carbonate solution. The experimental results are obtained with an assembly of 3.9 (upper figure) and 4.3 nm (lower figure) nanocrystals. The solid lines give a fit with a sum of single-electron addition functions. The single addition functions $\Delta Q(S^0 \rightarrow S^1)$, $\Delta Q(S^1 \rightarrow S^2)$ (dotted lines), ... are calculated with a model accounting for quantum-confined single-particle energy levels, $\varepsilon_S(d)$, $\varepsilon_P(d)$, ... and a size-dependent Coulomb repulsion energy (200 and 130 meV for 3.9 and 4.3 nm dots, respectively).

depend on the energy of the orbitals (ϵ_S and ϵ_P), the self-polarization energy per added electron (E_{pol}) and the electron-electron repulsion energy (E_{ee}) [3]. The differential charge functions can now be fitted with a sum of single-electron addition functions calculated with Equations 3.2 to 3.4 and a size-distribution for the ZnO nanocrystals in the assembly (Figure 3.7 and 3.8). The size-distributions used here are presented as inserts in Figure 3.7. The diameter dependent single-particle energy levels $\varepsilon_S(d)$ and $\varepsilon_P(d)$ are obtained from tight-binding theory (see also Section 4.2). The self-energy (i.e. polarization energy) $E_{pol}(d)$ and the repulsion energy $E_{ee}(d)$ are assumed to be proportional to d^{-1} [19].

Figure 3.7 shows the single-electron addition functions $\Delta Q(S^0 \rightarrow S^1)$ and $\Delta Q(S^2P^0 \rightarrow S^2P^1)$, and the total fit for the results obtained with an assembly permeated with an aqueous solution. We find that the experimental results can be fitted very well with a small value for the repulsion energy E_{ee}, i.e. $E_{ee} < kT$. As a consequence of the negligible repulsion energy, the addition curves $\Delta Q(S^0 \rightarrow S^1)$ and $\Delta Q(S^1 \rightarrow S^2)$ overlap. In addition, the width of the functions is entirely determined by the size dispersion. The difference in electrochemical potentials corresponding to the maxima of the single-electron addition functions reflect the energy difference between the *S*, *P* and *D* electron levels. For the 3.9 nm ZnO nanocrystals, we find ϵ_P-ϵ_S = 300 meV and ϵ_D-ϵ_P = 333 meV, while for the larger 4.3 nm dots ϵ_P-ϵ_S = 256 and ϵ_D-ϵ_P = 284 meV. These results are in fair agreement with the single-particle separations measured with IR absorption spectroscopy (see Section 4.5.2) [20]. Due to the size-distribution of the ZnO quantum dots in the assembly, there is a considerable overlap between the single-electron addition functions of the *S* and *P* orbitals. This is of key importance for understanding the characteristics of long-range transport, discussed in the next section.

The results obtained in PC are strikingly different (see Figure 3.8). They can only be fitted if a large Coulomb repulsion energy is taken into account: $E_{ee}(d)$ is 220 and 130 meV for the quantum dots of 3.9 and 4.3 nm, respectively. As a consequence, the single-electron addition curves $\Delta Q(S^0 \rightarrow S^1)$ and $\Delta Q(S^1 \rightarrow S^2)$ are clearly separated, and the overlap with $\Delta Q(S^2P^0 \rightarrow S^2P^1)$ is very strong. Thus, at a given electrochemical potential (for instance V = -0.6 V) a considerable fraction of the (largest) quantum dots contain an electron in a *P* orbital, while the smallest quantum dots have no or one electron in the *S* orbitals. As a result of the large charging energy observed in PC, the electron number is considerably smaller than in ZnO nanocrystal assemblies permeated with water (see Figure 3.4).

E_{ee} in PC is 100-200 meV which is considerably larger than in aqueous electrolytes. The dielectric constants of water (81) and PC (64) are almost similar and

cannot explain this difference. We believe that adsorption of protons on the ZnO surface can strongly reduce the values of E_{pol} and E_{ee}.

In order to fit the differential capacitance functions obtained in PC, an additional broadening effect on the single-electron energy levels has to be taken into account. The origin of this broadening of the single-electron energy level distribution is not clear. Because of the weak screening of the Coulomb repulsion, it is possible that electron-electron repulsion between adjacent quantum dots cannot be neglected.

3.3.2 Long-range electron transport

In order to measure the characteristics of long-range electron transport in the ZnO quantum-dot assemblies, the electrochemically gated transistor is used. At a given electrochemical potential, thus a given $\langle n \rangle$, a small potential drop is applied between the source and drain (V_{sd} = 1-10 mV), and the current I_{sd} is measured. We found that I_{sd} is linearly dependent on V_{sd} for these small values of V_{sdD} [15]. The linear conductance, $G = R^{-1} = I_{sd}/V_{sd}$, is presented as a function of $\langle n \rangle$ in Figure 3.9 for assemblies of 3.9 and 4.3 nm dots permeated with the phosphate buffer. Note that the conductance starts to increase from a very low value to much higher values as soon as electrons are injected into the films.

For the 3.9 nm quantum dots, the conductance increases linearly with $\langle n \rangle$, for $0 < \langle n \rangle < 2$, and for $2 < \langle n \rangle < 8$. Note that in the second range the slope of the R^{-1} and $\langle n \rangle$ plot is larger. This suggests that there are at least two regimes characterized by a different electron mobility μ. The same trends are observed with the quantum dots of 4.3 nm in size. In this case, R^{-1} increases again if $\langle n \rangle > 8$. The electron mobility can be calculated using:

$$\mu \equiv \frac{\partial \sigma}{\partial N e} = \frac{d}{eLt} \times \frac{\partial G}{\partial N} \tag{3.5}$$

Here, σ is the specific electron conductivity (S·cm^{-1}), N is the average electron density (cm^{-3}), and e is the elementary charge. L, d, and t define the ZnO bridge dimensions and represent the width and length of the insulating gap and the thickness of the ZnO layer in this gap, respectively. There are clearly two regimes with a constant mobility. For the films with 3.9 nm dots the electron mobility is 17×10^{-3} cm^2/Vs and 66×10^{-3} cm^2/Vs respectively for $0 < \langle n \rangle < 1.5$, and $2.5 < \langle n \rangle < 8$. This is equivalent to an electron diffusion coefficient or diffusivity D of 0.4×10^{-3} cm^2/s and 1.5×10^{-3} cm^2/s. In the first range, the electrons occupy predominantly *S* levels and in the second predominantly *P* levels. We in-

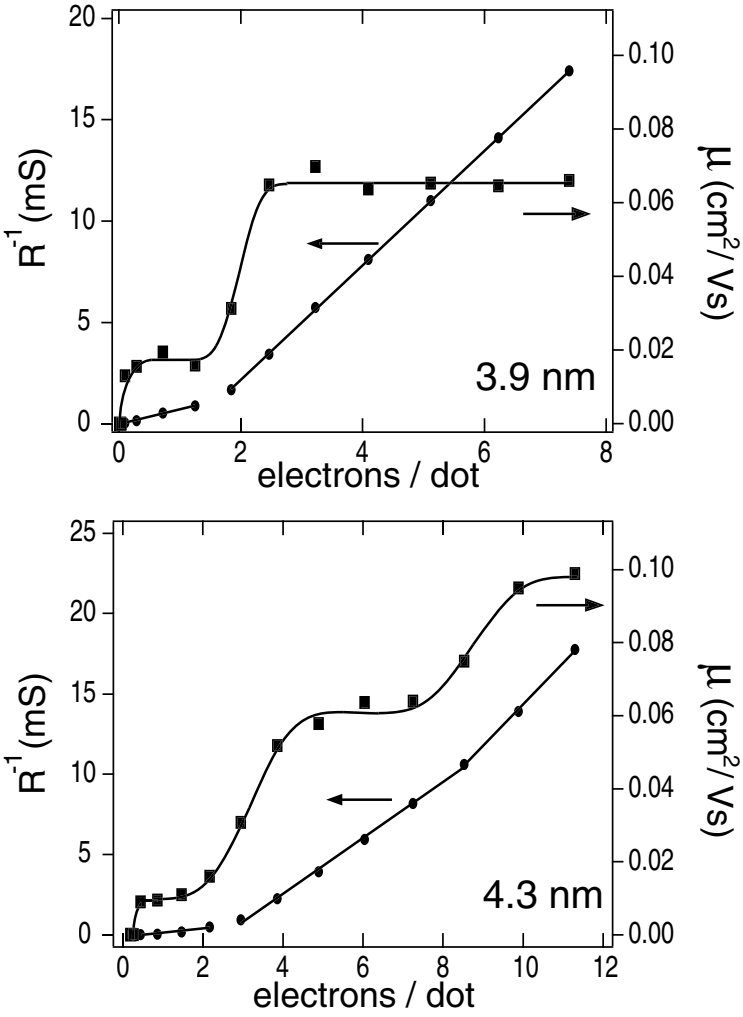

Figure 3.9: The source-drain conductance R^{-1} and the corresponding electron mobility μ as a function of $\langle n \rangle$. The electrochemically gated ZnO transistor is permeated with the phosphate buffer in this experiment. The average diameter of the quantum dots is indicated in the figure.

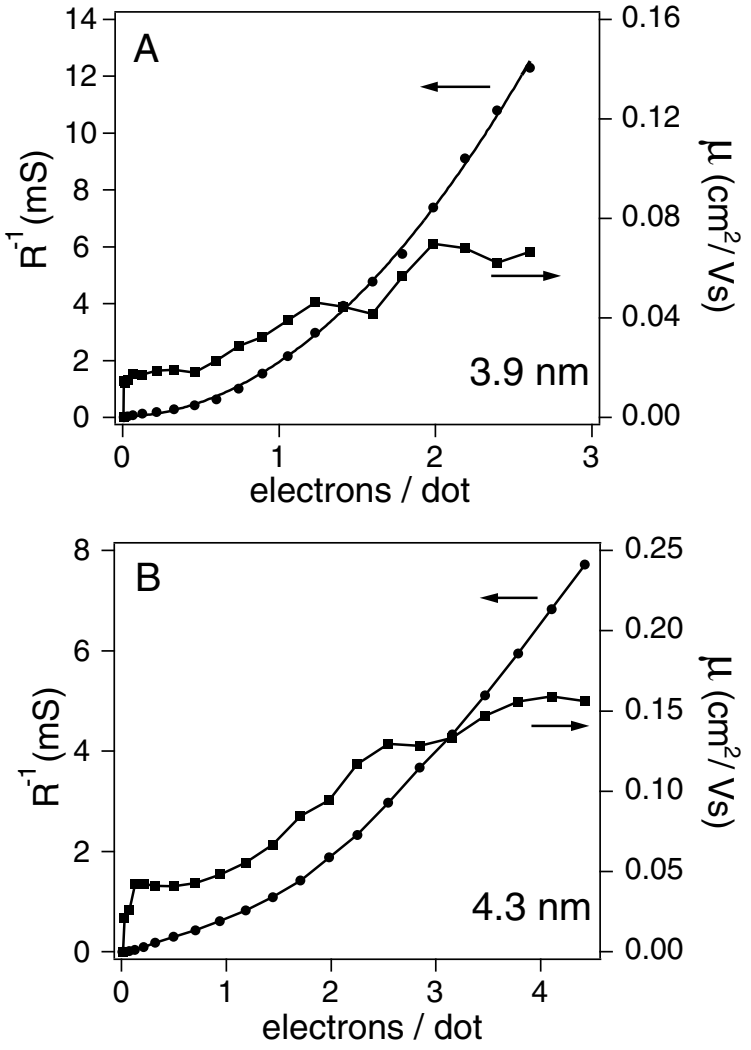

Figure 3.10: The source-drain conductance R^{-1} and the corresponding electron mobility μ as a function of $\langle n \rangle$. The electrochemically gated ZnO transistor is permeated with PC in this experiment. The average diameter of the quantum dots is indicated in the figure. The lines through the points are a guide to the eye.

fer that the mobility in the first regime corresponds to tunnelling via the *S* orbitals and in the second corresponds to tunnelling via the *P* orbitals. There is a transition range between these two regimes at around $\langle n \rangle = 2$ where both *S* and *P* orbitals are involved in long-range transport. This agrees with the overlap of the *S* and *P* density-of-states observed in the differential capacitance function (Figure 3.7). The two regimes for the electron mobility in the films with 4.3 nm dots can also clearly be seen. However, the transition range between the two regimes is broader due to the stronger overlap between the *S* and *P* density-of-states as can be seen in Figure 3.7. The variation in μ for a given regime (*S* or *P*) in the aqueous electrolyte was about 10% for electrodes from different batches, but the relative magnitude of μ_{P-P}/μ_{S-S} was always close to 4. The ratio of 4, found in every sample, can be understood more quantitatively by applying the Einstein-Smoluchowski formalism. Electron hopping between the *S* orbitals of neighboring quantum dots corresponds to a mobility:

$$\mu_{S-S} = (e/k_B T)\frac{\Delta^2}{\tau_{S-S}} \tag{3.6}$$

Δ is the length over which the electron is transferred in one tunnelling step (i.e. the diameter of the quantum dot) and τ_{S-S} the typical time between two tunnelling events. Electron diffusion via *P*-*P* orbital tunnelling corresponds to:

$$\mu_{P-P} = \gamma(e/k_B T)\frac{\Delta^2}{\tau_{P-P}} \tag{3.7}$$

Here γ accounts for the higher density of the *P* orbitals per unit of energy (γ should be 3 if the width of the *P* single-electron functions were the same as that of the *S* functions). Thus, the fact that γ is larger than 3 must be due to the larger spatial extension of the *P* orbitals with respect to the *S* orbitals. In agreement with this, tunnelling through *P* orbitals in resonant tunnelling experiments through a single quantum dot leads to a somewhat larger current increase as compared to that for tunnelling through *S* orbitals [2].

With assemblies consisting of 4.3 nm quantum dots, the electron mobility increases again for $\langle n \rangle > 8$. Although the electron mobility does not really flatten off at $\langle n \rangle = 11$, the expected ratio for μ_{D-D}/μ_{P-P} of 10/6, corresponds very well to the empirical value of 1.6 which we obtain from our results. Since Δ corresponds to the diameter of a ZnO quantum dot, we calculate that the rate for *S*-*S* orbital tunnelling in 3.9 nm particles $1/\tau_{S-S}$ is $3\times10^9 \mathrm{s}^{-1}$, while the *P*-*P* tunnel rate $1/\tau_{P-P}$ is $3.7\times10^9 \mathrm{s}^{-1}$. By comparison, the rates of resonant tunnelling in a

single-quantum dot device with metal/dot tunnel barriers of 1 nm in width are two orders of magnitude smaller [2].

We conclude that there is a weak to moderate coupling between the atom-like orbitals of the quantum-dot building blocks. In Chapter 2 we showed that long-range electron transport in ZnO quantum-dot assemblies is non-coherent [8]. This means that the electron wave functions do not extend over several quantum dots: tunnelling occurs by step-wise tunnelling from dot to dot.

In Figure 3.10 the linear conductance and the calculated electron mobility in PC is presented as a function of $\langle n \rangle$. R^{-1} increases with increasing $\langle n \rangle$ but unlike the result for assemblies permeated with water, quantum steps cannot easily be distinguished. The line through the data points is a guide to the eye. For the assembly with 3.9 nm ZnO nanocrystals, the mobility gradually increases for $0 < \langle n \rangle < 3$. A range with a constant mobility is not found here. This behavior can be understood by comparison of Figure 3.7 and 3.8. The filling of the *S* levels with a second electron overlaps strongly with the filling of the *P* levels. Therefore, the electron mobility changes much more gradually from *S*-*S* tunnelling via *S*-*P* tunnelling to *P*-*P* tunnelling. The results with an assembly of 4.3 nm dots, however, suggest that there are again two regimes, i.e. tunnelling via the *S* orbitals for $0 < \langle n \rangle < 1$ and tunnelling via the *P* orbitals for $2.5 < \langle n \rangle < 4.5$. In between these two ranges there is again a gradual increase in the electron mobility due to larger overlap of the *S* and *P* single electron functions.

Remarkably, the electron mobilities are two to three times larger than for quantum-dot films permeated with water. Similar results were reported in another study [15]. The increased mobility in quantum-dot films permeated with PC compared to films permeated with water must be due to subtle changes in the tunnelling barriers between the quantum dots. Since the rate of tunnelling depends exponentially on the width (W) and the height (V) of the barrier, $\tau_{-1} \sim exp(-W\sqrt{8m_eV/\hbar^2})$, subtle microscopic changes in the structure of the film will have measurable effects on the long-range mobility. For instance, the strong affinity of water for the ZnO surface might lead to a $Zn(OH)_2$ layer between two ZnO nanocrystals in the assembly which will increase the width of the tunnelling barrier. The adsorption of protons on the ZnO surface may also lead to changes in the height or width of the tunnelling barrier between two nanocrystals.

In our quantum-dot films, structural disorder is mainly related to the dispersion in the size of the quantum dots. The fact that we do not find a conductor-to-insulator transition, theoretically expected in the potential range at around $\langle n \rangle = 2$, is due to the simultaneous filling of *S* and *P* orbitals. For quantum-dot films permeated with aprotic solvents, the electron-electron repulsion energy seems to

enlarge the effects of the size-dispersion. As a result, the mobility increases gradually as $\langle n \rangle$ increases above two (see Figure 3.10B). Structural disorder in the quantum-dot assembly, and thus in the tunnelling distances, may also have a dispersive effect on the electron mobility (see Equations 3.6 and 3.7).

3.3.3 Temperature dependence of the electron transport

Here, we report on the temperature dependence of the electron transport through an assembly of ZnO quantum dots. We have studied a porous assembly of ZnO nanocrystals permeated with an aqueous electrolyte solution (the phosphate buffer with pH = 8) and two aprotic electrolyte solutions, 0.1 M tetrabutylammonium perchlorate in ethanol and in propylene carbonate. We have measured the conductance G of the quantum-dot assembly between a source and drain electrode in a broad temperature range between room temperature and the melting points of the solvents (156 K for ethanol and 224 K for propylene carbonate). Since $\langle n \rangle$ is independently controlled, the temperature dependence of the conductance gives direct information on the temperature dependence of the electron mobility in the assembly of quantum dots. Thus, the effect of several phenomena, such as the energy mismatch between electron energy levels due to a dispersion in the size of the quantum dots and the Coulomb repulsion between the electrons in a quantum dot can be studied.

The striking difference between a ZnO quantum-dot assembly permeated with an electrolyte solution with water or with an aprotic electrolyte solvent such as ethanol or propylene carbonate is demonstrated in Figure 3.11. For nanocrystals with an average diameter of 4.3 nm, $\langle n \rangle$ can reach eleven if the assembly is permeated with water. However, $\langle n \rangle$ is at most three and four for PC and ethanol, respectively. This was also observed for quantum dots of different sizes (see Section 3.3.1). These results indicate that the electric charging energy, corresponding to the addition of an electron to a ZnO quantum dot, is much larger if the assembly is permeated with an aprotic solvent. This is confirmed by measurements of the differential capacitance for electron injection as a function of the electrochemical potential showing that the electric charging energy is smaller than $k_B T$ for assemblies permeated with water, but 4-6 times $k_B T$ for an aprotic solvent (see Section 3.3.1).

Figure 3.12 shows the source-drain conductance of a ZnO quantum-dot assembly permeated with ethanol as a function of the accumulation potential. The conductance increases promptly as soon as electrons are injected in the assembly. The conductance can increase by four orders of magnitude in the stability range

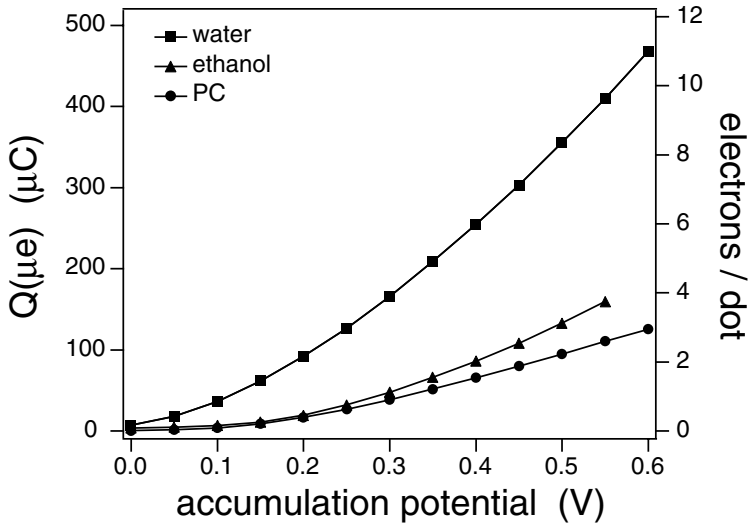

Figure 3.11: The electron charge injected in an assembly of ZnO quantum dots (average diameter of the quantum dots is 4.3 nm) as a function of the accumulation potential of the assembly. The assembly has been permeated with an aqueous electrolyte solution and with the two aprotic solutions, i.e. ethanol and propylene carbonate. The corresponding average number of electrons per quantum dot $\langle n \rangle$ is obtained from the injected charge and the number of quantum dots in the film (see Section 2.5).

of the assembly. Similar results have been obtained with films permeated with propylene carbonate and water (see Section 2.3.2). This strongly indicates that the injected electrons occupy delocalized atom-like orbitals, not localized band gap states. This has been confirmed by optical and near-infrared spectroscopy (see Section 3.3.1) [20, 21]. A typical plot of the electron mobility in ethanol as a function of increasing electron number is shown as an inset in Figure 3.12: the mobility increases gradually with $\langle n \rangle$, which is very similar to the results in propylene carbonate (see Section 3.3.2). A striking difference between aqueous and aprotic electrolyte solutions is that with aprotic electrolyte solutions the conductance and mobility of the quantum-dot film depend strongly on the temperature.

Figure 3.13*A* shows the conductance as a function of $1/k_BT$ measured with an assembly of ZnO quantum dots (4.3 nm in diameter) permeated with PC. The data were acquired between 293 K and the melting point of PC (224 K). The results obtained below the melting point of PC are not very reproducible, probably due to mechanical damage of the quantum-dot film and the film/metal contacts. The plots correspond to different accumulation potentials and thus to different

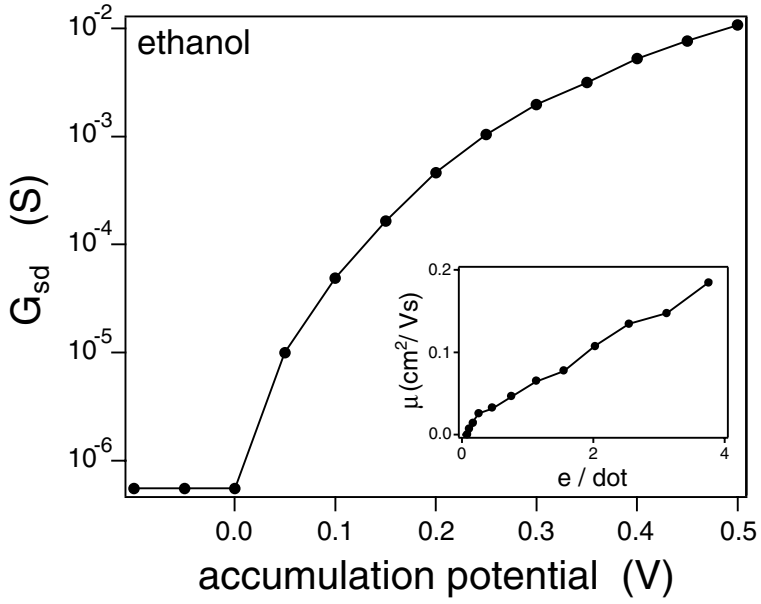

Figure 3.12: The conductance of an assembly of ZnO quantum dots permeated with an ethanol electrolyte solution (average diameter of the quantum dots is 4.3 nm) measured between a source and drain electrode as a function of the accumulation potential. Inset: The electron mobility as a function of the electron occupation number of the quantum dots.

electron occupation numbers ($1.2 < \langle n \rangle < 3$). In all cases, the logarithm of G_{sd} decreases linearly with $1/k_BT$ in the range $40 < 1/k_BT < 50$. The data acquired at 224 K in PC are positioned slightly above the linear fits. The results show that the conductance increases exponentially with increasing T; the thermal activation energy obtained for the slope of the plots is 81 meV ($\pm$10 meV) for $\langle n \rangle$ = 1.2 and 101 meV for the maximum occupancy of the assembly; i.e. $\langle n \rangle$ = 3. The results obtained with assemblies permeated with ethanol are very similar (Figure 3.13*B*); the thermal activation energy varies from 100 meV (for $\langle n \rangle$ = 0.8) to 122 meV ($\langle n \rangle$ = 3.5). Our results seem to indicate that the thermal activation energy increases slightly with increasing occupation of the quantum dots.

Thermally activated long-range charge carrier transport has been observed in molecular crystals [22], self-assembled super-lattices of gold [23] and cobalt [24] nanocrystals, and assemblies of CdSe quantum dots [10]. The thermal activation energy obtained from the temperature dependence of the conductance varied between 10 and 200 meV depending on the system studied. The results are com-

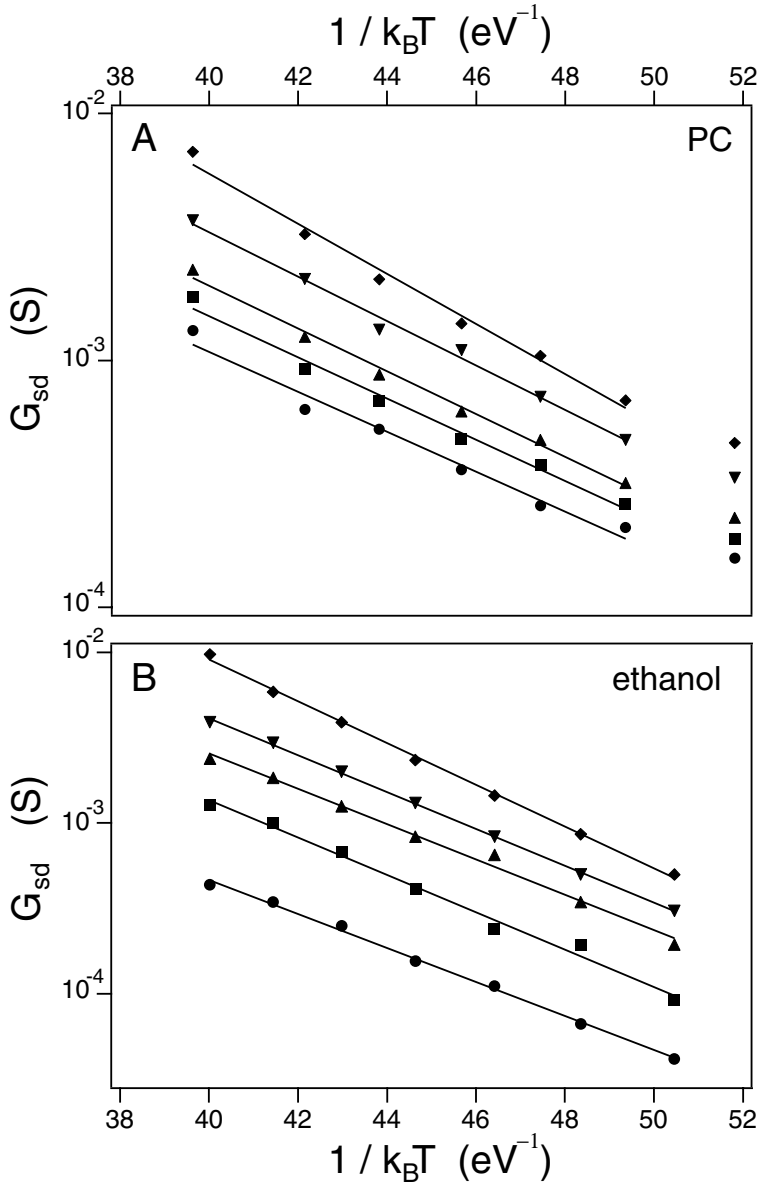

Figure 3.13: The source-drain conductance of an assembly of ZnO quantum dots (average diameter of the quantum dots is 4.3 nm) permeated with propylene carbonate (Fig. 3.13*A*) or with ethanol (Fig. 3.13*B*) as a function of $1/k_BT$. The plots are obtained with different accumulation potentials and thus different electron occupation in the quantum dots. Fig. 3.13*A*: $\langle n \rangle$ is 1.2 (●), 1.5 (■), 1.8 (▲), 2.2 (▼) and 3.0 (◆) respectively. Fig. 3.13*B*: $\langle n \rangle$ is 0.8 (●), 1.2 (■), 1.7 (▲), 2.0 (▼), and 3.5 (◆) respectively.

monly explained in terms of the orthodox Coulomb-blockade model in which the thermal activation energy found in the conductance is assigned to the electrical charging energy, $\frac{e^2}{C}$ needed to add an electron to a molecule, a metallic nanocrystal or a semiconductor quantum dot in the assembly. The conductance of a ZnO quantum-dot assembly permeated with water is independent of the temperature (5-35°C) showing that, in this case, the electric charging energy is smaller than k_BT. It also shows that the energy mismatch between the *S* type conduction levels of adjacent quantum dots (which is due to the dispersion in size of the ZnO nanocrystals) is so small that it does not lead to thermal activation of electron transport. Thus, the strong temperature-dependence of the conductance of ZnO nanocrystal assemblies reported here must be assigned to the electric charging energy; i.e. the Coulomb-blockade effect. The electric charging energy is close to 100 meV for films permeated with ethanol or propylene carbonate, independent of the nature of the charge-compensating positive ions used in the film.

It is not entirely clear why the electric charging energy is much smaller if the film is permeated with water: the dielectric constants of the solvents are not very different. We conjecture that charge screening by protons chemisorbed on the surface of the ZnO nanocrystals or even intercalated in the ZnO lattice may lead to a very effective screening of the charge of the electrons. Our results suggest that the electric charging energy increases slightly with increasing electron occupation of the ZnO quantum dots. This is in contrast to the standard, i.e. constant capacitance model. Microscopic models which account both for dielectric polarization and electron-electron repulsion may be helpful in understanding such details [3].

3.4 Conclusions

We have used an electrochemically gated transistor to study the storage and transport of electrons in an assembly of ZnO quantum dots permeated with a PC or ethanol solution and we compared the results with those obtained in an aqueous solution in Chapter 2. The differential capacitance of the films shows the subsequent filling of the *S* and *P* orbitals of the ZnO quantum dots. Optical measurements show that localization of electrons in surface states between the HOMO and LUMO is not important.

The distribution in the size of the dots leads to an overlap between the *S* and *P* density-of-states. The electron-electron Coulomb repulsion in films permeated with an aqueous electrolyte is very small ($\leq k_BT$), but is much larger in propylene carbonate and ethanol (100-200 meV). As a result, less electrons per quantum

dot can be injected in the films permeated with propylene carbonate and ethanol. From the low-temperature measurements we found a thermal activation energy of 80-120 meV. These values correspond quite well to the Coulomb repulsion of 100-200 meV found in the charging experiments.

The electron mobility measured as a function of the electron occupation per quantum dot in water shows that there are two quantum regimes in the long-range transport of electrons. In the first regime transport occurs by tunnelling from dot to dot via the *S* orbitals, in the second regime tunnelling occurs via the *P* orbitals. In propylene carbonate and ethanol, mixed tunnelling regimes are observed, due to the fact that the strong Coulomb repulsion energy masks the effects of quantum confinement.

It is shown that the quantum properties of individual nanocrystals in an assembly define the characteristics of long-range electron transport. The screening of the charge of the electrons depends strongly on the choice of the liquid permeating the porous assembly. On the basis of this work it would be interesting to investigate the role of the permeating electrolyte solution in more detail.

References

[1] U. Banin, Y.W. Cao, D. Katz and O. Millo, *Nature* **400**, 542 (1999).

[2] E.P.A.M. Bakkers, Z. Hens, A. Zunger, A. Franceschetti, L.P. Kouwenhoven, L. Gurevich and D. Vanmaekelbergh, *Nano Lett.* **1**, 551 (2001).

[3] A. Franceschetti, A. Williamson and A. Zunger, *J. Phys. Chem. B* **104**, 3398 (2000).

[4] Y.M. Niquet, G. Allan, C. Delerue and M. Lannoo, *Appl. Phys. Lett.* **77**, 1182 (2000).

[5] C.B. Murray, C.R. Kagan and M.G. Bawendi, *Science* **270**, 1335 (1995).

[6] C.B. Murray, S.H. Sun, W. Gaschler, H. Doyle, T.A. Betley and C.R. Kagan, *IBM J. Res. Dev.* **45**, 47 (2001).

[7] F. Remacle and R.D. Levine, *ChemPhysChem* **2**, 20 (2001).

[8] A.L. Roest, J.J. Kelly, D. Vanmaekelbergh and E.A. Meulenkamp, *Phys. Rev. Lett.* **89**, 036801 (2002).

[9] C. Wang, M. Shim and P. Guyot-Sionnest, *Appl. Phys. Lett.* **80**, 4 (2002).

[10] D.S. Ginger and N.C. Greenham, *J. Appl. Phys.* **87**, 1361 (2000).

[11] M. Drndić, M.V. Jarosz, N.Y. Morgan, M.A. Kastner and M.G. Bawendi, *J. Appl. Phys.* **92**, 7498 (2002).

[12] N.Y. Morgan, C.A. Leatherdale, M. Drndić, M.V. Jarosz, M.A. Kastner and M.G. Bawendi, *J. Appl. Phys.* **66**, 075339 (2002).

[13] E.A. Meulenkamp, *J. Phys. Chem. B* **102**, 5566 (1998).

[14] P. Hoyer and H. Weller, *J. Phys. Chem.* **99**, 14096 (1995).

[15] E.A. Meulenkamp, *J. Phys. Chem. B* **103**, 7831 (1999).

[16] V. Noack, H. Weller and A. Eychmüller, *Phys. Chem. Chem. Phys.* **2003**, *5*, 384.

[17] P. Hoyer, R. Eichberger and H. Weller, *Ber. Bunsen-Ges. Phys. Chem.* **97**, 630 (1993).

[18] S.R. Morrison, *Electrochemistry at semiconductor and oxidized metal electrodes*, 1 ed., London, Plenum Press., 401 (1980).

[19] L.E. Brus, *J. Chem. Phys.* **79**, 5566 (1983).

[20] A. Germeau, A.L. Roest, D. Vanmaekelbergh, E.A. Meulenkamp, G. Allan and C. Delerue, *Phys. Rev. Lett.* **90**, 097401 (2003).

[21] A.L. Roest, et al. accepted for publication in *ChemPhysChem*.

[22] W.A. Schoonveld, J. Wildeman, D. Fichou, P.A. Bobbert, B.J. van Wees and T.M. Klapwijk, *Nature* **404**, 977 (2000).

[23] M. Dorogi, J. Gomez, R. Osifchin, R.P. Andres and R. Reifenberger, *Nature* **52**, 9071 (1995).

[24] C.T. Black, C.B. Murray, R.L. Sandstrom and S. Sun, *Science* **290**, 1131 (2000).

Chapter 4

Optical transitions between the conduction levels of ZnO quantum dots studied by IR absorption spectroscopy

In this chapter, we report on the optical transitions in few-electron artificial atoms strongly confined in ZnO nanocrystals with a diameter between 3 and 6 nm. We use an assembly of weakly coupled ZnO nanocrystals in which electrons are injected electrochemically; the average electron number is obtained from the injected charge and the number of quantum dots in the assembly. The charged ZnO nanocrystals show broad spectra in the near IR, the shape and total absorption intensity being determined by the average electron number only. The spectra can be explained by taking into account the allowed electric dipole transitions between the atom-like orbitals of the ZnO nanocrystals and the size-distribution of the nanocrystals in the sample.

4.1 Introduction

Colloidal insulating nanocrystals should form ideal hosts for strongly-confined artificial atoms, i.e. configurations of one to a few electrons occupying the conduction energy levels of the nanocrystal. Such nanocrystals can be obtained in molar quantities by wet chemical synthesis with increasing control of the size, shape and surface electronic properties [1–3]. The dimensions below 10 nm ensure strong quantum confinement of the electrons corresponding to confinement energies in the 0.1 to 1 eV range. For comparison, artificial atoms defined by lithography in bulk semiconductor crystals have dimensions of a few tens to hundreds of nanometers and, accordingly, show much weaker confinement effects in the 1 meV range [4]. The interest in studying artificial atoms in the strong confinement regime is due to the fact that quantum confinement and Coulomb exchange interactions all depend in a different way on the dimensions of the nanocrystal host [5]. Thus, in strongly confined systems, as yet unobserved electrical and optical properties should emerge.

A major problem in studying strongly-confined artificial atoms is control of the *electron occupation number* N, i.e. the number of electrons per quantum dot. For example, a transistor consisting of a single CdSe quantum dot, mounted between two electrodes, with a gate to control the electron or hole number has been reported [4, 6]. The technological sophistication required for the fabrication of such a device, however, limits experimental studies by a wide research community. We have fabricated *assemblies* consisting of ZnO nanocrystals with a diameter between 3 and 6 nm in which the electron number can be controlled by the electrochemical potential. In long-range electron transport, two quantum regimes have been observed corresponding to tunneling between the *S* orbitals for an electron occupation number lower than two, and tunneling between the *P* orbitals for an electron occupation number between two and eight (see Section 2.3.2) [7].

Here, we report a study of the optical properties of artificial atoms created in such an assembly. We detect the optical transitions between the conduction levels in artificial atoms consisting of one to ten electrons by absorption spectroscopy in the near infrared. The importance of this work for the physics of strongly-confined systems is twofold. First, we demonstrate that, by gradually increasing the electron number in the ZnO nanocrystals, the contribution of each individual electronic transition to the absorption spectrum can be identified, despite the size dispersion in the assembly. Until now, only the optical transition between the lowest (*S*) and second lowest (*P*) conduction level in CdSe and ZnO quantum dots has been reported [8, 9]. Second, the present method of spectroscopy directly

provides the single-particle energy separations between the electron levels. This is due to the fact that electrons are transferred from one conduction level to another (keeping the electron number constant), the repulsion energy between two electrons being nearly independent of the orbitals that they occupy [10]. This is in firm contrast to conventional absorption and luminescence spectroscopies that probe transitions between valence and conduction levels; the polarization and the Coulomb-interaction energies of the electron and hole play an important role in the energy of the transition [10] making the extraction of single-particle energies more complex and subject to uncertainties.

In this chapter, we first discuss the single-electron conduction levels in ZnO quantum dots and the optical transitions between these levels. The electron energy levels are calculated with a tight-binding method and compared with the effective mass approximation. The tight-binding model calculations are done by the collaborating group of Dr. Allan and Dr. Delerue (IEMN, Lille). The effective mass approximation calculations are done by Dr. Germeau (Utrecht University) [11]. These orbitals are then used to calculate the oscillator strengths of the electric dipole transitions between the energy levels. Next, we show the IR absorption spectra obtained with an assembly of ZnO quantum dots with an increasing average occupation number $\langle n \rangle$. We present a model that calculates the distribution of the electrons over the quantum dots in the assembly for a given electrochemical potential, and their corresponding IR absorption. By fitting this model to the absorption spectra we obtain the relative oscillator strengths of *S-P*, *P-D*, *P-S*' and *D-F* transitions and single-particle energy separations between these levels. The oscillator strengths and single-particle energy separations are compared with the predictions from the tight-binding model.

4.2 Single-electron conduction levels in ZnO quantum dots

An electron added to an otherwise neutral ZnO nanocrystal will occupy the conduction state of lowest energy, i.e. the Lowest Unoccupied Molecular Orbital (LUMO). This orbital is strongly delocalized. The electron is thus confined in the limited space of the nanocrystal. The kinetic confinement energy, i.e. the difference in kinetic energy between an electron in a nanocrystal and a bulk crystal, due to confinement of its wave function, can be calculated with a number of methods. In order of increasing sophistication, we have the particle-in-a-box approximation, the quasi-particle-in-a-box (effective mass) approximation [12–14] and various tight-binding [15, 16] and pseudo-potential methods [5, 17]. We use

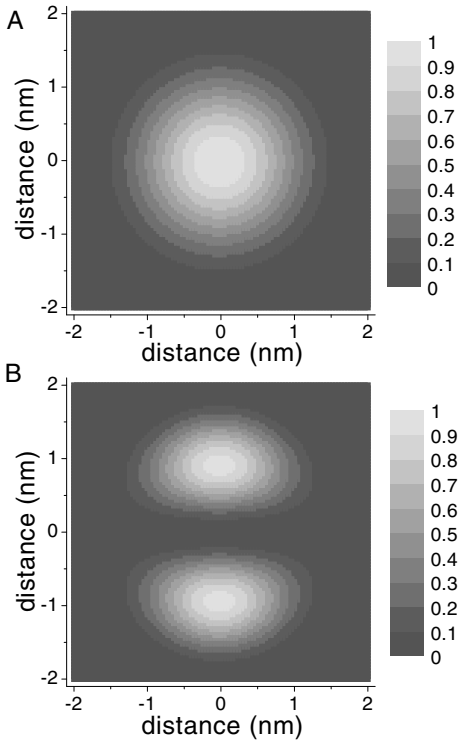

Figure 4.1: The square of the wavefunctions with quantum numbers (A) $n = 1$, $l = 0$ (*S*, LUMO) and (B) $n = 1$, $l = 1$ (*P*), calculated with the effective mass approximation [11] for a spherical ZnO quantum dot (4 nm in diameter) as a function of the position in the quantum dot.

here the quasi-particle-in-a-box approximation to calculate the single-particle kinetic confinement energy levels in a spherical ZnO quantum dot, and compare the results with the outcome of more sophisticated tight-binding calculations. The polarization (i.e. dielectric) confinement energy of an electron in a quantum dot is considered in Section 4.5.

In the effective mass approximation, the interaction of a (conduction) electron with a periodic lattice potential (i.e. the scattering by core atoms) is described by replacing the (bare) mass m of the electron, by an effective mass m^* (called the mass of the quasi-electron). This approximation holds for a weak periodic potential and small values of the wave vector k. To describe the confinement of the electron by the nanocrystal, we assume, as a first approximation, that the quasi-electron potential is constant inside the quantum dot and infinitely high outside the

dot. The eigenfunctions of the electron (in spherical coordinates) are a product of the spherical harmonics $Y_l^m(\theta, \varphi)$ [18], which only depend on the spherical coordinates θ and φ, and the spherical Bessel functions $j_l(k_{l,n}r)$ [18], which only depend on the radial distance r. With l we denote the quantum number for the angular momentum, m is the quantum number for the projection of the angular momentum and the quantum number n distinguishes different energy levels with equal angular momentum. The atom-like electron orbitals *S*, *P*, *D*, *F* have $l = 0, 1, 2, 3$. The orbital with quantum numbers $l = 0$ and $n = 2$ is denoted with *S*'. The wave vector $k_{l,n}$ is determined from the condition that the wave function vanishes at the surface, i.e. $j_l(k_{l,n}R) = 0$ where R is the radius of the particle. Due to this condition, the energy levels no longer form a continuum; instead we obtain quantized energy levels with discrete wave vectors k. Figure 4.1 shows the square of the modulus of the *S* and *P* eigenfunctions. The energy levels of the eigenfunctions are given by [18]:

$$\varepsilon_{l,n} = \frac{\hbar^2 k_{l,n}^2}{2m^*} \tag{4.1}$$

This is for an electron with an effective mass m^*. From this expression and the boundary condition $j_l(k_{l,n}R) = 0$, we obtain that the kinetic confinement energy of the electron depends on the radius R of the quantum dot as $1/R^2$, and is inversely proportional to the effective mass.

Figure 4.2 shows the kinetic confinement energy of the lowest conduction levels, obtained with the effective mass approximation (symbols), as a function of the diameter of the ZnO quantum dot. With an electron effective mass equal to the bulk electron effective mass ($m^* = 0.2m$ [19]), the kinetic confinement energy of the lowest energy level is of the order of 500 meV for a quantum dot with a diameter of 4 nm. In order of increasing energy we find *S*, *P*, *D*, *S*' and *F* levels. The degeneracy (including spin states) of an energy level l is given by $2(2l + 1)$.

A more accurate description of the confinement of the electron to a quantum dot is based on the assumption that the potential barrier is finite. The tunnelling decay length r_t is given by [18]:

$$r_t = \frac{\hbar}{2\sqrt{2m(E_{vac} - E)}} \tag{4.2}$$

Here E_{vac} is the energy of the electron at rest in vacuum and E is the energy of the electron in a given conduction energy level. With a typical value $(E_{vac} - E)$ of 4 eV [19], the decay length is 0.5 nm. Because the kinetic confinement

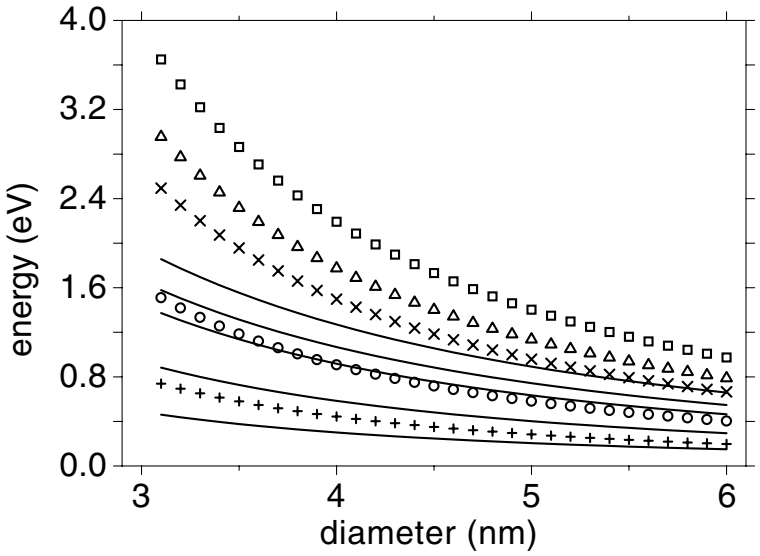

Figure 4.2: The kinetic confinement energy of the lowest conduction levels of a ZnO quantum dot, as a function of the diameter of the quantum dot. The solid lines were calculated with the tight-binding model (from bottom to top; *S*, *P*, *D*, *S'*, *F*), the symbols are the predictions from the effective mass approximation [11]: *S* (+), *P* (○), *D* (×), *S'* (△) and *F* (□).

energy strongly depends on the volume in which the electron is confined, carrier penetration outside the crystallite reduces the energy of the electron considerably (25-50% for quantum dots with a diameter from 2-7 nm).

Because the effective mass approximation holds only for small kinetic energy values (such that the kinetic energy is quadratic in the wave vector k), smaller quantum dots are described less accurately by the effective mass approximation. Advances in computational physics have enabled the direct solution of the single electron Schrödinger equation for larger quantum dots [17]. The Hamiltonian of the electron in this system accounts for the interaction of the electron with the atoms of the nanocrystal and the surroundings of the quantum dot. However, to find solutions of the Schrödinger equation, approximations are necessary and the success of a method depends on the choice of the approximations. Two methods frequently used are the pseudopotential method and the tight-binding theory. The use of the pseudopotential method to calculate the energy levels in insulating nanocrystals has been advocated by Zunger and coworkers [10, 20–22]. Here,

we will consider a tight-binding model to calculate the conduction levels in ZnO quantum dots, developed by the Lille group.

In the tight-binding model, one assumes that the quantum-dot wave functions are built up from a relatively small number of localized atomic wave functions. In this approximation we exclude the delocalized (i.e. ionized) atomic wave functions. Here we describe a tight-binding approximation built up from the Zn and O atomic wave functions *s*, *p*, *d* and *s'* (including spin-orbit coupling) [23]. One assumes that the electron can be described by a single-particle Hamiltonian and that this single-particle Hamiltonian for the quantum dot is the same as the bulk single-particle Hamiltonian. This means that the scattering of the electrons with the lattice is assumed to be the same as in a bulk crystal. The tight-binding parameters are fitted to the bulk ab-initio pseudopotential energy dispersion curve and the experimental electron and hole effective masses. The advantage of this semi-empirical approach is that only a relevant selection of wave functions needs to be calculated; this enables one to perform calculations for a large quantum dot (up to 15 nm). Dangling bonds at the surface are saturated by pseudo-hydrogen atoms. Figure 4.2 shows the kinetic confinement energy of the lower conduction levels of a ZnO quantum dot (solid lines). The lowest conduction level has *S* symmetry and is two-fold degenerate. In order of increasing energy we have a *P* level (six-fold degenerate), a *D* level (ten-fold degenerate), an *S'* level (two-fold degenerate), and a *F* level (fourteen-fold degenerate). From Figure 4.2 it is clear that the size-dependence of the kinetic confinement energy calculated with tight-binding theory is weaker than that calculated with the effective mass approximation ($1/R^2$). Furthermore, the relative difference between tight-binding theory and effective mass approximation is larger for higher values of energy. For quantum dots with a diameter of 6 nm for instance, the difference between tight-binding and effective mass is only 30% for the *S* level and already 50% for the *F* level. The different results here are mainly due to the infinite energy barrier used in the effective mass approximation. Higher energy levels have a larger spatial extension in tight-binding. In the effective mass method the infinite energy barrier does not allow for such a spatial extension.

Figure 4.2 shows the square of the *S* and *P* wave functions in a ZnO quantum dot as a function of the position, obtained with the tight-binding model. The wave functions obtained with the tight-binding method show the periodicity of the lattice. A detailed comparison of Figure 4.1 and 4.2, shows that the tight-binding orbitals decay more slowly from the center towards the crystal surface than the orbitals obtained with the effective mass approximation with infinite walls.

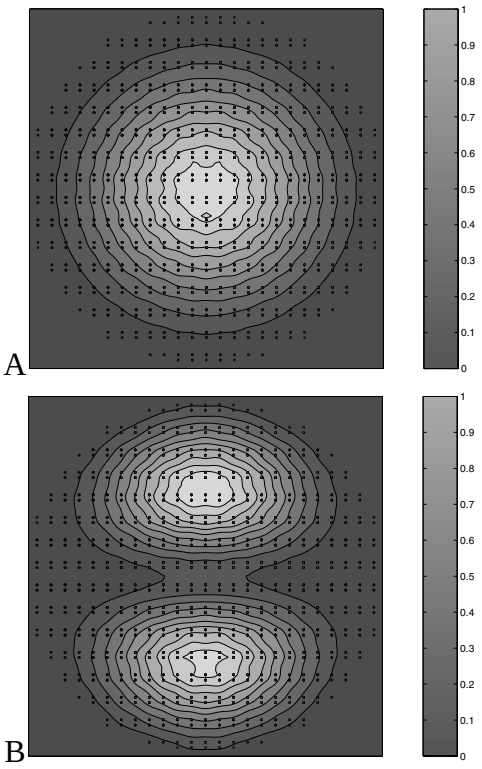

Figure 4.3: The square of the *S* wave function ($n = 1, l = 0$) (A) and *P* wave function ($n = 1$, $l = 1$) (B), of a nearly spherical ZnO quantum dot (4.2 nm in diameter) calculated with the tight-binding model as a function of the position. The atoms of the ZnO nanocrystal are indicated with points; note the crystal facets.

4.3 Optical transitions between the conduction levels in ZnO quantum dots

4.3.1 Electric dipole transitions in a one-electron dot and oscillator strengths

We consider the electric dipole absorption rate A_{it} (i.e. the amount of energy absorbed per unit time which equals the transition probability per unit time multiplied by the photon energy) for one quantum dot containing one electron. The rate of a transition between electron states i and t is proportional to the incident energy intensity per unit frequency $J_{(E_t - E_i)}$ (i.e. the photon flux per unit frequency times the photon energy). With $E_i(E_t)$, we denote the energy of the electron in the initial (final) state. The absorption rate A_{it} is averaged over the polarization

directions of incident radiation. This absorption rate is given by (Fermi's golden rule) [18]:

$$A_{it} = \frac{\pi e^2}{2mc\epsilon_0} f_{it}\ J_{(E_t - E_i)} \tag{4.3}$$

Here m is the mass of the electron, c the speed of light and ϵ_0 the permittivity of vacuum. In this expression f_{it} denotes the oscillator strength between the electron states i and t, defined as:

$$f_{it} = \frac{2m}{\hbar^2}(E_t - E_i)|\langle i|z|t\rangle|^2 \tag{4.4}$$

The matrix element of the z coordinate of the dipole operator is represented by $e\langle i|z|t\rangle$. An interesting feature of the oscillator strength is that its sum over a complete set of (normalized) basis states t (without spin states) equals one, i.e.:

$$\sum_t f_{it} = 1 \ \ (\text{sum rule}) \tag{4.5}$$

This property can be used to check if all allowed transitions have been accounted for. It holds for a Hamiltonian that contains the momentum operator only in the kinetic energy operator. A complete set of electron basis states is a collection of states t such that every possible electron state can be written as a unique linear combination of these basis states. In the tight-bing model, a set of basis states contains not only conduction and free states but also valence states, with an energy smaller than the *S* conduction level. Because spin-orbit coupling is only a slight perturbation (meV) the sum rule holds to a good approximation for our tight-binding model.

From IR absorption measurements we obtain the transition rate between two *energy levels*, not between two *electron states*. We therefore must calculate the *average* absorption rate $\bar{A}_{ll'}$ for one quantum dot that contains one electron, due to transitions between the *energy levels* E_l and $E_{l'}$. We assume that each energy level E_l contains $2(2l+1)$ electron states (including spin states). With this assumption

$$\bar{A}_{ll'} = \frac{1}{2(2l+1)} \sum_i \sum_t A_{it} \tag{4.6}$$

Here the sum runs over all states i with energy E_l and all states t with energy $E_{l'}$; A_{it} is given by Equation 4.3.

For an electron with a spherically symmetric Hamiltonian, the electric dipole transition rules are $\Delta l = \pm 1, \Delta j = 0, \pm 1$ and $\Delta m_j = 0, \pm 1$ [24]. With j we

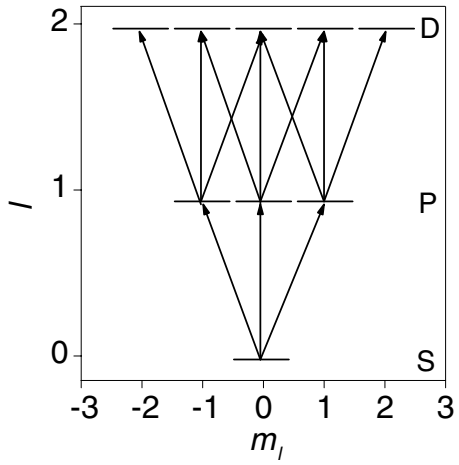

Figure 4.4: The allowed transitions between the *S*, *P* and *D* conduction levels in a spherical quantum dot.

denote the quantum number for the total angular momentum (spin + orbit) and m_j, the quantum number for its projection. In other words, the matrix element $\langle i|z|t\rangle$ is non zero only for the transitions between states with $\Delta l = \pm 1, \Delta j = 0, \pm 1$ and $\Delta m_j = 0, \pm 1$. If spin-dependent interactions are negligible, the spin is conserved and the transition rules become $\Delta l = \pm 1, \Delta j = \pm 1$ and $\Delta m_l = 0, \pm 1$. Figure 4.4 shows the allowed transitions between the orbitals corresponding to the *S*, *P* and *D* levels.

In the effective mass approximation, which possesses full rotational symmetry for spherical structures, the oscillator strengths of forbidden transitions are zero. Although the tight-binding model does not have full rotational symmetry, the oscillator strengths of forbidden transitions are orders of magnitude smaller than the allowed transitions. The selection rules for transitions in our quantum dots are thus determined by the symmetry of the envelope wave functions.

The average oscillator strength due to transitions between the energy level E_l and $E_{l'}$ is given by:

$$\bar{f}_{ll'} = \frac{1}{2(2l+1)} \sum_i \sum_t f_{it} \tag{4.7}$$

Here the sum adds up all states i (t) with energy E_l ($E_{l'}$). Figure 4.5 shows the summed oscillator strength $2(2l+1)\bar{f}_{ll'}$ for the allowed transitions between the lowest energy levels in a spherical ZnO quantum dot. A polarization term (see

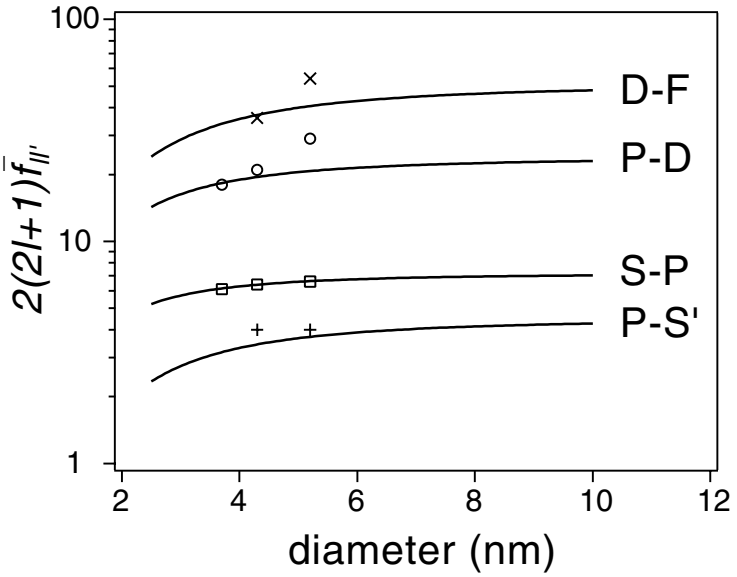

Figure 4.5: The summed oscillator strength $2(2l+1)\bar{f}_{ll'}$ for the allowed transitions is shown as a function of the diameter of the ZnO quantum dot. The values obtained by tight-binding theory (including spin-orbit coupling) are represented as solid lines. The symbols represent results obtained from the fit of our data: *S-P* (□), *P-D* (○), *D-F* (×) and *P-S'* (+). The experimental *S-P* oscillator strength is set equal to the theoretical value. This allows us to compare the other experimental oscillator strengths with the theoretical values in a relative way.

section 4.5.1) is not taken into account. Because the polarization energy Σ_l of an electron in our dots depends only slightly (of the order of meV) on l (*S* or *P*) [21], we assume that a polarization term will only slightly disturb the oscillator strengths we obtain here.

We remark that the average oscillator strength $\bar{f}_{ll'}$ is of the order of 4 for the *S-P* transition. The average oscillator strength for both the *P-D* and the *D*-F transitions has a similar value. It will become clear in the following sections that the selection rules and the calculated oscillator strengths are of importance to understand the absorption spectra of few electron artificial atoms.

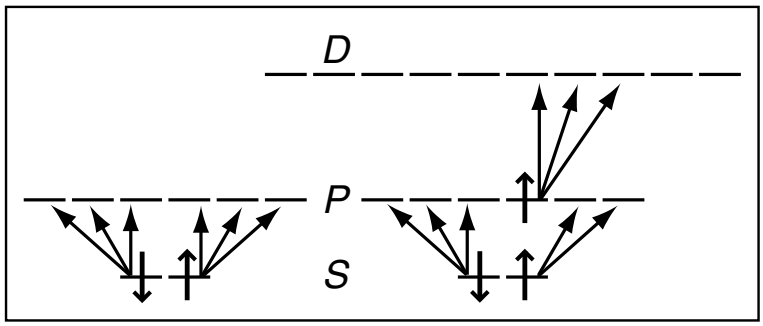

Figure 4.6: Schematic representation of the possible transitions in a quantum dot occupied by two (left, S^2P^0 configuration) and three (right, S^2P^1 configuration) electrons. Every arrow represents one possible transition.

4.3.2 Transitions in a dot containing more than one electron

We now consider the absorption rate by one quantum dot with more than one electron, due to transitions between the *S* and *P* energy levels. Because the transition probability per quantum dot per photon is much smaller than one ($\simeq 10^{-15}$ see Section 4.4.2), and in the approximation that the absorption rate is independent of spectator electrons. Spectator electrons with an energy $E_{l'}$ occupy states that cannot be occupied by an electron that makes a transition to this energy level. Obviously, we take this into account. Here we mean the influence of spectator electrons on the absorption rate beside this Pauli-effect. Because the Coulomb interaction $J_{l,l'}$ between electrons depends only by a few meV on the quantum number l, l'(*S* or *P*) [21], we assume that spectator electrons only slightly disturb the absorption rate. Exchange interaction is about an order of magnitude smaller than the Coulomb interaction [21] and we neglect it in the rest of this chapter.

The overall absorption rate of a quantum dot with two electrons, due to a transition from electron state *S* to *P* is $2A_{SP}$. If three electrons are present in a quantum dot a *P* level will also be occupied. Two things change as is schematically shown in Figure 4.6. First, there is no transition possible between the occupied *S* level and the occupied *P* level with the same spin (the selection rules for the allowed transitions are explained in Section 4.3.1). While $2A_{SP}$ accounted for six possible *S*-*P* transitions, now only five possible transitions are left. The absorption by a quantum dot with three electrons (configuration S^2P^1), due to a transition between the *S* and *P* level, equals therefore $2A_{SP}(1 - 1/6)$. Second, an extra contribution to the overall absorption arises because it is now possible to excite the

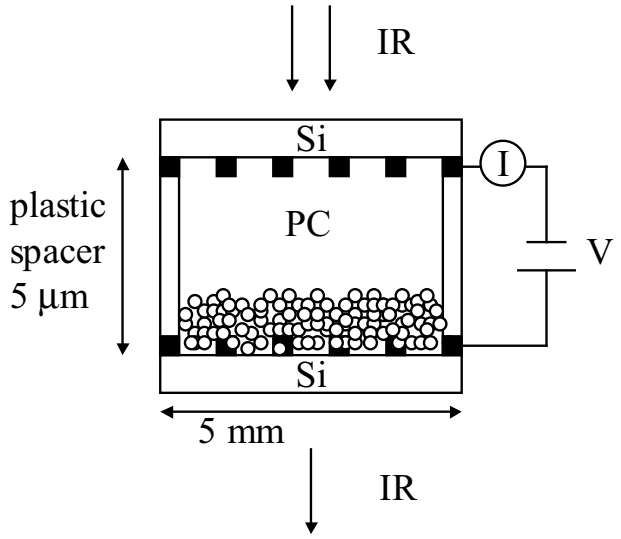

Figure 4.7: Schematic drawing of the two-electrode electrochemical cell used in IR absorption measurements on an assembly of ZnO quantum dots. The gold grid on the silicon electrodes consists of gold lines 100 nm in thickness, 1μ wide and a distance of 10 μm between the lines. The propylene carbonate electrolyte penetrates the ZnO quantum-dot layer which is about 200 nm thick.

electron in the *P* level to the *D* level with an absorption rate A_{PD}. The absorption rate A_{PD} accounts for three possible transitions from the *P* level to three *D* levels ($\Delta m_l = 0, \pm 1$, see Section 4.3.1). The overall absorption rate of a quantum dot with more than three electrons, due to a transition from electron state *P* to *D* will increase linearly with the number of electrons in the *P* levels and will decrease again if the *D* levels are occupied (more than eight electrons).

4.4 IR absorption spectra obtained with an assembly of ZnO quantum dots

4.4.1 Experimental method

In the IR absorption measurements we use ZnO quantum dots without capping, with diameters in the 3-6 nm range. The preparation of the ZnO quantum dots is described in detail in Chapter 2. A film of ZnO quantum dots, about 200 nm thick, was deposited by spin-coating a washed colloidal suspension on a substrate.

Annealing of the layer by heating to 90° C for 15 minutes removed residual alcohol from the layer. IR transparent electrodes consisted of a gold grid (100 nm thick, 1 μm wide with a distance of 10 μm between the gold lines) on a silicon substrate. The IR absorption measurements on an assembly of ZnO quantum dots were performed with a two-electrode electrochemical cell schematically shown in Figure 4.7. A negative voltage V between the work electrode (with the ZnO layer) and a counter electrode, leads to an increase in the electrochemical potential μ of the ZnO quantum-dot assembly, which becomes populated with electrons. Because of the presence of positive ions in the electrolyte solution (propylene carbonate with 0.1 M $LiClO_4$) in the pores of the film, the electric field due to electrons in the quantum dots is screened. As a result, the average electron number in the quantum dots can be quite high (up to ten electrons per dot) and the electrons are distributed uniformly over all ZnO nanocrystals in the film.

The number of electrons stored in the ZnO layer was measured by integrating the current I that flows between work and counter electrodes. The average electron occupation number $\langle n \rangle$ of a quantum dot is obtained from the total number of electrons and the number of quantum dots in the layer (see Section 2.5 for a more detailed discussion of $\langle n \rangle$). with 3 V between the work electrode and the counter electrodes, the ZnO film was no longer chemically stable. This limits the charging to a maximum of ten electrons per quantum dot, 5.2 nm in diameter and to only three electrons if the diameter is 3.7 nm. Because of IR absorption by the electrolyte, the electrolyte layer must be as thin as possible. We used cells with an optical path through the electrolyte solution of 5 μm. There was no space for a reference electrode. This means that we could not measure the electrochemical potential μ of the ZnO layer. All IR absorption measurements were performed with a Bio-rad FTIR spectrometer FTS-40, at room temperature in a nitrogen-purged environment.

4.4.2 Results

Figure 4.8 shows the increase in the absorption (i.e. the fraction of the incident intensity absorbed) of an assembly of ZnO quantum dots (the average diameter is 4.3 nm in (a) and 3.7 nm in (b)) due to charging with on average $\langle n \rangle$ electrons per quantum dot. The corresponding voltage V between the electrode with the quantum dots and the counter electrode is also indicated. The charging of the electrode takes a few seconds. The change in the IR absorption is instantaneous with the charging of the electrode. The dips in the absorption spectrum at 3000, 1800, 1300, and 1100 cm^{-1} are also found in the absorption spectrum of the propylene

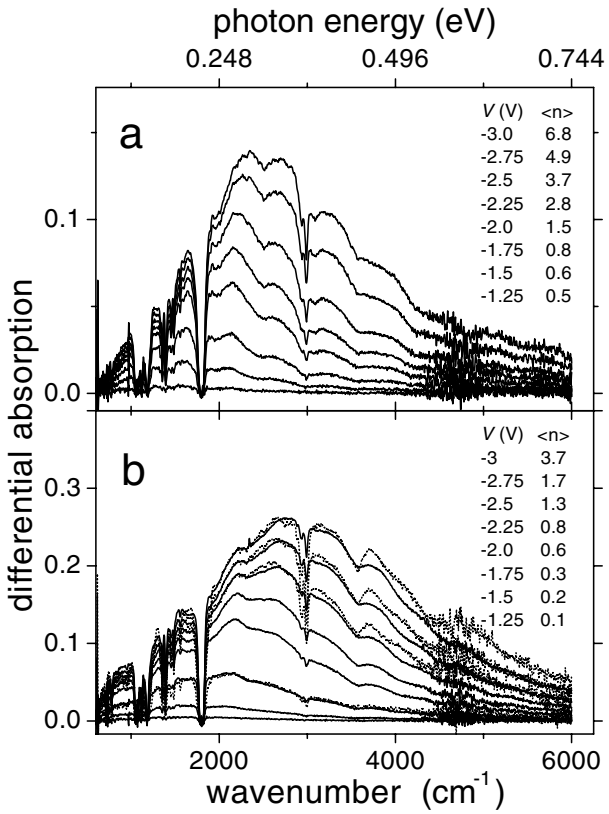

Figure 4.8: The increase in the IR absorption of an assembly of ZnO quantum dots due to injection of an increasing number of electrons. The applied potential between the ZnO layer and counter electrode, and the corresponding average occupation number are indicated. For quantum dots with an average diameter of 4.3 nm (a), the average occupation number $\langle n \rangle$ can be as high as 7, whereas for quantum dots with an average diameter of 3.7 nm (b), $\langle n \rangle$ reaches only 4. The excellent reproducibility is shown by the results obtained with another sample (dotted line) in (b).

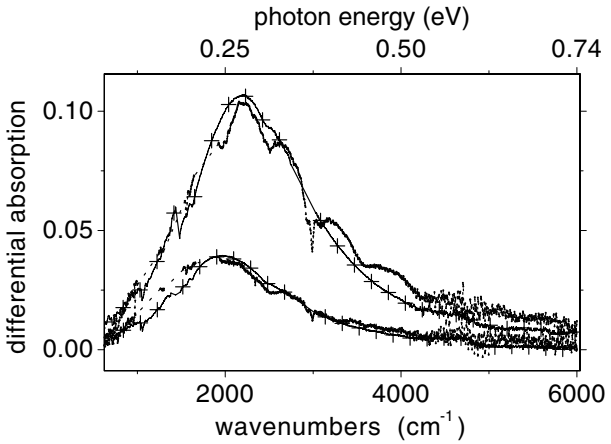

Figure 4.9: The increase in the IR absorption of an assembly of ZnO quantum dots (average diameter is 4.3 nm) due to charging with on average 0.8 and 3.7 electrons per quantum dot. The solid line with symbols (+) shows the increase in the absorption of a colloidal solution of the same ZnO quantum dots, due to excitation with UV light (λ = 300 nm) [11]. The latter spectra are very similar to these obtained with ZnO quantum-dot assemblies. The sharp features, below 2000 cm^{-1}, due to the electrolyte solution have been omitted for clarity.

carbonate electrolyte. The assembly can reversibly store up to seven electrons per quantum dot (4.3 nm in diameter) without chemical degradation. The energy of the absorbed photons is in the range of a few 100 meV, which corresponds to the energy difference between the conduction levels in ZnO quantum dots in the 3 to 6 nm range (see Section 4.2). The width of the absorption peak, is essentially due to the size-distribution. In confirmation of this, the spectra obtained at cryogenic temperatures show the same width [11]. From Figure 4.8 it is clear that for increasing occupation number $\langle n \rangle$, the absorption and the width of the absorption peak increase while the position of the absorption peak shifts to higher energies. This strongly suggests that several different optical transitions become possible when $\langle n \rangle$ increases. From a comparison of the spectra shown in Figure 4.8a and b, it is clear that the absorption peak is at larger energy for the smaller quantum dots. This is a clear manifestation of the size confinement of the energy levels. Figure 4.8b shows that the absorption spectra obtained with two different samples are nearly identical; the reproducibility is of the order of a few percent. The reproducibility in the measurement of the charge for two different samples is better than 10% for voltages smaller than 3 V.

The IR absorption due to charging of the *S* level of the ZnO assembly (average diameter 5.2 nm, layer thickness 200 nm) is about 10% of the incident flux. The IR intensity throughout the sample is thus almost constant. From the absorption due to charging, the incident IR photon flux of 10^{18} photons per second per centimeter square (over a photon energy range of 400 meV) [25] and the total number of quantum dots (10^{14}), we obtain an *S*-*P* average absorption cross section σ = 0.1 ± 0.05 nm^2. The absorption cross section σ is defined as the ratio of the absorption rate per quantum dot (energy per time unit) and the incident energy intensity (energy per time and per surface unit). With an average *S*-*P* oscillator strength $\bar{f}_{S-P}$ = 3.5 (see Figure 4.5), we obtain from Equation 4.3 for a quantum dot with a diameter of 5 nm, σ = 0.09 $\pm$ 0.03 nm^2, in excellent agreement with the experimental value.

Figure 4.9 shows the increase in the IR absorption of an assembly of ZnO quantum dots (average diameter is 4.3 nm) due to charging with an average of 0.8 and 3.7 electrons per dot. The symbols (+) show the increase in the absorption of a *colloidal solution* of the same ZnO quantum dots, due to photochemical charging with UV light [11]. The spectra are normalized accounting for the different number of quantum dots in the optical path in the case of an assembly and a dispersion. It can be seen that the spectra obtained with solutions have a very similar shape to those obtained with the assembly. This suggests that the electronic coupling between the ZnO quantum dots in an assembly is weak. In addition, the red shift of the onset of the exciton absorption of an assembly of ZnO quantum dots, compared to that of a colloidal solution of ZnO quantum dots is very small (see Section 2.2.1). This further supports the idea that the coupling between neighbouring quantum dots is weak. Finally, the magnitude of the mobility of electrons in an assembly of ZnO quantum dots, due to tunnelling between conduction band levels, also indicates a weak overlap of the conduction band orbitals of neighbouring quantum dots (see Section 2.3.2). We will therefore assume that orbital overlap in an assembly of ZnO quantum dots is not important in the electric-dipole transitions; thus, uncoupled quantum dots will be considered (Section 4.5).

4.5 Quantitative analysis of the spectra

4.5.1 A statistical model

Tunnelling of an electron between two conduction orbitals of adjacent ZnO quantum dots occurs on a time scale of nanoseconds [7]. On the other hand, the relaxation of electrons from a higher to a lower conduction level is much faster (of

the order of a picosecond [26]). We therefore can assume that the electrons injected in a ZnO assembly are in electrochemical equilibrium. In this section we present a model for the absorption of a collection of quantum dots with a given size-distribution and an electrochemical potential μ. We calculate the electron occupation N of a quantum dot of radius R for a given electrochemical potential μ and temperature T. From the expression for the absorption of a quantum dot with N electrons given in section 4.3.2, we calculate the total absorption in a ZnO assembly as a function of the average occupation number $\langle n \rangle$.

The occupation number N of a quantum dot with radius R (present in a quantum-dot assembly with electrochemical potential μ) is most easily obtained by considering the electron addition energy μ_N. $\mu_N(R)$ is defined as the energy required to add one electron to a quantum dot (with radius R) containing $N-1$ electrons in the conduction band, i.e.:

$$\mu_N = E_N - E_{N-1} \tag{4.8}$$

Here E_N is the internal energy of a quantum dot with N excess electrons. If $\mu_N < \mu$ the occupation will be N and if $\mu_N > \mu$ the occupation will be $N-1$. An electron added to a quantum dot with $N-1$ electrons occupies a conduction state with a kinetic confinement energy ε_N (see Section 4.2). The charge of this electron, with wave function ψ, will polarize the quantum dot and its environment; as a result there is a polarization energy:

$$\Sigma_N = \frac{1}{2} \int -e|\psi(\mathbf{r})|^2 V(\mathbf{r})\, d\mathbf{r} \tag{4.9}$$

Here V is the electrostatic potential due to the charge distribution $-e|\psi(\mathbf{r})|^2$. Furthermore, there is the repulsion energy J_N due to the Coulomb interaction with the $N-1$ conduction electrons already present in the dot:

$$J_N = \int -e|\psi(\mathbf{r})|^2 V_{N-1}(\mathbf{r})\, d\mathbf{r} \tag{4.10}$$

Here $V_{N-1}(\mathbf{r})$ is the potential due to the $N-1$ other electrons in the dot. For our quantum dots, the exchange energy is about an order of magnitude smaller than the Coulomb interaction [21] and we disregard it here. The electron addition energy μ_N can then be written as:

$$\mu_N(R) \simeq \varepsilon_N(R) + \Sigma_N(R) + J_N(R) \tag{4.11}$$

The polarization energy Σ_1 for a spherically symmetric electron distribution with respect to the polarization energy in a bulk crystal is a function of the radius of the quantum dot R and the macroscopic static dielectric constant $\epsilon_{in}(\epsilon_{out})$ inside (outside) the quantum dot [10], $\Sigma(\frac{1}{R}, \epsilon_{in}, \epsilon_{out})$. Because the polarization energy Σ_l and the Coulomb interaction between two electrons $J_{ll'}$ is very weakly dependent on the quantum number l and because correlation effects between electrons are also in the order of a few meV [12, 13, 15, 21] we make the approximation:

$$\Sigma_N \simeq \Sigma \tag{4.12}$$

and

$$J_N \simeq 2(N-1)\Sigma \tag{4.13}$$

In this way we obtain an *electric* addition energy $\mu_N^{el}(= \mu_N - \varepsilon_N)$ for $N-1 \rightarrow N$:

$$\mu_N^{el}(R) = (2N-1)\Sigma \tag{4.14}$$

Equation 4.14 corresponds to the constant capacitance of electron addition better known as the 'standard model' which has been used frequently for metallic nanocrystals and larger (10 to 100 nm) semiconductor quantum dots defined by lithography [4, 27]. Σ corresponds then to $\frac{e^2}{2C}$ with C the capacitance of the quantum dot in a given electronic structure. In the fitting of the IR absorption spectra, the value of the charging energy $\Sigma(R)$ is an important fit parameter since it determines the electron occupation of a ZnO quantum dot of radius R in the assembly. We denote the total electron addition energy for the transition $N-1 \rightarrow N$ as:

$$\mu_N(R) = \varepsilon_N(R) + (2N-1)\Sigma(R) \tag{4.15}$$

With $\Sigma(R)$ is $\frac{A}{2R}$ (A is the fitting constant in our procedure). This is in accordance with Equation 4.14, where Σ is a constant parameter that can be adjusted to fit the experimental absorption spectra. The Coulomb interaction between two neighbouring charged quantum dots in our electrolyte (with a Debye screening length L of 1.2 nm) is of the order of 10^{-1} meV and is disregarded.

At 0 K, all single-particle energy levels in a quantum dot with radius R that have an addition energy $\mu_N(R)$ smaller than the electrochemical potential μ will be filled. With R_N we denote the radius of the smallest quantum dot with N electrons. This radius is the solution of the equation:

$$\mu = \mu_N(R_N) \tag{4.16}$$

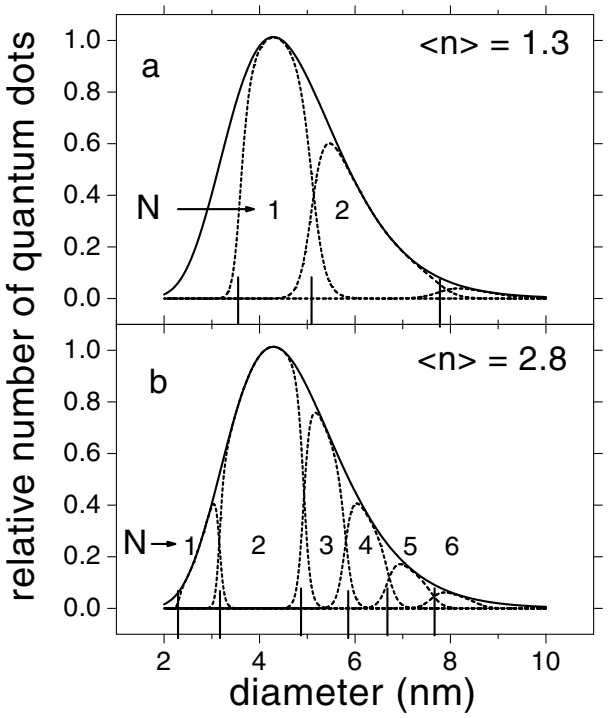

Figure 4.10: The solid line shows the size-distribution of a collection of quantum dots with an average diameter of 4.3 nm. The smallest diameters of a quantum dot with N electrons at a temperature of 0 K, $2R_N$, are indicated for an average occupation number $\langle n \rangle$ = 1.3 (a)) and $\langle n \rangle$ = 2.8 (b)). The dashed lines show the distribution of quantum dots from one to six electrons at room temperature.

The addition energy $\mu_N(R)$ is calculated with tight-binding values for the kinetic confinement energy $\varepsilon_N(R)$, and an electric addition energy $\mu_N^{el} = (2N-1)\frac{A}{2R}$. Equation 4.16 is third order in R_N and is solved numerically with an accuracy of a few percent. Because μ_N increases with N and decreases with R, $R_{N+1} > R_N$. Quantum dots with a radius R between $R_N < R < R_{N+1}$ have N electrons. By calculating the radii R_N for $N = 1$ to $N = 32$ (*F* like shell filled), we obtain the occupation number for all quantum dots in our assembly.

As an example we show in Figure 4.10 the calculated electron occupation in a collection of ZnO quantum dots with a size-distribution around the average diameter of 4.3 nm. The size-distribution which we need to explain the IR spectra is larger than the size-distribution found with TEM (see Section 2.5). It was also larger than the distribution used to fit the charging experiments in water in Chap-

ter 3 but the same as the distribution used to fit the charging experiments in PC. The radii R_N are indicated for an average occupation number $\langle n \rangle$ = 1.3 (a) and $\langle n \rangle$ = 2.8 (b). At a temperature T, the occupation of a single-particle level ε_N in a quantum dot with radius R is given by the Fermi-Dirac distribution:

$$\frac{1}{1 + e^{\frac{\mu_N(R) - \mu}{kT}}} \tag{4.17}$$

Since we now have the occupation number as a function of the diameter of the quantum dot, we can calculate the IR absorption by each class of quantum dots with a given occupation number. The absorption of the sample due to charging of the quantum dots is of the order of 10^{-1}. This means that the IR intensity throughout the sample is nearly constant. From the incident IR photon rate (10^{18} photons per second [25]) and the number of quantum dots in the sample (10^{14}), we obtain an *S-P* absorption rate of the order of 10^3 photons per quantum dot per second. It has been shown that an electron excited to a *P* level decays to the *S* level on a picosecond time scale [26]. Thus, all IR photons are absorbed by the quantum dots with the ground state electronic configuration at a given temperature. Furthermore, since the absorption probability per quantum dot per photon is much smaller than one ($\simeq 10^{-15}$), the cross section for a quantum dot with N electrons is the sum of the cross sections of a quantum dot with one single electron, with the assumption that the cross section for a transition is independent of spectator electrons.

4.5.2 Discussion of the results

We now have a model for the absorption of a collection of ZnO quantum dots with a given size-distribution, electrochemical potential μ and temperature T. From the occupation number as a function of the diameter of the quantum dot, we also calculate the average occupation number $\langle n \rangle$ as a function of the electrochemical potential. Experimentally we have measured the change in the IR absorption due to charging of the quantum dots with on average $\langle n \rangle$ electrons per dot. We now compare the experimental absorption spectra with those obtained from our model. The fitting parameters in our model are i) the values for the single-particle energy levels ε_N, ii) the averaged oscillator strengths $\bar{f}_{ll'}$ of the allowed transitions and iii) the electric charging energy $\mu_N^{el} = (2N-1)\frac{A}{2R}$ and iv) the size-distribution of the quantum dots.

Figure 4.11 presents the IR absorption spectra for a quantum-dot assembly (diameter of ZnO nanocrystals is 4.3 nm) for $\langle n \rangle$ equal to 0.8 and 4.9. With in-

creasing $\langle n \rangle$, the maximum of the absorption spectrum shifts to higher energy, and the integrated intensity of IR absorption increases markedly. The latter observation indicates that the number of optical transitions increases when, besides the *S*, the *P* orbitals also become occupied with electrons. We have fitted the absorption curves, with the energy separations between the *S*, *P*, *D*, *S'* and *F* electron orbitals and the relative oscillator strengths for the allowed transitions as adjustable parameters. Figure 4.11a shows the results for a low average occupation number; $\langle n \rangle = 0.8$. The absorption curve can be accounted for by the allowed S-P transition ($\Delta l = +1$). For $\langle n \rangle = 0.8$, the sample consists of nanocrystals with 0, 1 and 2 electrons (see Figure 4.10). The contribution of the nanocrystals with one electron corresponds to the right shoulder in the fit. Note that the dip at 3000 cm^{-1} is due to absorption by the electrolyte.

The contribution of the nanocrystals with two electrons provides the left part. The energy separation between the *S* and *P* electron levels is obtained from the position of the absorption peak. There is also a very small contribution from a *P-D* transition; a small fraction of the (largest) quantum dots in the assembly has an electron in a *P* orbital. We remark that the absorption at the high energy side cannot be explained by a *P-S'* transition. The width of the *S-P* transition is about 200 meV. This width is due solely to the size-distribution of the quantum dots. This is supported by measurements at 10 K, which provide absorption spectra that are nearly identical to those at room temperature [11]. A similar width has been observed for the *S-P* transition in a sample of CdSe quantum dots [8].

For $\langle n \rangle = 4.9$, transitions from the *P* orbitals to higher-lying orbitals are expected. Figure 4.11b shows the contributions of the different transitions to the overall absorption spectrum. The main contribution comes from the *P-D* optical transition ($\Delta l = +1$). The steps on the high-energy side are due to the contributions of sub-ensembles of nanocrystals, each with a distinct number of *P* electrons. Each sub-ensemble has a different average diameter, and thus gives a contribution at slightly different energy due to the effect of quantum confinement. The energy separation between the *P* and *D* levels is obtained from the position of the peak in the absorption spectrum. The average oscillator strength of the *P-D* transition $\bar{f}_{PD}$ (relative to that of the *S-P* transition) is obtained from the intensity of the absorption curve. The results are discussed below. The remaining *S-P* contribution is merely due to the subset of the smallest quantum dots in the sample. Note that the maximum of the *S-P* contribution is therefore at higher energy than that of the *S-P* contribution for $\langle n \rangle = 0.8$. Moreover, despite the fact that there are two electrons in the *S* orbitals, the total *S-P* intensity has decreased markedly compared to that for $\langle n \rangle = 0.8$. At $\langle n \rangle = 4.9$ most particles have already three electrons in a

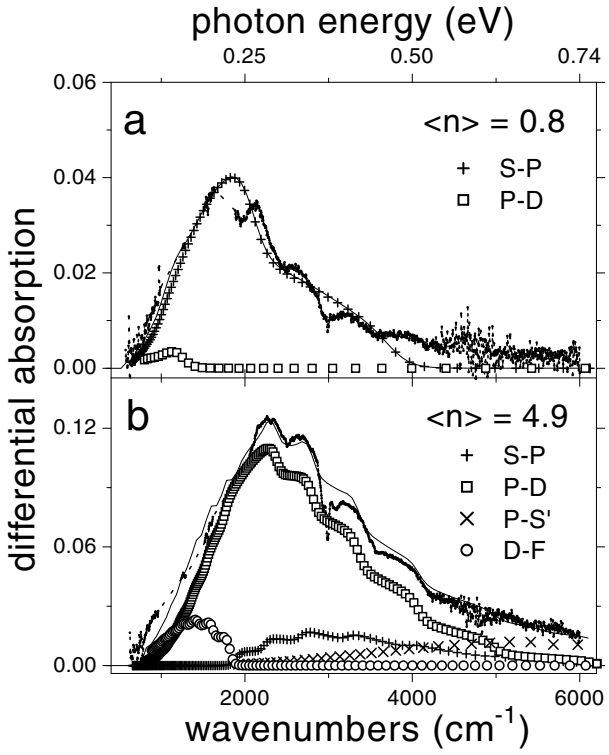

Figure 4.11: Absorption spectra (black lines) and corresponding fits (thin black lines) for a ZnO quantum-dot assembly (average diameter is 4.3 nm) at low and higher occupation $\langle n \rangle$. The spectrum for $\langle n \rangle = 0.8$ can be fitted with an S-P (+) and a *P-D* (□) transition. The spectrum for $\langle n \rangle = 4.9$ can be fitted with the *S-P* (+) and *P-D* (□) transition and the *P-S*' ($\times$) and *D-F* ($\circ$) transitions.

P level, which strongly reduces the *S-P* intensity (see Section 4.3.2). The subset of largest particles have occupied *D* orbitals. This leads to a *D-F* contribution ($\Delta l = +1$) at the low energy side of the spectrum. The tail at the high energy side of the spectrum is merely accounted for by the allowed *P-S*' ($\Delta l = -1$) transitions.

Figure 4.12 shows the increase in absorption of a quantum-dot assembly due to charging with on average 4.9 electrons, and the predictions from our model for different values of the electric addition energy, i.e. $\mu_N^{el} = (2N-1)\frac{A}{2R}$. From section 4.5, we know that the electric addition energy determines the electron occupation of the quantum dots (with radius R) in the assembly. From a fitting of the experimental spectra we obtain $\frac{A}{R}$ = 116 ± 45 meV. From the differen-

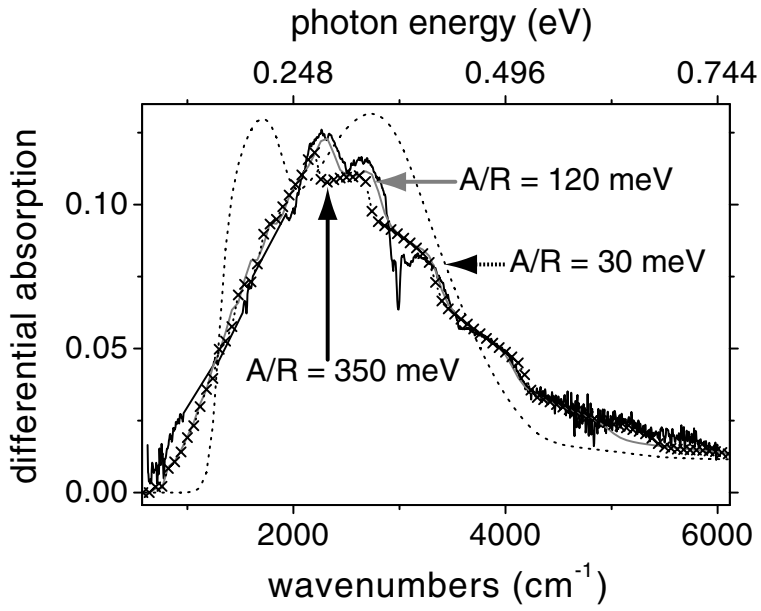

Figure 4.12: The increase in absorption of a quantum-dot assembly (average diameter is 4.3 nm) due to charging with on average 4.9 electrons, is shown with the predictions from our model for different values of the parameter $\frac{A}{R}$ ($\mu_N^{el} = (2N-1)\frac{A}{2R}$). The first peak in the curve with $\frac{A}{R} = 125$ meV is due to *D*-*F* transitions, the second peak mainly due to *P*-D transitions.

tial capacitance function obtained in a three-electrode system, it is found that the electric charging energy for a 4.3 nm quantum dot is about 130 meV (E_{ee} in Section 3.3.1), which is very close to the value obtained from this fitting procedure. Also the temperature dependence of electronic conduction in a ZnO assembly gives similar values for the charging energy 80-120 meV (see Section 3.3.3).

Figure 4.13 shows the absorption spectrum for a quantum-dot assembly with an average diameter of 5.2 nm. The spectrum with $\langle n \rangle = 1.4$ can essentially be fitted with an *S*-*P* transition. There is a small contribution from a *P*-*D* transition. From the fitting of this spectrum we obtain information on the energy separation between the *S* and *P* levels. The spectrum with $\langle n \rangle = 4.7$ is fitted with *S*-*P*, *P*-*D*, *P*-*S*' and *D*-*F* transitions. Because the main contribution comes from the *P*-*D* transition, we essentially obtain information on the energy separation between the *P* and *D* levels, and the oscillator strength of the *P*-*D* transition, relative to the oscillator strength of the *S*-*P* transition. The spectrum with $\langle n \rangle = 8.6$ provides

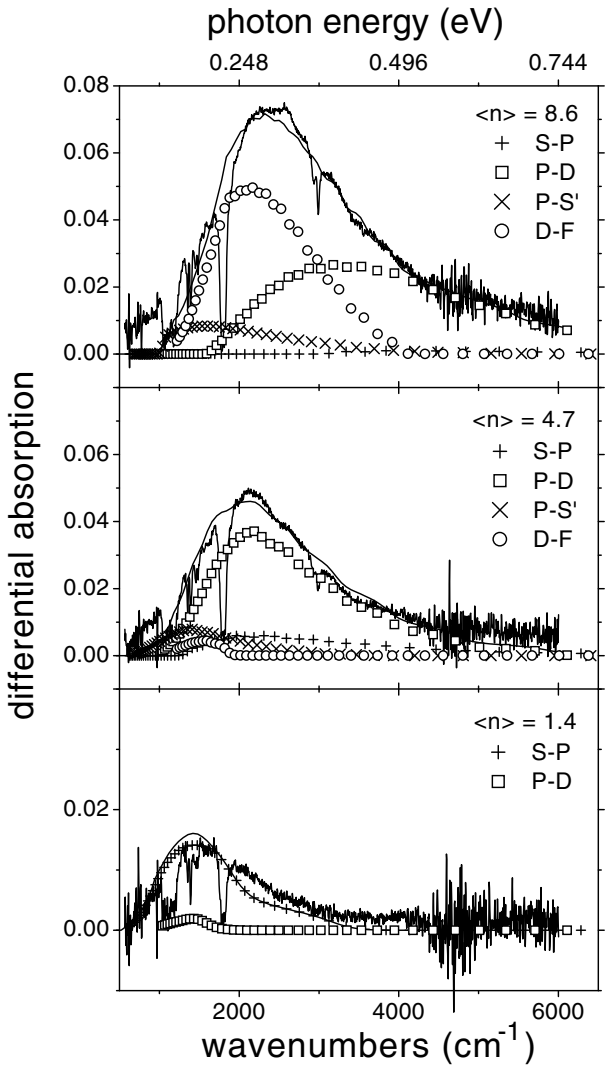

Figure 4.13: Absorption spectra (black lines) and corresponding fits (thin black lines) for a ZnO quantum-dot assembly (average diameter is 5.2 nm) at different occupation numbers $\langle n \rangle$. The spectrum for $\langle n \rangle = 1.4$ can be fitted with an *S-P* (+) and a *P-D* (□) transition. The spectra for $\langle n \rangle = 4.7$ and $\langle n \rangle = 8.6$ can be fitted with the *S-P* (+), *P-D* (□), *P-S'* (×) and *D-F* (○) transitions.

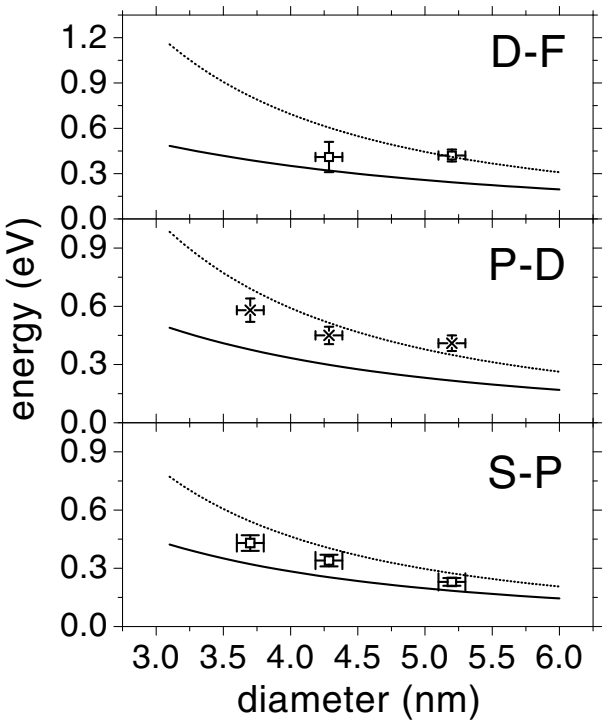

Figure 4.14: The separation between the single-electron energy levels obtained from the IR spectra (symbols) and calculated with tight-binding theory (solid lines) and effective mass approximation (dotted lines), as a function of the diameter of the ZnO nanocrystals.

information on the energy separation between the *F* and *D* levels, and the oscillator strength of the *D-F* transition, relative to the *S-P* transition. In summary, we have shown that, by fitting the IR absorption spectra for a gradually increasing occupation of the ZnO quantum dots, we obtain the relative oscillator strengths for the allowed transitions and the energy separations between the *S*, *P*, *D* and *F* levels. The contribution from *P-S*' is too broad and too weak to obtain reliable data for the *P-S*' energy separation.

We analyzed the absorption spectra for ZnO quantum dots of three different sizes: 3.7 nm $(0 < \langle n \rangle < 1.7)$, 4.3 nm $(0 < \langle n \rangle < 4.9)$, and 5.2 nm $(0 < \langle n \rangle < 8.6)$. In Figure 4.14 the single-particle energy separations that we obtain from analysis of the spectra are compared with the tight-binding values and the values obtained by the effective-mass approximation. The dependence of the *S-P* and *P-D* energy separation on the nanocrystal diameter is in line with

theory. Quantitatively, the experimental *S-P*, *P-D* and *D-F* separations are somewhat larger than the values calculated with the tight-binding model used here. The reason for this difference may be an inaccurate description of the surface of the quantum dot. Tight-binding calculations with different surface atoms passivating dangling bonds have shown that the energy levels depend on the surface termination [1, 28]. The presence of an internal electric field and deviations from the spherical shape form other possible reasons for the difference between the experimental and calculated results.

The oscillator strengths that we have obtained from a fit of the IR absorption spectra are compared with the tight-binding values in Figure 4.5. We have equated the experimental oscillator strength of the *S-P* transition to the tight-binding value. Figure 4.5 presents thus a comparison of the relative oscillator strengths for the different allowed transitions. For the quantum dots of 3.7 and 4.3 nm, we find a remarkable agreement between observed and calculated values. The oscillator strengths observed for the particles of 5.2 nm are higher than those predicted by tight-binding theory. The reason for this discrepancy is not clear.

Figure 4.10 shows the size-distribution used to fit the IR absorption spectra for quantum dots with an average diameter of 4.3 nm. The asymmetrical log-normal distribution is obtained from TEM pictures of similar quantum dots [29, 30]. The width of the size-distribution necessary to fit the IR absorption spectrum is however, much larger than the width obtained from TEM size histograms which is about 40% of the average diameter [31] (see also Section 3.3.1).

Below, we consider some phenomena which might be important in the broadening of the IR absorption spectra. It is not clear why we need an anomalous broad size-distribution to explain the width of the spectra. Spectra obtained at 10 K have a width almost identical to spectra obtained at room temperature [11]. This excludes broadening due to the absorption of phonons in the electronic transition. A coupling of the electron levels with the (fluctuating) dipoles of the solvent can very probably also be excluded. The linewidth of an IR transition between conduction levels in a quantum dot due to its lifetime ($\simeq$ a picosecond [26]) is of the order of a meV and thus cannot explain the broad spectra. Band-edge exciton emission and absorption measurements on an identical assembly of ZnO quantum dots show a similar width as obtained from IR absorption measurements. Size-selective band-edge exciton absorption measurements have shown that phonon replicas can shift the optical absorption 40 meV [32]. Capacitance measurements on a ZnO quantum-dot assembly in the same electrolyte solution as used for the IR experiments (propylene carbonate) show a size-distribution identical to that needed to explain the IR absorption spectra (see Section 3.3.1). We conjecture

that shape asymmetry [32], surface atoms [28] and changes in the local electric field (spectral diffusion) [33, 34] are factors that might determine the dispersion in the kinetic confinement energy levels ε_N and perhaps the anomalous width of the spectra.

4.6 Conclusions

In this chapter we have shown that artificial atoms can be prepared by electrochemical injection of electrons in an assembly of weakly coupled ZnO quantum dots with a diameter between 3 and 6 nm. The injected electrons occupy the conduction electron orbitals of the ZnO nanocrystals. By measuring the injected charge and the number of nanocrystals in the assembly, the average electron number $\langle n \rangle$ can be obtained. We have shown that up to ten electrons can be confined in the ZnO nanocrystals; this means that artificial atoms with S^1, S^2, S^2P^1, ... electron configurations can be studied. On the other hand, the same artificial atoms can also be prepared using a colloidal solution of ZnO nanocrystals in ethanol. Formation of an electron-hole pair by absorption of a photon with energy in the near UV and subsequent removal of the hole by electron transfer from an ethanol molecule lead to ZnO nanocrystals with one or more electrons in the conduction orbitals.

Using absorption spectroscopy in the near-IR we have studied the optical transitions in these artificial atoms. With a gradual increase in the electron number, the contributions of the *S-P*, *P-D*, *D-F* and *P-S*' allowed electric dipole transitions to the total absorption spectrum could be identified. The absorption spectra can be understood by a model based on the allowed electric dipole transitions between the atom-like conduction orbitals of the ZnO quantum dots. The distribution in the size of the ZnO nanocrystals in the sample is the most serious problem. It is accounted for by calculating the electron configuration as a function of the diameter of the quantum dots for a given average occupation number $\langle n \rangle$ assuming electronic equilibrium between the dots. In this way the experimental absorption spectra could be fitted accurately and in a self-consistent way. There is, however, one remaining problem: the size-distribution needed to explain the spectra is considerably broader than that found by analysis of TEM pictures. The relative oscillator strengths of the *S-P*, *P-D*, *D-F* and *P-S*' transitions were found to be in excellent agreement with the values calculated with the tight-binding theory. This means that the optical transitions are completely determined by the symmetry of the envelope wave functions, expressed by the quantum number l. Here,

we wish to remark that generally excitonic HOMO-LUMO transitions cannot be explained in such a simple way [35]. From the analysis, the single-particle energy separations between the *S*, *P*, *D*, and *F* levels can also be obtained.

References

[1] A.P. Alivisatios, *J. Phys. Chem.* **100**, 13226 (1996).

[2] X.G. Peng, L. Manna, W.D. Yang, J. Wickham, E. Scher, A. Kadavanich and A.P. Alivisatos, *Nature* **404**, 59 (2000).

[3] D.V. Talapin, A.L. Rogach, A. Kornowski, M. Haase and H. Weller, *Nano Lett.* **1**, 207 (2001).

[4] L.P. Kouwenhoven, D.G. Austing and S. Tarucha, *Rep. Prog. Phys.* **64**, 701 (2001).

[5] A. Franceschetti and A. Zunger, *Phys. Rev. Lett.* **78**, 915 (1997).

[6] D.L. Klein, R. Roth, A.K.L. Lim, A.P. Alivisatos and P.L. McEuen, *Nature* **389**, 669 (1997).

[7] A.L. Roest, J.J. Kelly, D. Vanmaekelbergh and E.A. Meulenkamp, *Phys. Rev. Lett.* **89**, 036801 (2002).

[8] M. Shim and P. Guyot-Sionnest, *Phys. Rev. B* **64**, 245342 (2001).

[9] M. Shim and P. Guyot-Sionnest, *Nature* **407**, 981 (2000).

[10] A. Franceschetti and A. Zunger, *Phys. Rev. B* **62**, 2614 (2000).

[11] A. Germeau, Ph.D thesis, University Utrecht (2003).

[12] G. Bryant, *Phys. Rev. B* **37**, 8763 (1988).

[13] Y. Kayanuma, *Phys. Rev. B* **38**, 9797 (1988).

[14] L.E. Brus, *J. Phys. Chem.* **79**, 5566 (1983).

[15] P. Lippens and M. Lannoo, *Appl. Phys. Lett.* **61**, 1948 (1992).

[16] M.V. Rama Krishna and R.A. Friesner, *Phys. Rev. Lett.* **67**, 629 (1991).

[17] L. Wang and A. Zunger, *J. Chem. Phys.* **62**, 2158 (1994).

[18] E. Merzbacher, *Quantum Mechanics*, John Wiley (1994).

[19] S. Fonash, *Solar Cell Device Physics* Academic Press, (1981).

[20] A. Franceschetti and A. Zunger, *Phys. Rev. B* **62**, R16287 (2000).

[21] A. Zunger, *Phys. Stat. Sol. B* **224**, 727 (2001).

[22] A. Franceschetti, A. Williamson and A. Zunger, *J. Phys. Chem.* **104**, 3398 (2000).

[23] Y. Niquet, Ph.D thesis, Universite des Siences et Technologies de Lille (2001).

[24] J. Elliot and P. Dawber, *Symmetry in Physics*, MacMillan Ltd (1985).

[25] Technical specifications of Bio-rad FTIR-spectrometer FTS 40.

[26] R.J. Warburton, C. Schaflein, D. Haft, F. Bickel, A. Lorke, K. Karrai, J.M. Garcia, J. Schoenfeld and P.M. Petroff, *Nature* **405**, 926 (2000).

[27] D. Averin, A. Korotkov and K. Likharev, *Phys. Rev. B* **44**, 6199 (1991).

[28] N. Hill and K. Whaley, *J. Chem. Phys.* **100**, 2831 (1994).

[29] M. Dib, M. Chamarro, V. Voliotis, J.L. Fave, C. Guenaud, P. Roussignol, T. Gacoin, J.P. Boilot, C. Delerue, G. Allan and M. Lannoo, *Phys. Stat. Sol. b* **212**, 293 (1999).

[30] P. Hoyer, R. Eichberger and H. Weller, *Ber. Bunsen-Ges. Phys. Chem.* **97**, 630 (1993).

[31] E.A. Meulenkamp, *J. Phys. Chem. B* **102**, 5566 (1998).

[32] D. Norris, Al.L. Efros, M. Rosen and M.G. Bawendi, *Phys. Rev. B* **53**, 16347 (1996).

[33] S. Empedocles, D. Norris and M.G. Bawendi, *Phys. Rev. Lett.* **77**, 3873 (1996).

[34] R.G. Neuhauser, K.T. Shimizu, W.K. Woo, S. Empedocles and M.G. Bawendi, *Phys. Rev. Lett.* **85**, 3301 (2000).

[35] D. Norris and M.G. Bawendi, *Phys. Rev. B* **53**, 16338 (1996).

Chapter 5

Luminescence of ZnO quantum-dot assemblies

Assemblies of ZnO nanocrystals can be charged with electrons; the average electron number can be varied in a controlled way between zero and ten. The luminescence of such charged assemblies due to UV excitation has been studied and compared with the luminescence of quantum-dot suspensions. The luminescence of ZnO assemblies depends on the electron number and the nature of the interpenetrating electrolyte. Remarkably, with increasing electron number, the green (defect) luminescence quenches, while the exciton luminescence increases. Thus, quenching of the exciton luminescence by an Auger-type process is unimportant in charged ZnO quantum dots. This forms a strong contrast with results obtained with Si and CdSe quantum dots.

5.1 Introduction

ZnO has been known as a luminescent material for a century, and some fifty years ago it was discovered that firing ZnO powder in a reducing atmosphere gives a particularly efficient blue-green phosphor. Green light has an energy smaller than the band gap of ZnO and corresponds to an electronic transition via a defect. Green-emitting ZnO is usually denoted as ZnO:Zn because of the loss of oxygen during the reducing treatment [1]. This material has a high efficiency as a low-voltage phosphor and has been used in vacuum fluorescent displays (VFD's) and field emission displays (FED's) [2]. Because of the important applications luminescent ZnO has been the subject of much research aimed at finding the origin of the visible emission.

Recent work has indicated that oxygen vacancies are the most likely candidates for the recombination centers involved in the visible luminescence of ZnO [3–8]. In the past, most work has been done on micron-sized single-crystalline materials. Van Dijken et al. investigated ZnO nanocrystals and deduced from the size-dependent visible emission that a hole in a deep trap and an electron in the conduction band must be responsible for the visible emission [4]. The deep hole trap was assigned to oxygen vacancies in ZnO.

Besides the visible luminescence an ultraviolet emission is also found in many cases; this is due to the radiative recombination of excitons. This emission is relatively narrow and located at around 3.25 eV for a bulk ZnO crystal. Both the visible and the exciton emission was observed in ZnO quantum-dot assemblies. It was found that the intensity of the visible and the exciton emission depended on the electrochemical potential of the system [9, 10].

In this chapter, we compare the luminescence of assemblies of ZnO quantum dots with that of suspensions. We make use of the fact that, in our experiments, the average electron number $\langle n \rangle$ is known with a reasonable accuracy. In particular, we investigate the effect of an increasing occupation of the conduction orbitals on the defect and exciton luminescence.

5.2 Experimental

The suspensions and assemblies of ZnO nanocrystals were prepared by the method described in Chapter 2. The electrodes used in this work were made with fluoride-doped tin oxide (TFO) on glass substrates. The average number of electrons per quantum dot $\langle n \rangle$ was determined as described in Section 2.5. The results de-

scribed in this chapter were obtained with ZnO assemblies made from 4.3 nm quantum dots, unless otherwise mentioned.

The *photoluminescence measurements* were performed on a SPEX Fluorolog spectofluorometer model F2002 equipped with a double-grating 0.22 m SPEX 1680 monochromators and a 450 W xenon lamp as the excitation source. UV irradiation of the suspensions and the assemblies was carried out inside the spectrofluorometer using the excitation beam (at 300 nm). The emission light was transported through a fibre optics cable to a 0.3 m monochromator (Acton Pro SP-300i, 150 lines/mm grating, blazed at 500 nm).

The *suspensions* in ethanol were measured in a quartz cuvette. The excitation beam had a rectangular cross section of about 1 cm by 1 mm. The penetration depth of the UV radiation was such that absorption took place over the entire width of the cuvette.

The ZnO *assemblies* were investigated in an electrochemical cell with quartz windows. The aqueous electrolyte was an argon-purged 0.2 M phosphate buffer (pH = 8) and was made by adding pure NaOH to a phosphoric acid solution. Here the reference electrode was a Ag/AgCl electrode, and the counter electrode a platinum sheet. Otherwise, anhydrous propylene carbonate (PC) with 0.1 M tetrabutylammonium perchlorate ($TBAClO_4$) was used. In this electrolyte a silver rod served as a quasi-reference electrode (see also Chapter 3).

5.3 Luminescence of ZnO quantum dots

In Figure 5.1 typical emission and absorption spectra of a ZnO suspension are shown, taken after the sol was purged with nitrogen for 10 minutes. A broad band emission is observed in the visible region extending from 1.5 eV to 3.0 eV with a maximum at 2.2 eV. This is called the *visible emission* of ZnO. A much sharper peak is observed in the UV region with a maximum at 3.4 eV and extending from 3.0 to 3.5 eV. This is called the *exciton emission* of ZnO.

The exciton and visible emission of ZnO are found to be size dependent and from this size dependence the mechanism for the luminescence was derived by Van Dijken et al. [3, 4]. The mechanism for the exciton and visible emission of ZnO is taken from these references and briefly summarized.

Figure 5.2 gives a schematic overview of the *radiative* relaxation processes that take place upon photoexcitation of a ZnO dot. The *non-radiative* recombination processes which occur after photoexcitation of a ZnO quantum dot are omitted from this scheme. The band edges are shown as well as a deep trap level

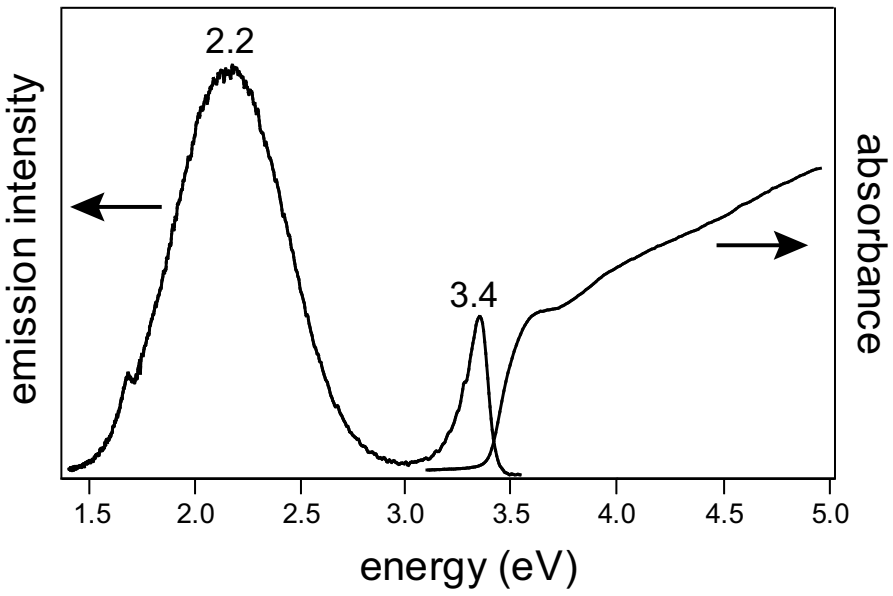

Figure 5.1: Room-temperature emission and absorption spectra of a suspension of nanocrystalline ZnO quantum dots in ethanol. The emission spectrum was obtained with 4.1 eV excitation after the ZnO suspension was purged with nitrogen for 10 minutes. A broad band is observed in the visible region with a maximum at 2.2 eV. A much sharper peak is observed in the UV region with a maximum at 3.4 eV. The onset of absorption is at about 3.4 eV.

in the bulk of the dot, $V_O^{\bullet}$. At the surface of the dot, the energy distribution of an O^{2-}/O^{-} state is shown. The arrows indicate the electronic transitions. If a ZnO quantum dot is excited with a photon with an energy larger than the band gap, an exciton is created. This exciton can decay to the quantum-dot ground-state by emission of a UV-photon (A). The hole can be trapped in a surface state O_S^{2-} which is oxidized to O_S^{-} (B). The trapped hole is transferred to the oxygen vacancy $V_O^{\bullet}$ which is oxidized to $V_O^{\bullet\bullet}$ (C). The electron in the conduction band recombines with the trapped hole to give the visible emission (D).

Electron paramagnetic resonance (EPR) studies have shown that oxygen vacancies containing one electron ($V_O^{\bullet}$) are the predominant paramagnetic defects [5–7]. In macrocrystalline ZnO these defects are represented by a level approximately 2 eV below the conduction band edge [11] and they are often assumed to be the recombination centers for the visible emission in ZnO. The $V_O^{\bullet}$ center can only serve as the recombination center for the visible emission after formation of a $V_O^{\bullet\bullet}$

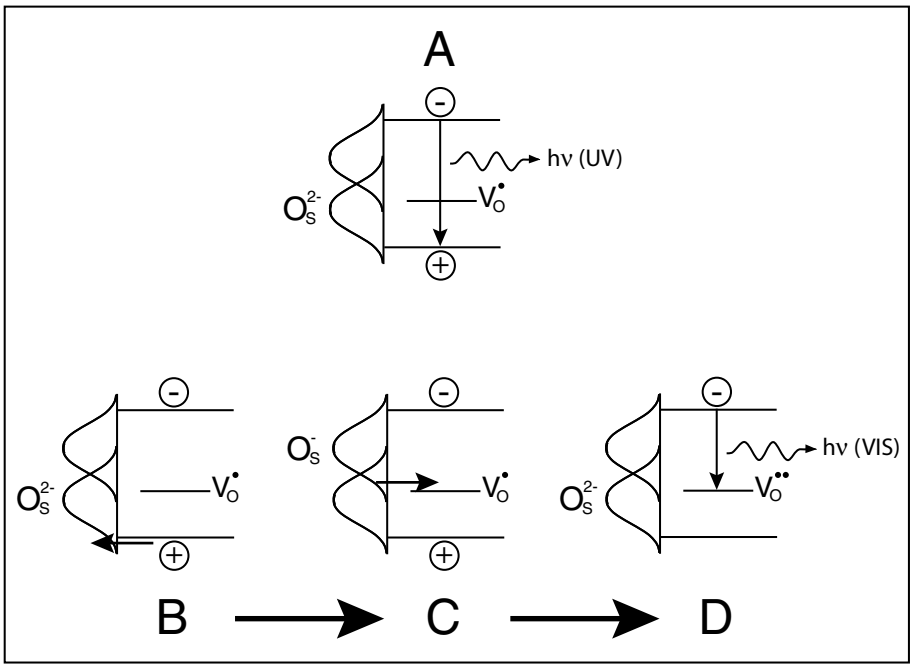

Figure 5.2: A schematic overview of the radiative relaxation processes that take place upon photoexcitation of a ZnO dot [4]. The band edges are shown as well as a deep trap level in the bulk of the particle. At the surface of the dot, an energy distribution of an O^{2-}/O^{-} state is shown. A The exciton relaxes to its ground-state emitting a UV-photon. This is the exciton emission. B The hole gets trapped in a surface state O_S^{2-} which is oxidized to O_S^{-}. C The trapped hole is transferred to the oxygen vacancy $V_O^{\bullet}$ which is oxidized to $V_O^{\bullet\bullet}$. D The electron in the conduction band recombines with the trapped hole which gives rise to the visible emission.

center as was shown by Van Dijken et al. [4] (Figure 5.2).

Figure 5.3 shows the effect of purging the suspension with nitrogen and irradiation with UV light. Spectra were taken at different times after purging with nitrogen had started. Upon UV irradiation the visible emission quenches while the intensity of the exciton emission increases. The width of the exciton emission increases slightly (from 100 to 150 meV) and the peak maximum shifts to somewhat lower energies (3.36 to 3.34 eV) as the intensity increases, on the other hand, the width of the visible emission peak is constant (approximately 600 meV) and the peak maximum does not shift significantly.

The photochemical charging of the ZnO quantum dots with electrons was found to be responsible for the increased exciton emission [8]. Van Dijken showed

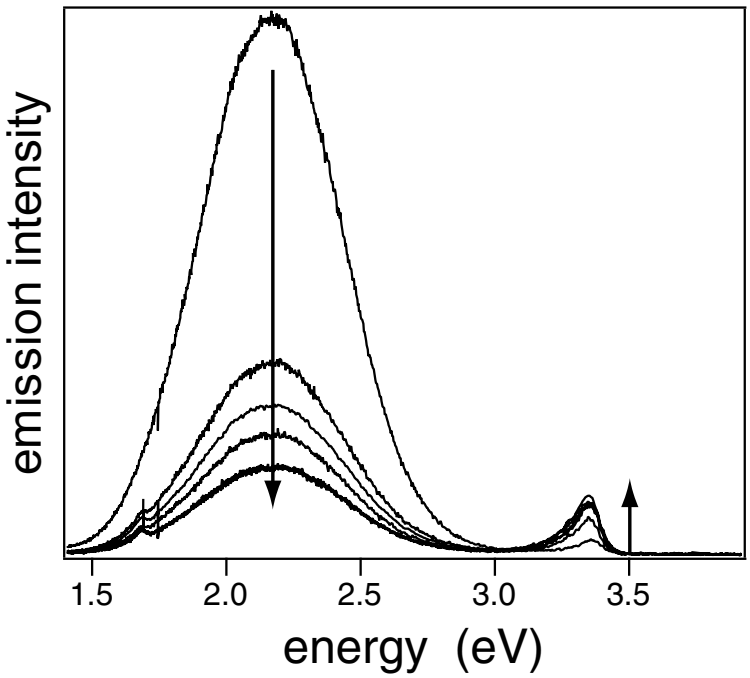

Figure 5.3: Room-temperature emission spectra of the same quantum-dot suspension as in Figure 5.1. The emission spectra were obtained with 4.1 eV excitation. The spectra are taken after regular time intervals while the sol is purged with nitrogen. The visible emission quenches and the exciton emission increases in time as the sol is purged with nitrogen.

that admission of oxygen into the colloidal suspension restored the initial emission properties. The quenching of the visible emission was accounted for by assuming that oxygen scavenges photogenerated electrons. In the absence of oxygen, excess photogenerated electrons are present resulting in a passivation of $V_O^{\bullet}/V_O^{\bullet\bullet}$ centers, which are involved in the visible emission process [3, 4, 8] (see Figure 5.2). A $V_O^{\bullet\bullet}$ center changes into a $V_O^{\bullet}$ center by accepting an electron. The $V_O^{\bullet}$ center can trap an additional electron to form a $V_O^{\times}$ center which is located just below the conduction band edge [3, 4, 11]. Thus, in the presence of conduction electrons, the defect center for the green emission is removed. By performing measurements on an assembly, we hoped to obtain more detailed information on the role of conduction electrons in the defect and exciton luminescence.

5.4 Potential-dependent luminescence

5.4.1 Phosphate buffer

In Figure 5.4 room-temperature emission spectra are shown of a ZnO assembly permeated with a deaerated phosphate buffer. The numbers in the figures refer to the potential in V vs. Ag/AgCl. The total potential range is divided into four domains to emphasize the changes in the visible and exciton emission. The visible emission increases by a factor of about three when the potential is decreased from 0 to -0.5 V (A). The exciton emission is very weak and nearly constant in this potential domain. Changing the potential to more negative values leads to a strong decrease of the visible emission, while the exciton emission is increased (B). In the third domain (C), the visible emission has almost vanished. The exciton emission increases further with decreasing potential. The width of the exciton emission peak increases from about 0.1 to 0.3 eV in this domain. The width of the visible emission peak is broad (0.6 eV) and does not change much from 0 to -1 V. In the fourth domain from -1 to -1.2 V, the visible emission is completely quenched. The exciton emission decreases slightly at more negative potentials.

From the results presented in Figure 5.3 and 5.4 for the ZnO assembly and the ZnO suspension respectively, it is obvious that decreasing the potential (from -0.50 to -0.75 V) has the same effect on the luminescence as purging the UV-irradiated suspension with nitrogen.

The same potential-dependent luminescence characteristics were obtained by changing the potential back to more positive values. This shows that the assemblies are chemically stable in this potential range. Changing the potential to values more negative than -1.2 V leads, however, to irreversible damage of the ZnO layer; the assemblies of ZnO nanocrystals become turbid and less charge can be stored. The ZnO dots and the underlying TFO are known to be reduced in this potential range [12].

In Figure 5.5 the results from Figure 5.4 are summarized. The maximum intensity of both the visible and the exciton emission peaks are plotted versus the electrochemical potential. It can be clearly seen that the visible emission increases from an almost constant value to a maximum at -0.5 V about three times as high. At more negative values the visible emission is quenched. From Chapter 2 we know that -0.6 V is the onset potential for electron injection into the atom-like conduction levels of the ZnO quantum dots. At this potential the exciton emission starts to increase strongly and the visible emission is quenched.

With the results obtained from the charging experiments in Chapter 2 we can

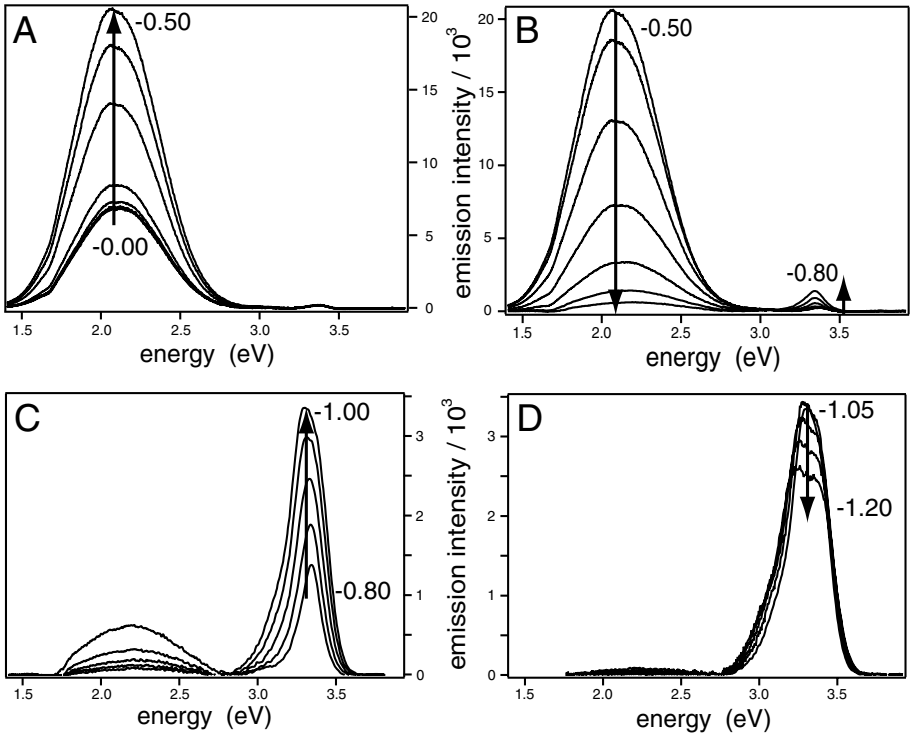

Figure 5.4: Room-temperature emission spectra of a ZnO assembly permeated with a phosphate buffer. The numbers in the figures refer to the potential in V vs. Ag/AgCl. The potential is changed in 50 mV steps. The total potential range is divided into four characteristic regions: A From 0 to -0.5 V; the visible emission peak increases and the exciton emission is small and does not change. B From -0.5 V to -0.75 V; the visible emission quenches gradually (by a factor of 20 at -0.75 V) and the exciton emission starts to increase at almost the same potential (from -0.6 V). C From -0.75 V to -1.0 V; The visible emission is quenched almost completely and the exciton emission increases further and becomes the most intense emission. D From -1.0 V to -1.2 V; the visible emission is quenched and the exciton emission decreases slightly.

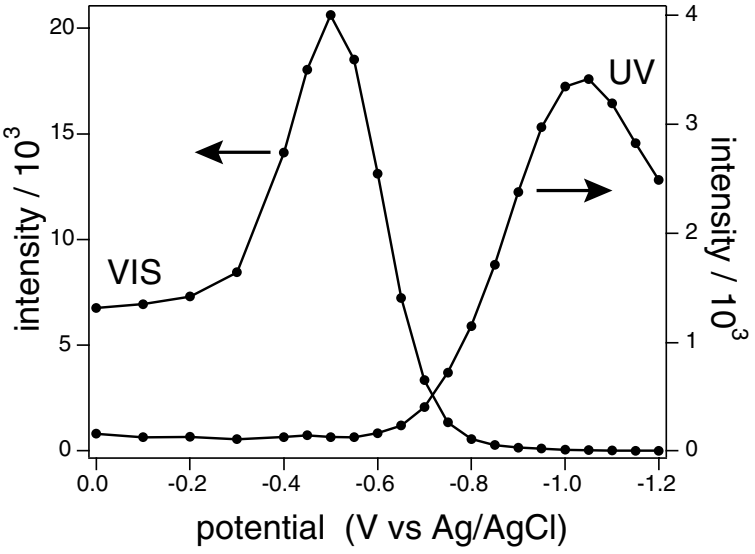

Figure 5.5: Peak intensity of the visible and exciton emission as a function of the potential. The visible emission increases between 0 and -0.5 V from an almost constant value to a value 3 times higher and is quenched at more negative potentials. At -0.8 V the intensity has decreased to only 2% of the maximum value. The exciton emission has an almost constant value for the potential range from 0 to -0.55 V. At -0.6 V the exciton emission increases but is quenched at potentials higher than -1.05 V.

plot the maximum intensities of Figure 5.5 against the average number of electrons per quantum dot $\langle n \rangle$ (see Figure 5.6). It is clear that the visible emission is quenched as soon as electrons are injected into the conduction levels of the ZnO dots. The intensity has decreased by a factor of eight for $\langle n \rangle$ = 1 and the visible emission has almost vanished for $\langle n \rangle$ = 2. These results strongly suggest that on average there is at most one green luminescent defect center per quantum dot. The exciton emission increases almost linearly with $\langle n \rangle$ to a value of an average of six electrons per quantum dot. This shows that Auger recombination is not important in ZnO. In contrast, Auger recombination was found to be a dominant process in other quantum-dot systems, such as porous Si [13–15] and CdSe [16, 17]. In the case of Auger recombination an exciton can recombine non-radiatively by transferring its energy to an electron in a conduction level (or another exciton). The Auger-excited electron will relax by non-radiative processes. This leads to a decreasing luminescence with an increasing concentration of electrons in the conduction levels. It is not clear why Auger recombination is unimportant in ZnO and

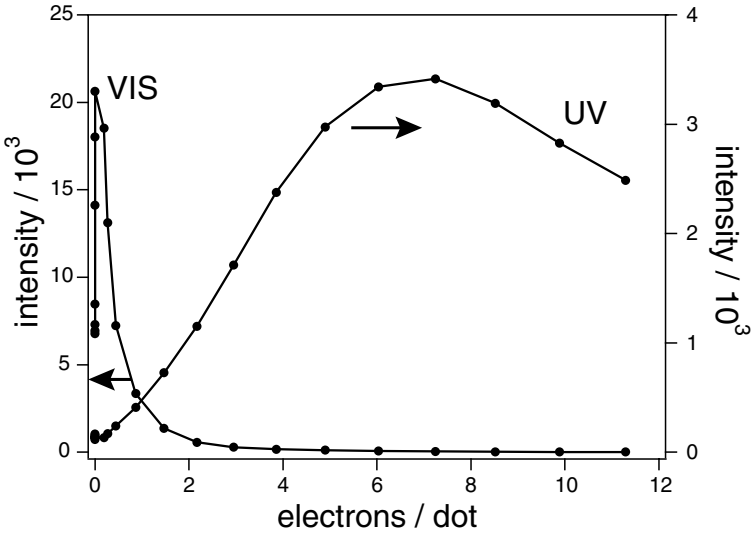

Figure 5.6: Emission peak intensities of the visible and exciton emission as a function of the average electron occupation number $\langle n \rangle$. The visible emission intensity is completely quenched at $\langle n \rangle$ = 2. The exciton emission increases almost linearly up to an average of six electrons per dot.

why the luminescence intensity increases with $\langle n \rangle$. A possible explanation could be that the probability for radiative recombination is proportional to the number of electrons in the conduction levels. Further (theoretical) work is needed to answer these important questions.

In Chapter 2 and 3 we can find that at -0.8 V only about half the quantum dots have N = 1; at -0.8 V the maximum of the *S*-type energy level distribution is reached. This would suggest that the largest dots in the assembly are predominantly responsible for the visible emission. That could also be an explanation for the small shift in the energy of the visible and exciton peak maxima in Figure 5.7 are plotted versus the potential. The visible peak maximum shifts from around 2.12 to 2.10 eV in the same potential range in which the visible emission increases to its maximum value at -0.5 V. At more negative potentials the peak shifts to higher energy (approximately 2.3 eV at -1.15 V). In the potential range from 0 to -1 V we find an increase in the peak maximum energy of approximately 180 meV. For comparison, Hoyer et al. observed a much stronger increase of the energy of approximately 400 meV [9]. The shape of their visible emission peak also changed strongly in this potential range. They observed asymmetrical and ir-

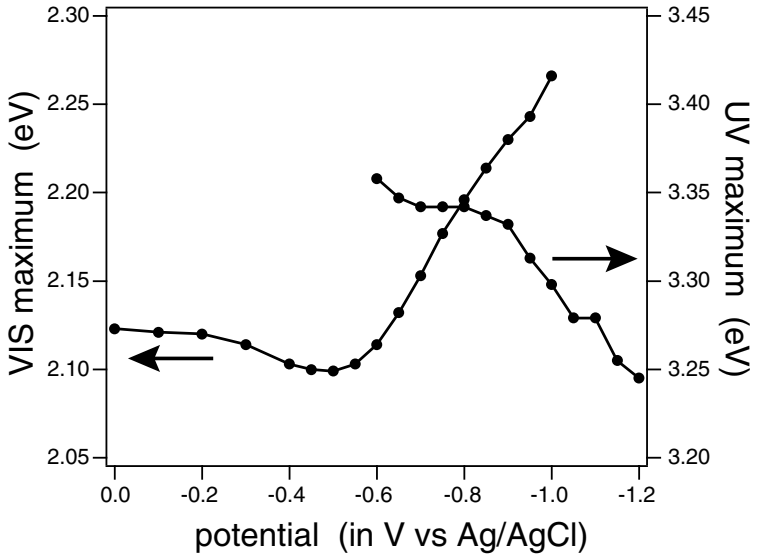

Figure 5.7: Visible and exciton emission peak maximum energies. The visible peak maximum energy decreases from approximately 2.12 to 2.10 eV if the potential is changed from 0 to -0.5 V. If the potential is further decreased, the energy shifts to a maximum value of approximately 2.25 eV at -1.0 V. The exciton emission peak maximum energy shifts to lower energies from approximately 3.35 to 3.25 eV in the potential range of -0.6 to -1.2 V. Because of the irregular shape of the exciton emission peak at potentials more negative than -1 V we took the maximum energy of the best Gaussian fit.

regularly shaped emission peaks in the complete potential range (0 to -1 V) while we observed almost perfect Gaussian-shaped visible emission peaks. The exciton emission peak maximum shifts from about 3.35 to 3.25 eV in the potential range of -0.6 to -1.2 V. A similar shift of the exciton emission to lower energies due to the injection of electrons was observed by Warburton [18]. Because of the irregular shape of the exciton emission peak at potentials more negative than -1 V we took the maximum energy of the best Gaussian fit.

The increasing intensity of the visible emission and the decreasing energy of this emission in the potential range of 0 to -0.5 V are not understood. The decrease in the visible emission, starting negative of -0.5 V is due to the loss of $V_O^{\bullet}/V_O^{\bullet\bullet}$ centers caused by the occupation of these centers by electrons. The energy shifts to somewhat higher values because the largest dots are filled with electrons first, before the smaller ones. The upward shift by 180 meV is in line with the dispersion of the conduction energy levels deduced from independent optical and

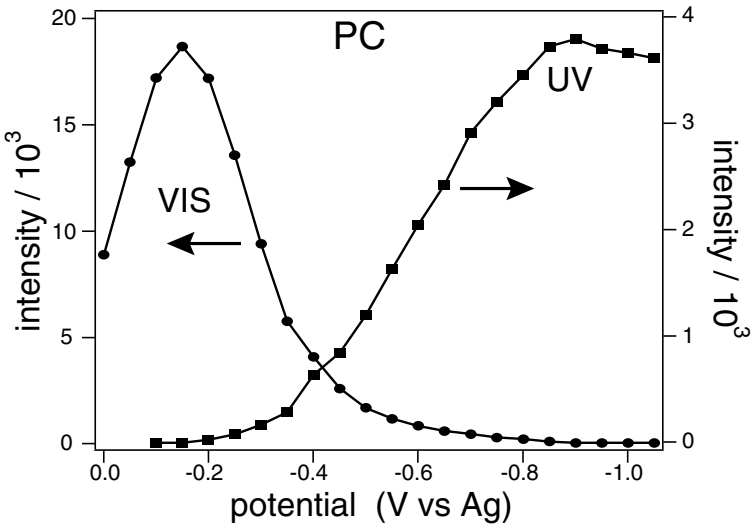

Figure 5.8: Peak intensities of the visible and exciton emission as a function of the potential. The results are shown for a ZnO quantum-dot assembly permeated with PC. The visible emission increases by a factor 2 from 0 to -0.2 V and is quenched on going to more negative potentials. At -0.6 V the maximum intensity has decreased to only 5% of the maximum value. The exciton emission increases strongly at potentials more negative than -0.2 V but is quenched at potentials more negative than -0.9 V.

electrical experiments, presented in Chapters 3 and 4. The preferential filling of the lowest atom-like orbitals shows that a state close to Fermi-equilibrium is reached in the quantum-dot assembly.

5.4.2 Propylene carbonate electrolyte

Here, we consider the role of conduction electrons on the defect and exciton luminescence for assemblies in an aprotic solvent (PC). In this case, fewer electrons can be stored per dot than in an assembly permeated with the phosphate buffer (see Chapter 3).

In Figure 5.8 the maximum peak intensities for the visible and exciton emission are shown as a function of the electrochemical potential of a ZnO quantum-dot assembly permeated with PC. The maximum intensities do not significantly differ from the values found with the phosphate buffer. We observe a similar potential dependence for the increase and quenching of the two emission peaks. The visible emission increases by a factor of 2 from 0 to -0.2 V and is quenched at

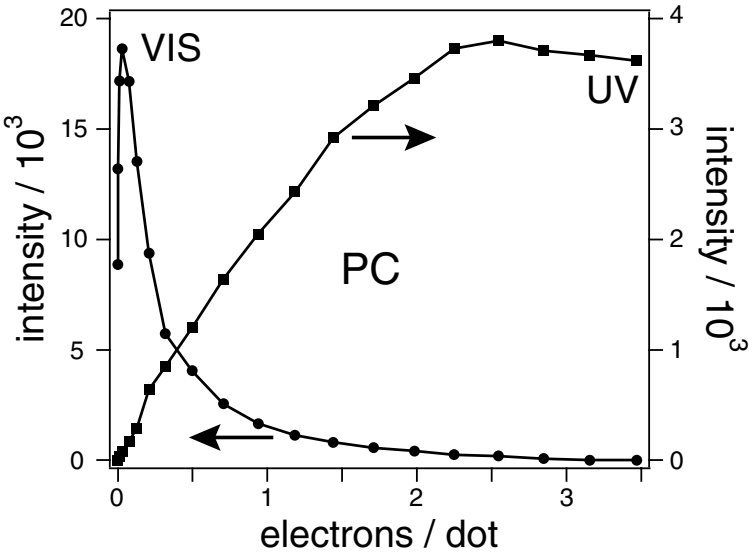

Figure 5.9: Emission peak intensity of the visible and exciton emission as a function of the average electron occupation number $\langle n \rangle$. The visible emission intensity is almost completely quenched at $\langle n \rangle$ = 2. The exciton emission increases almost linearly up to $\langle n \rangle$ = 2.

more negative potentials. At -0.6 V the intensity has decreased to only 5% of the maximum value. The exciton emission increases strongly from -0.2 V to -0.9 V. Negative of -0.9 V, there is a slight decrease in intensity. This decrease is probably due to chemical degradation of the ZnO surface.

In Figure 5.9 the results from Figure 5.8 are replotted as intensity versus $\langle n \rangle$. The visible emission goes down as soon as electrons are injected into the ZnO assembly and this emission is almost completely quenched at $\langle n \rangle$ = 2. The exciton emission increases as electrons are injected into the assembly. The increase is almost linear up to $\langle n \rangle$ = 2. If we take $\langle n \rangle$ = 1 as a reference we can compare the results in PC and water. The intensity of the visible emission has decreased to 7 and 13% of its maximum value for PC and the phosphate buffer, respectively. Thus, it seems that less electrons per quantum dot are needed in PC than in the phosphate buffer to get the same degree of quenching. A possible explanation is that the visible emission originates mainly from the larger quantum dots in the assembly. The Coulomb repulsion in the PC electrolyte causes the electrons to occupy mainly the larger quantum dots, in contrast to the situation without Coulomb repulsion (see Section 3.3.1). This is due to the increase of the electrochemical

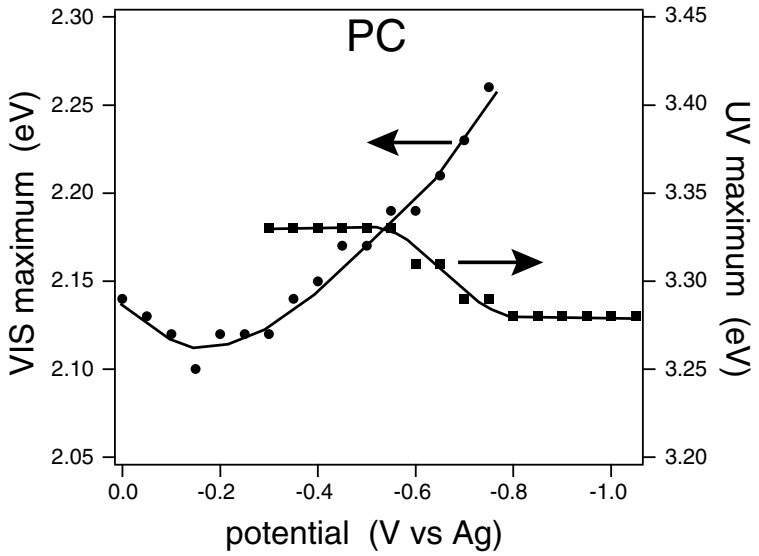

Figure 5.10: Visible and exciton emission peak energies. The visible peak energy decreases from approximately 2.15 to 2.10 eV if the potential is changed from 0 to -0.15 V. If the potential is further decreased, the energy shifts gradually to a maximum value of approximately 2.25 eV at -1.15 V. The exciton emission peak maximum energy shifts to lower energies from about 3.33 to 3.28 eV in the potential range of -0.30 to -1.05 V. Because of the irregular shape of the exciton emission peak at potentials more negative than -0.9 V we took the peak energy of the best Gaussian fit.

potential for electron injection caused by the Coulomb repulsion.

In Figure 5.10 the energy maxima of the visible and exciton emission are shown as a function of the potential. The visible peak maximum decreases from approximately 2.15 to 2.10 eV as the potential is changed from 0 to -0.15 V. As the potential is further decreased, the peak energy increases gradually to a maximum value of approximately 2.25 eV at -1.15 V. The maximum energy of the exciton emission peak shifts to lower energies from about 3.33 to 3.28 eV in the potential range of -0.30 to -1.05 V. Because of the irregular shape of the exciton emission at potentials more negative than -0.9 V we took the maximum energy of the best Gaussian fit. These results for PC are similar to the results obtained with the phosphate buffer in the same potential range as can be seen from Figure 5.7 and 5.10.

5.5 Conclusions

ZnO quantum dots show in general two types of emission: a broad-band emission in the visible range and a relatively narrow ultraviolet emission (the exciton emission). A change from predominantly visible to completely ultraviolet emission is observed on purging a ZnO suspension with nitrogen or inserting electrons electrochemically into ZnO assemblies. We found a strong decrease in the visible emission and a strong increase in the exciton emission with decreasing potential. The interpenetrating electrolyte had a clear effect on the emission characteristics. With PC much fewer electrons were needed to produce the same exciton emission intensity. The stability of the ZnO in the specific electrolyte solution seemed to be the limiting factor in the increase of the exciton emission.

References

[1] R.E. Shrader and H.W. Leverenz, *J. Opt. Soc. Am.* **37**, 939 (1947).

[2] S. Shionoya and W.M. Yen (editors), *Phosphor Handbook*, CRC Press LCC, Boca Raton, 255 (1999).

[3] A. van Dijken, Ph.D thesis, University Utrecht (1999).

[4] A. van Dijken, E.A. Meulenkamp, D. Vanmaekelbergh and A. Meijerink, *J. Phys. Chem. B* **104**, 1715 (2000).

[5] M. Anpo and Y. Kubokawa, *J. Phys. Chem.* **88**, 5556 (1984).

[6] K. Vanheusden, C.H. Seager, W.L. Warren, D.R. Tallant and J.A. Voigt, *Appl. Phys. Lett.* **68**, 403 (1996).

[7] K. Vanheusden, W.L. Warren, C.H. Seager, D.R. Tallant, J.A. Voigt and B.E. Gnade, *Appl. Phys. Lett.* **79**, 7983 (1996).

[8] A. van Dijken, E.A. Meulenkamp, D. Vanmaekelbergh and A. Meijerink, *J. Phys. Chem. B* **104**, 4355 (2000).

[9] P. Hoyer R. Eichberger and H. Weller, *Ber. Bunsen-Ges. Phys. Chem.* **97**, 630 (1993).

[10] P. Hoyer and H. Weller, *J. Phys. Chem.* **99**, 14096 (1995).

[11] F.A. Kröger, *The Chemistry of Imperfect Crystals*, North-Holland Publishing company, Amsterdam, 691 (1964).

[12] E.A. Meulenkamp, *J. Phys. Chem. B* **103**, 7831 (1999).

[13] F. Ozanam, J.-N. Chazalviel and R.B. Wehrspohn, *Thin Solid Films* **297**, 53 (1997).

[14] L.M. Peter and R.I. Wielgosz, *Appl. Phys. Lett.* **69**, 806 (1996).

[15] L.M. Peter, R.I. Wielgosz, P.A. Snow, R.V. Penty, I.H. White and E.A. Meulenkamp, *Thin Solid Films* **276**, 123 (1996).

[16] K.T. Shimizu, W.K. Woo, B.R Fisher, H.J. Eisler and M.G. Bawendi, *Phys. Rev. Lett.* **89**, 117401 (2002).

[17] A.A. Mikhailovsky, A.V. Malko, J.A Hollingsworth, M.G. Bawendi and V.I. Klimov, *Appl. Phys. Lett.* **80**, 2380 (2002).

[18] R.J. Warburton, C. Schäflein, D. Haft, F. Bickel, A. Lorke, K. Karral, J.M. Garcia, W. Schoenfeld and P.M. Petroff, *Nature* **405**, 926 (2000).

Chapter 6

Non-dispersive, trap-limited electron transport in macroporous GaP

Electron transport in macroporous GaP networks permeated with an electrolyte solution has been studied by analysis of the photocurrent response upon a small-amplitude modulation of the light intensity. It is found that under conditions close to a steady-state, electron transport is non-dispersive, characterized by a single transit time that depends on the thickness of the porous layer and the background light intensity. An analysis of the results show that the transit time is determined by multiple trapping and detrapping of electrons in interfacial states close to the electron Fermi level which is determined by the steady-state light intensity. As a result the density-of-states (DOS) function in a considerable region of the band gap can be determined from the transit time, when the energy of the electron Fermi level is changed by means of the background light-intensity.

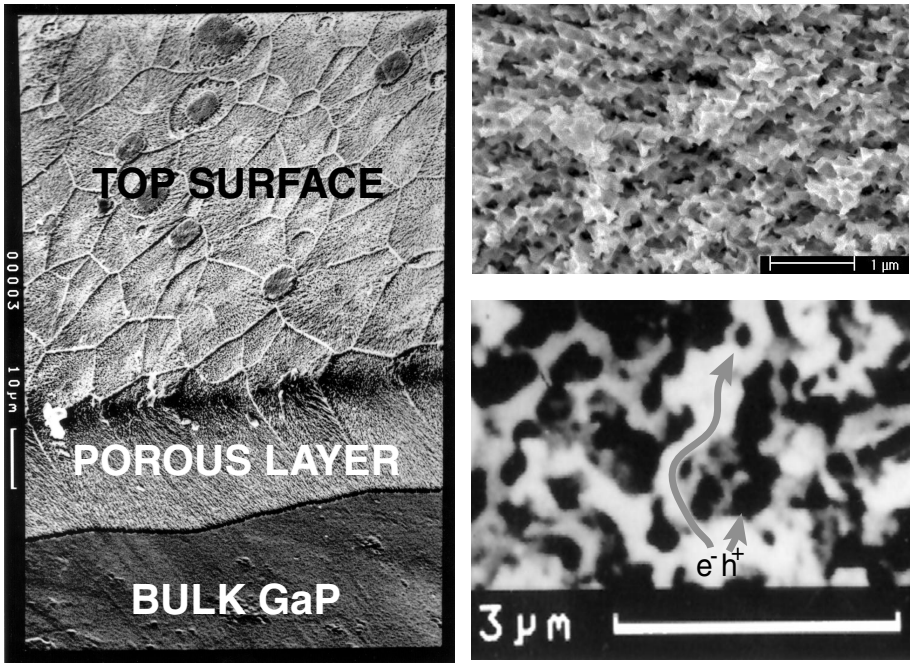

Figure 6.1: Left SEM picture: top and side view of a porous *n*-type GaP layer (20 μm thick) formed on a crystalline GaP substrate by anodic etching at 10 V in aqueous 0.5 M H_2SO_4. The two SEM pictures at the right give a more detailed image of the porous network. The lower picture at the right shows a thin slice of the porous layer where a photo-generated hole is transferred to the permeated electrolyte solution and the electron diffuses through the network towards the back contact. The *n*-GaP structural units (white) are interconnected. The size of the structural units shows a large variation in the 30-300 nm range.

6.1 Introduction

Porous semiconductors, permeated with an electrolyte solution or an electronic conductor, form the basis for efficient devices for converting light into electrical energy [1–4]. In such a system, the dynamics of electron-hole separation are directly related to the micro- or nanoscale geometry. Due to separation of the photo-excited electron and hole in the two phases, recombination is slow. As a consequence, photogenerated charge carriers can travel over macroscopic distances through a porous semiconductor and can be collected at a back contact.

The system considered in this work is macroporous *n*-type GaP. Figure 6.1 shows an overview SEM picture of a layer of porous GaP on bulk GaP; the porous

layer is formed by anodic etching [5]. The porous layer has a uniform thickness which can be varied between 10 and 200 μm by the charge passed during anodic etching. XRD measurements showed that the porous layer is single crystalline [6]. Figure 6.1 also shows the network in more detail; the dimensions of the pores and structural units are in the 100 nm range. Absorption of light of sufficient energy ($h\nu > 2.24$ eV) leads to free electrons and holes in the porous solid; the photoexcited holes can reach the (internal) interface with the electrolyte solution, where they are consumed in an anodic charge transfer process. Electron-hole recombination is prevented due to the fact that the diffusion length of the photogenerated holes is comparable to the dimensions of the structural units of the GaP network [5]. Under anodic conditions, each photon absorbed in the porous GaP leads to the passage of one electron in the external circuit. Photogenerated electrons travel over macroscopic distances through the porous network before they are collected at the back contact. This makes such a system interesting for the study of long-range electron transport.

Since porous GaP is permeated with a highly conductive electrolyte, the internal surface has a constant electrostatic potential; there is, hence, no electrical field involved in the long-range transport of the electrons; transport is due solely to diffusion. An electronic scheme of the porous GaP system is presented in Figure 6.2. The statistical driving force that is responsible for the directed electron diffusion in such a system, i.e. the spatial gradient of the electron Fermi level, has been considered in previous work [7]; it is determined by the photogeneration of electrons at one side of the network, transport in the network, and collection at the back contact. It has been found that the driving force is nearly constant in the entire porous structure of thickness d, and is approximately equal to $2k_BT/d$ [7].

Electron transport in porous semiconductors (mainly particulate systems such as nanoporous TiO_2) has been investigated by measuring the harmonic photocurrent density response $\tilde{j}(\omega)$ upon a small-amplitude modulation of the absorbed light intensity $\tilde{\Phi}(\omega)$ (ω is the modulation frequency), that is superimposed on the steady-state light intensity Φ [8–13]. It has been shown that for systems with a high photocurrent quantum yield, the transfer function, i.e. $\tilde{j}(\omega)/e\tilde{\Phi}(\omega)$, is a fingerprint of the transport characteristics. The transfer function has a characteristic frequency that is unequivocally related to the average transit time of the electrons through the porous solid [14]. From this work, it became clear that electron diffusion in particulate nanoporous TiO_2 assemblies is strongly attenuated due to trapping/detrapping of electrons in band gap states. The origin for the attenuation of electron diffusion is hence similar to that in amorphous semiconductors, such as intrinsic amorphous hydrogenated silicon [15]. However, it is believed that in

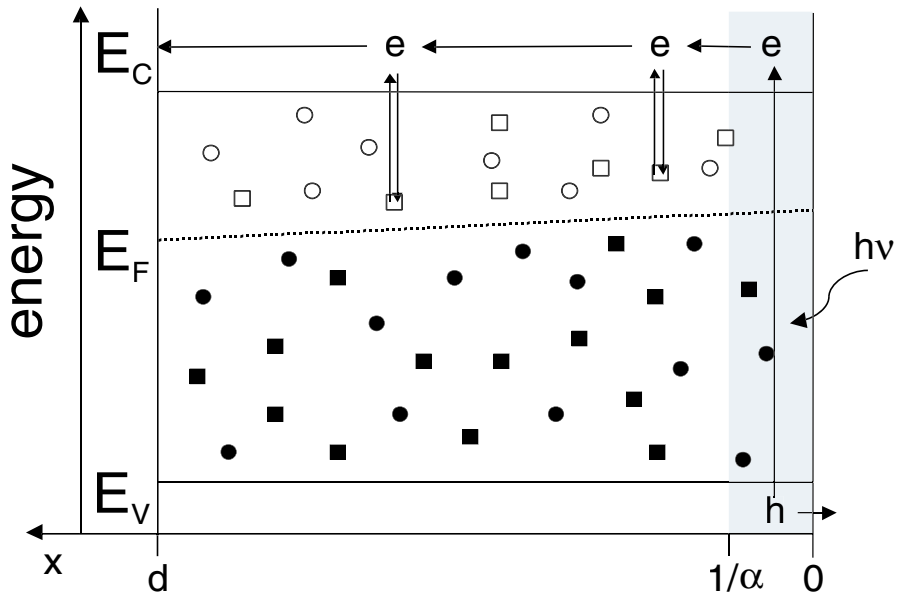

Figure 6.2: Energy scheme of trap-limited electron transport in macroporous GaP. Electrons and holes are generated by green light (514.4 nm line of an argon laser) in a small region at the electrolyte side of the layer, $0 < x < 1/\alpha$ with $1/\alpha < 3$ μm. Holes are directly transferred to the electrolyte at $x = 0$; the electrons have to travel through the porous layer over a distance d, until they reach the crystalline, bulk part of the GaP and are transferred to the back contact at $x = d$. The electrons diffuse through the porous layer due to a gradient in the electron Fermi level E_F. During their passage, the electrons are trapped in unoccupied states (□,❍) near E_F; the transit time is determined by multiple trapping in states around E_F.

porous semiconductors, the trap levels in the band gap are located at the internal interface between the solid and the electrolyte.

In a theoretical paper [14], the case of a small excess of free electrons (in the conduction band) was considered diffusing through the system and undergoing trapping/detrapping via electron levels in the band gap. The steady-state occupation of these levels is determined by the transport and trapping/detrapping of the photogenerated electrons. The results of this theoretical exercise were remarkable in the sense that a transport regime was predicted which is non-dispersive (also called 'normal' or 'Gaussian') [16–20]. Although the travelling electrons are frequently trapped/detrapped during their passage, transport is characterized by a mean 'transit' time determined by the length of the transport path, the den-

sity of trapping levels close to the electron Fermi level E_F (in the energy-range $E_F - k_BT < E < E_F + k_BT$) and the energy of this level with respect to the conduction band edge. In addition, a second transport regime was predicted, for which the transfer function, $\tilde{j}(\omega)/e\tilde{\Phi}(\omega)$, shows a strong dispersion as a function of the modulation frequency. This is then very similar to the dispersive photocurrent transients, with tails extending over many orders of magnitude of time, which are often observed in time-of-flight (TOF) experiments with amorphous semiconductors [15–20].

In this chapter, we report on the characteristics of electron transport through macroporous GaP networks, between 10 and 100 μm thick, filled with different electrolyte solutions. It is first shown that the transfer function, $\tilde{j}(\omega)/e\tilde{\Phi}(\omega)$, corresponds to the regime of *non-dispersive* transport, which means that there is a *characteristic* average transit time for *all* electrons travelling through the system. It will become clear that this transit time is determined by multiple trapping/detrapping of electrons in states in the band gap, and that the effective density of trap levels at the electron Fermi level can be determined. We measured the density-of-states (DOS) profile in a considerable energy region of the band gap by scanning the electron Fermi level. This was accomplished by varying the background light intensity over five orders of magnitude. First, we provide experimental results showing that electron transport in porous GaP under steady-state conditions is, to a large extent, non-dispersive; in a second part we derive the DOS profile from the transfer function. Finally, we compare our method with other methods that have been proposed for determination of the DOS profile, and we discuss the possible nature of the trap levels.

6.2 Experimental methods

The experiments were performed on a *n*-GaP single crystal grown by the Czochralsky liquid encapsulation method with a sulphur donor density of 5×10^{17}/cm^3. 350 μm thick wafers were exposed to the electrolyte. The *n*-type GaP was made porous by anodic etching in the dark in 0.5 M H_2SO_4 at a potential of 10 V vs. Ag/AgCl.

The electrochemical experiments were performed in a conventional three electrode cell with a porous GaP electrode, a platinum counter electrode and a Ag/AgCl electrode as reference. The electrode potentials are given with respect to that of the reference electrode. The potential was applied using a PAR 273A potentiostat. In addition, an SI 1255 frequency response analyzer from Schlumberger was

used for measurement of the transfer function $\tilde{j}(\omega)/e\tilde{\Phi}(\omega)$ in the frequency region between 0.1 and 1000 Hz. All measurements were performed at 20°C. The electrolytes were prepared from distilled water and analytical grade reagents.

The source of illumination for the impedance measurements was an argon-ion laser tuned at λ = 514.5 nm ($h\nu$ = 2.41 eV; the band gap of GaP is 2.24 eV). Uniform light intensity at the electrode surface was achieved by means of a Newport beam expander. The 632.6 nm line (1.96 eV) of a He-Ne laser was used to photo-etch porous GaP electrodes to increase the porosity. The principle of this photoetching with sub-band gap light has been discussed in previous work of our group [21, 22].

6.3 Evidence for non-dispersive, trap-limited transport

Figure 6.3A shows a complex plane representation of the optoelectrical transfer function, $\tilde{j}(\omega)/e\tilde{\Phi}(\omega)$, measured with a porous GaP photoelectrode (the thickness of the porous layer is 40 μm) illuminated from the side opposite to the collecting contact (Figure 6.2). In Figure 6.3B and C, the imaginary and real components of the transfer function are plotted as a function of the modulation frequency ω. The low frequency limit of $\tilde{j}(\omega)/e\tilde{\Phi}(\omega)$ is a point on the real axis equal to the differential photocurrent quantum yield at a given steady-state light intensity Φ; i.e. $\partial j/e\partial\Phi$. With porous GaP photoanodes, $\partial j/e\partial\Phi$ is (almost) equal to one, since electrons and holes are effectively separated under anodic conditions [5]. At higher frequencies the imaginary component of $\tilde{j}(\omega)/e\tilde{\Phi}(\omega)$ shows a minimum; the corresponding characteristic modulation frequency will be denoted as ω_m. At modulation frequencies above ω_m, the plot of $\tilde{j}(\omega)/e\tilde{\Phi}(\omega)$ passes from the [+,-] quadrant to the [-,-] quadrant. Finally, $\tilde{j}(\omega)/e\tilde{\Phi}(\omega)$ becomes zero at sufficiently high frequencies. Similar results were obtained with nanoporous, particulate TiO_2 photo-electrodes [8–13].

In an early study of electron transport in porous GaP [23], our group has shown that the characteristic time of the transfer function, i.e. $1/\omega_m$, is orders of magnitude longer than the charge/discharge time constant of the cell; this means that the photocurrent response, $\tilde{j}(\omega)/e\tilde{\Phi}(\omega)$, corresponds directly to the motion of photogenerated carriers in the porous system. In a recent paper, an analytical expression for the transfer function was derived [14]:

$$\frac{\tilde{j}(\omega)}{e\tilde{\Phi}(\omega)} = \frac{1}{1 - i\omega\tau_d(1+\Sigma)/\alpha d}\left[\frac{1 - e^{-i\omega\tau_d(1+\Sigma)}}{i\omega\tau_d(1+\Sigma)} - \frac{1 - e^{-\alpha d}}{\alpha d}\right] \qquad (6.1)$$

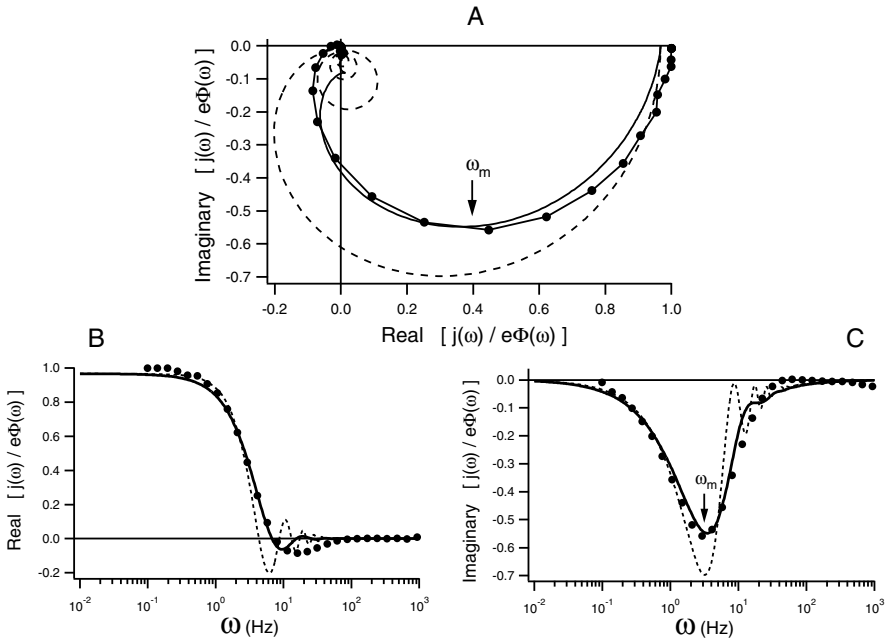

Figure 6.3: A The optoelectrical transfer function (•'s connected with lines), presented in the complex plane, measured with a porous GaP electrode ($d = 40$ μm) permeated with an aqueous 0.5 M H_2SO_4 solution at a light intensity, Φ, of 2×10^{14}/cm^{2}s. The transit time of the electrons through the structure, $\tau(d, \langle n \rangle)$, is equal to $3/\omega_m$, ω_m being the characteristic frequency. B and C show the Bode plots of the real and the imaginary part of the optoelectrical transfer functions (•'s), plotted versus the modulation frequency, ω. The dashed lines present the theoretical plot according to Equation 6.1. The solid lines present the theoretical plots for the case in which a Gaussian distribution around the average transit time is assumed. ω_m can be obtained from the minimum in the imaginary part of the optoelectrical transfer function.

In this equation, τ_d is the trap-free transit time of electrons through the system. Σ denotes the exchange function; this complex function describes the dynamics of exchange between the *excess* density of free electrons and the electron levels in the band gap. The steady-state occupation of the band gap states is in accordance with Fermi-Dirac statistics.

It has been shown that, if the trap-free transit time ($\tau_d = d^2/D$ with the bulk diffusion coefficient D) is considerably longer than the longest localization time of an electron in a trap (thus close to the electron Fermi level), Σ is equal to its low-frequency limit (a real number) in the entire frequency range of interest ($0 < \omega < 10/\tau_d$) [14]. In this case, electron transport is non-dispersive. This means that a packet of excess electrons travels with a constant velocity through the system; nevertheless this velocity can be reduced strongly due to multiple trapping/detrapping. From Equation 6.1, it can be shown that, according to reference [14], the effective transit time corresponds to $3/\omega_m$ and is given by:

$$\frac{3}{\omega_m} = \tau_d \left[1 + \frac{k_B T \Sigma_i s_i(E_F)}{\langle n \rangle}\right] \tag{6.2}$$

We denote the effective, trap-limited transit time as $\tau(d, \langle n \rangle)$, where $\langle n \rangle$ stands for a typical concentration of free electrons in the system averaged over the spatial coordinate along the path of the electrons, under steady-state conditions. Equation 6.2 indicates that the attenuation of electron transport is due mainly to trapping in states around the electron Fermi level E_F; the position of this level with respect to the bottom of the conduction band E_C is determined by $\langle n \rangle$, i.e. $n/N_C = e^{(E_F - E_C)/k_B T}$. In Equation 6.2, $k_B T \Sigma_i s_i(E_F)/\langle n \rangle$ is the low frequency limit of Σ; $k_B T \Sigma_i s_i(E_F)$ is the effective density of states (per unit of volume) at the Fermi-level. If $k_B T \Sigma_i s_i(E_F)/\langle n \rangle \gg 1$, the transit time of the electrons is determined by multiple trapping; it is then equal to the product of the number of trapping events (in traps at the Fermi-level) and the release time.

We plotted the transfer function given by Equation 6.1, assuming that the exchange function Σ is real; $\tau(d, \langle n \rangle)$ has been set equal to $3/\omega_m$. In Figure 6.3A, it can be seen that the shape of the plot of the theoretical transfer function (dashed line) shows the same essential features as the experimental result. The frequency dispersion predicted by theory is compared with the experimental results in Figure 6.3B. The dispersion in the experimental data is stronger than predicted by Equation 6.1. A possible explanation is that the driving force in the region of light absorption, i.e. $0 < x < 1/\alpha$ ($1/\alpha \leq 3$ μm in this work), is considerably smaller than the average value set to $2k_B T/d$. This means that the transit time of the packet of excess electrons gets dispersed, especially in the first part of the

transport path. This is not accounted for in our theoretical treatment [14]. Other explanations could be a dispersion in the thickness of the porous layer, a dispersion in the length of the transport path and a dispersion in the density of states of the trapping levels. A convincing agreement between theory and experiment is obtained, when a Gaussian distribution around the average value of the transit time $\tau(d, \langle n \rangle)$ is taken (see Figure 6.3 solid lines, full width at half maximum is 0.5 times $\tau(d, \langle n \rangle)$). In reference [14], the transfer function was considered for the case of dispersive transport (where Σ has an imaginary component). Then, the representation of the transfer function in the complex plane is essentially different from the experimental result shown here; furthermore, the dispersion of the transfer function with the modulation function is much stronger than we observed experimentally in the case of GaP. This leads us to conclude that electron transport in macroporous GaP under the given conditions is non-dispersive.

From the experimental result in Figure 6.3, it follows that the transit time $3/\omega_m$ through a porous layer 40 μm thick (at a steady-state light intensity, Φ, of $2 \times 10^{14}/\text{cm}^2\text{s}$) is 1 s. We can estimate the trap-free transit time of the electrons through the system using:

$$\tau_d = \frac{d}{\mu_e \langle F \rangle} \tag{6.3}$$

Here, μ_e is the mobility of electrons in the conduction band of GaP, equal to about 100 cm^2/Vs [24] and $\langle F \rangle$ is the average value of the statistical driving force for diffusive transport. In previous work [7], we showed that the driving force for electron transport, i.e. the gradient of the electron Fermi level in the direction of the transport path, is nearly independent of the position in the system (except for the region $0 < x < 1/\alpha$). A good estimate for the average driving force over the entire system, $\langle F \rangle$, is $2k_BT/ed$. The trap-free transit time of electrons diffusing through a system of thickness d then becomes:

$$\tau_d = \frac{d}{\mu_e \langle F \rangle} = \frac{d^2}{2(k_BT/e)\mu_e} \tag{6.4}$$

For a porous GaP system with a thickness of 40 μm, the trap-free transit time is then calculated to be 3×10^{-6}s taking the bulk mobility μ_e equal to 100 cm^2/Vs. This is 3×10^5 times shorter than the experimental transit time measured with a background light intensity of $2 \times 10^{14}/\text{cm}^2\text{s}$, which is 1 s. We must thus conclude that the transport of free carriers in macroporous GaP is strongly attenuated. In principle, scattering of the electrons with the internal surface of the porous system may lead to a reduction of the mobility of the free electrons. However, the

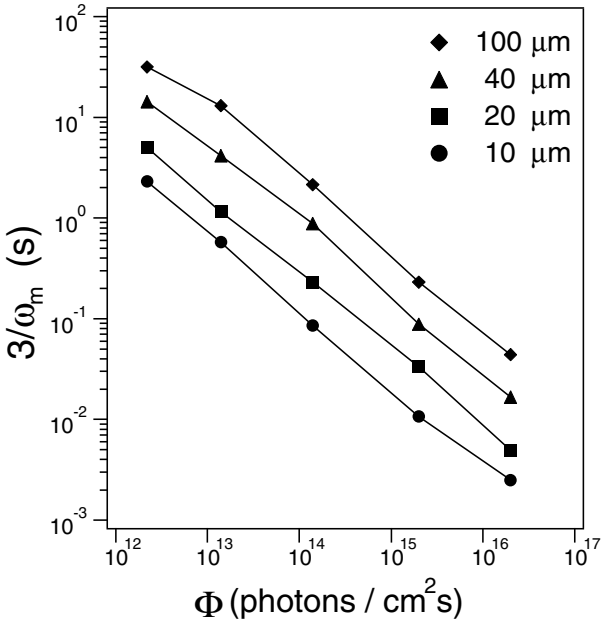

Figure 6.4: The transit time for the electrons in macroporous GaP, $3/\omega_m$, for a 10 (●), 20 (■), 40 (▲), and 100 (◆) μm thick layer of porosity 25%, measured in an aqueous 0.5 M H_2SO_4 solution. The transit time was measured with intensity-modulated photocurrent spectroscopy (IMPS) as a function of the light intensity. The double-logarithmic plot is used to present all data in one figure, and the lines are a guide to the eye.

mean free path for scattering of electrons with the lattice (phonons) is only a few nanometers. Since the structural units of the porous GaP system have dimensions in the 100 nm range, surface scattering is not expected to be important. The strong attenuation of electron transport in porous GaP must be due to multiple trapping of the diffusing electrons in band gap states. This is strongly supported by the fact that the transit time in a system of a given thickness is determined by the background light intensity Φ.

In Figure 6.4, the transit times, i.e. $3/\omega_m$, measured with porous GaP systems with a thickness of 10, 20, 40, and 100 μm, are plotted as a function of Φ (a double logarithmic plot is used to show all data in one figure). The transit time decreases strongly with increasing light intensity. Similar results have been obtained with particulate, nanoporous TiO_2 [8–13]. This feature is characteristic for non-dispersive transport controlled by multiple trapping. An increase in the light

intensity leads to an increase in the density of free electrons in the conduction band, hence to an upwards shift of the electron Fermi level E_F with respect to the edge of the conduction band, E_C. The main localization time, i.e., in traps close to E_F, is proportional to $e^{(E_C-E_F)/k_BT}$; an upwards shift of E_F with respect to E_C reduces the localization time of the electrons in traps. The relationship between the density of free electrons in the conduction band and the absorbed light intensity, has been considered in reference [7]. When the collection of the photogenerated carriers is sufficiently fast, it is found that the average density of free electrons is given by:

$$\langle n \rangle = \frac{1}{d}\int_0^d n(x)dx = \Phi\frac{d}{2(k_BT/e)\mu_e} \tag{6.5}$$

It should be remarked that, for a given value of the absorbed light intensity Φ, the average density of free electrons $\langle n \rangle$ increases with increasing thickness of the system; this is due to the fact that the driving force for directed diffusion is proportional to d^{-1}. Substitution of Equations 6.4 and 6.5 into Equation 6.2, gives the transit time as a function of the external parameters d and Φ:

$$\frac{3}{\omega_m} = \tau(d, \langle n \rangle) = d\frac{k_BT\Sigma_i s_i(E_F)}{\Phi} \tag{6.6}$$

The density of states at a given position of the electron Fermi level, $k_BT\Sigma_i s_i(E_F)$, can be determined from the transit time. In principle, the results obtained with porous layers of different thickness should lead to a single DOS function.

6.4 The density-of-state function

In Figure 6.5, the density-of-states, $k_BT\Sigma_i s_i(E_F)$, is presented as a function of the position of the electron Fermi level in the band gap (the results present the number of states per unit of *geometrical* volume, hence containing the GaP permeated with the electrolyte solution). The results presented in Figure 6.5A are obtained from the data of Figure 6.4, which were measured with porous GaP layers 10, 20, 40, and 100 μm thick. These data lead clearly to a single DOS function; this shows that the steady-state transport theory of reference [7] is sufficiently accurate to account for the effect of the variable thickness of the porous layers. The density of states is about $10^{16}/\text{cm}^3$ deep in the gap (0.7 eV below E_C), and increases, roughly exponentionally, with increasing energy, up to a value of $1.5 \times 10^{17}/\text{cm}^3$ at 0.4 eV below E_C.

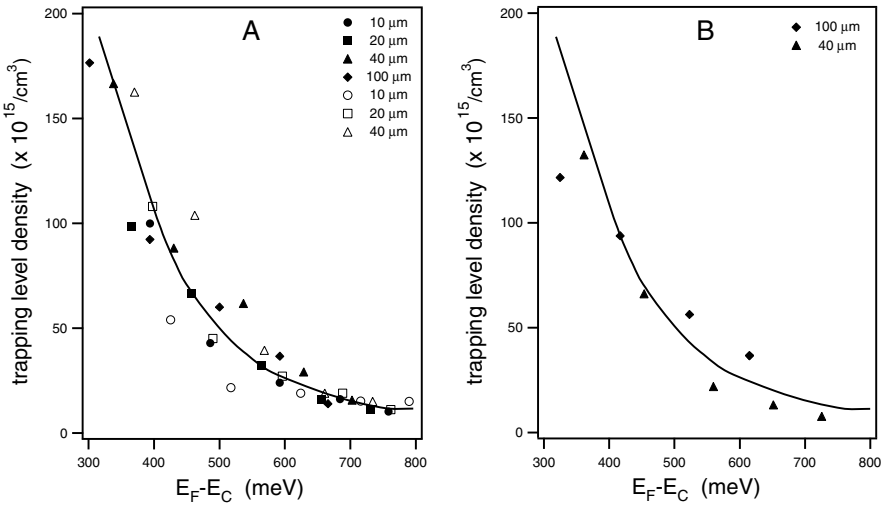

Figure 6.5: A The density of trapping levels $2k_BT\Sigma_i s_i(E_F)$ as a function of the position in the band gap of macroporous GaP (porosity is 25%) is shown. The data were obtained from Figure 6.4 supplemented with three other samples. The thickness of the porous layer is indicated in the graph. The density of state function is roughly exponential as indicated by the solid line. B The data shown in this picture are obtained from two samples. These samples have been etched photoanodically to increase the porosity to 50%. The solid line obtained from A is shown as a guide to the eye.

We measured the DOS with porous GaP permeated with other electrolyte solutions. An aqueous electrolyte solution was used, in which Fe^{2+} was added as a hole scavenger. We also used propylene carbonate (PC) with I_3^- as a hole scavenger. The hole scavengers were used to prevent the photoelectrochemical dissolution of the porous GaP. The results were similar to those obtained with the aqueous 0.5 M H_2SO_4 electrolyte. The DOS function was also measured for samples which were photoanodically etched with sub-band gap light [6], to increase the porosity from 25% to 50%. The results from these measurements are presented in Figure 6.5B. It can be seen that the DOS function does not change on changing the porosity of the GaP structure from 25% to 50%.

6.5 Discussion

Measurement of the photocurrent response to a harmonic modulation of the light intensity for the study of the density of states in the band gap of a semiconductor

has been proposed by several research groups [25–28]. There has been much discussion about the precise interpretation of the results [25–29]. The method was used mainly to investigate amorphous intrinsic semiconductors in *p-i-n* type devices. A full comparison of the work in references [25–29] with the method used here is beyond the scope of this chapter. There are, however, important differences with the work that is presented here. We consider them briefly. First, the photocurrent in *p-i-n* type devices is, in principle, due to the motion of electrons and holes. This complicates the analysis since the precise contributions of electrons and holes to the modulated photocurrent $\tilde{j}(\omega)$ has to be known [29]. Moreover, electron-hole recombination during the transport of both types of carrier in the intrinsic layer has to be taken into account [25–29]. In our work, the modulated photocurrent is due completely to the motion of electrons in the porous GaP, because the photogenerated holes are directly transferred to the electrolyte solution in the pores. Electron-hole recombination during the transport of electrons is absent which makes the kinetic analysis simpler [14]. We conclude that the conditions under which electron transport has been studied here allow a straightforward analysis of the rate equations.

There is, in addition, a fundamental difference between the work presented here and the 'modulated photocurrent method' proposed by Oheda and later discussed by several other research groups [25–28]. Oheda considers the phase shift between $\tilde{j}(\omega)$ and $\tilde{\Phi}(\omega)$ at relatively high frequencies. In that case, the excess free carriers are in electronic equilibrium with the electrons in shallow traps, but not with the deeper traps closer to the electron Fermi-level. A demarcation level is defined between the shallow and deep levels, which shifts upward with increasing modulation frequency. In our work, the modulation frequency is in the range for which the electrons in all the traps located above the electron Fermi-level are in equilibrium with the excess electrons, generated by the modulation signal $\tilde{\Phi}(\omega)$. Since Fermi-statistics can be applied, the rate of electron capture in a trap is related directly to the localization time in the trap. This means that all traps have the same effect on the attenuation of electron transport, irrespective of the capture cross section for trapping. As an important result, in our method the DOS function corresponds to *all* the electron levels in the band gap. In the methods discussed in references [25–28], only states with a single capture cross section are considered in the analysis.

We scanned the electron Fermi-level through the upper half of the band gap of porous GaP, between 0.8 and 0.3 eV below the conduction band, by changing the background light intensity over five orders of magnitude. The determination of the position of the electron Fermi level with respect to the conduction band edge, is

based on the application of the transport model for steady-state conditions [7]. In this model, it is assumed that there is no recombination and that the electron transfer from the porous system into the collecting contact is sufficiently fast. The first assumption is supported by the observation of photocurrent quantum yields close to unity [5]. The second assumption is supported by the fact that the characteristic time observed with the transfer function, $\tilde{j}(\omega)/e\tilde{\Phi}(\omega)$, depends on the thickness of the porous layer (see for instance Figure 6.4); this time is thus not determined by electron transfer from the porous GaP network into the bulk GaP. Clearly, the characteristic time observed from $\tilde{j}(\omega)/e\tilde{\Phi}(\omega)$ is the time that the photogenerated electrons need to travel through the system. This time is determined by multiple trapping/detrapping, and we showed that the DOS function in the band gap of porous GaP can be determined making use of the data obtained with samples of different thicknesses.

We observe that the density of band gap states in macroporous GaP is about $10^{16}/\text{cm}^3$ at 0.8 eV below E_C and increases, roughly exponentionally, with increasing energy up to a value of $1.5 \times 10^{17}/\text{cm}^3$ at 0.3 eV below E_C. Bulk GaP has been characterized in detail by photoelectrochemical and other methods in the past [5]. There is no evidence for band gap states in such a high density in single crystalline non-porous GaP. Porous etching leads to a single crystalline network, and this mild electrochemical process is not expected to enhance the density of bulk defects. We therefore conclude that the band gap states involved in electron trapping, are located at the interface of the porous GaP and the electrolyte. This is, furthermore, supported by the fact that there is a considerable absorption of sub-band gap light in macroporous GaP (and not in bulk GaP) found to be due to optical transitions of interfacial electrons [21, 22]. Our results do not give insight into the chemical nature of the band gap states. It is clear that replacing the aqueous electrolyte solution by a non-aqueous solution does not change the DOS function. Investigation of the chemical nature of the interfacial states will require state of the art *in situ* techniques such as surface sensitive IR spectroscopy [30, 31].

A density of band gap states that rises exponentially with increasing energy towards the conduction band edge has often been found with amorphous semiconductors, such as α-Si:H [15]. We observed a similar DOS function in macroporous GaP in the energy region 0.8-0.3 eV below the conduction band edge. However, the origin and chemical nature of these band gap states, very probably located at the GaP/electrolyte interface, must be different from that of the tail states observed in amorphous semiconductors. Changing the porosity from 25% (Figure 6.5A) to 50% (Figure 6.5B) did not seem to affect the volumetric denstity of states which would imply a similar internal surface for both porosities. Interest-

ingly, an exponential distribution of the band gap states has been reported recently for nanoporous TiO_2 electrodes, permeated with acetonitrile solutions [32].

6.6 Conclusions

We found that electron transport in macroporous GaP filled with aqueous and non-aqueous electrolytes is non-dispersive under steady-state conditions. Transport is characterized by a single transit time that depends on the thickness of the porous layer and the background light intensity, and is determined by multiple trapping in interfacial states close to the electron Fermi level. The DOS function can be determined from the transit time by scanning the electron Fermi level through a considerable region of the band gap.

References

[1] B. O'Regan and M. Grätzel, *Nature* **353**, 737 (1991).

[2] G. Hodes, I.D. Howell and L.M. Peter, *J. Electrochem. Soc.* **139**, 3136 (1992).

[3] A. Köhler, D.A. dos Santos, D. Beljonne, Z. Shuai, J.-L. Bredas, A.B. Holmes, A. Kraus, K. Mullen and R.H. Friend, *Nature* **392**, 903 (1998).

[4] U. Bach, D. Lupo, P. Comte, J.E. Moser, F. Weissortel, J. Salbeck, H. Spreitzer and M. Grätzel, *Nature* **395**, 583 (1998).

[5] B.H. Erné, D. Vanmaekelbergh and J.J. Kelly, *Adv. Mater.* **7**, 739 (1995).

[6] F.J.P. Schuurmans, D. Vanmaekelbergh, J. van de Lagemaat and A. Lagendijk, *Science* **284**, 141 (1999).

[7] D. Vanmaekelbergh and P.E. de Jongh, *J. Phys. Chem. B* **103**, 747 (1999).

[8] K. Schwarzburg and F. Willig, *Appl. Phys. Lett.* **58**, 2520 (1991).

[9] F. Cao, G. Oskam, G.J. Meyer and P.C. Searson, *J. Phys. Chem* **100**, 17021 (1996).

[10] P.E. de Jongh and D. Vanmaekelbergh, *Phys. Rev. Lett.* **77**, 3427 (1996).

[11] L. Dloczik and I. Uhlendorf, *J. Phys. Chem. B* **101**, 10281 (1997).

[12] P.E. de Jongh and D. Vanmaekelbergh, *J. Phys. Chem. B* **101**, 2716 (1997).

[13] A. Solbrand , H. Lindström , H. Rensmo, A. Hagfeldt , S.-E. Lindquist and S. Södergren, *J. Phys. Chem. B* **101**, 2514 (1997).

[14] D. Vanmaekelbergh and P.E. de Jongh, *Phys. Rev. B* **61**, 4699 (2000).

[15] R.A. Street, *Hydrogenated Amorphous Silicon*, Cambridge Solid State Science Series, edited by R.W. Chahn, E.A. Davis and I.M. Ward, Cambridge University Press, Cambridge, (1991).

[16] H. Scher and E.W. Montroll, *Phys. Rev. B* **12**, 2455 (1975).

[17] G.F. Seynhaeve , R.P. Barclay, G.J. Adriaenssens and J.M. Marshall, *Phys. Rev. B* **39**, 10196 (1989).

[18] H. Scher, M.F. Shlesingerand J.T. Bendler, *Phys. Today* **44**, 26 (1991).

[19] A. Jakobs and K. W. Kehr, *Phys. Rev. B* **48**, 8780 (1993).

[20] B. Hartenstein, H. Bässler, A. Jakobs and K.W. Kehr, *Phys. Rev. B* **54**, 8574 (1996).

[21] D. Vanmaekelbergh and L. van Pieterson, *Phys. Rev. Lett.* **80**, 821 (1998).

[22] D. Vanmaekelbergh, M.A. Hamstra and L. van Pieterson, *J. Phys. Chem. B* **102**, 7997 (1998).

[23] D. Vanmaekelbergh, F. Iranzo Marinand J. van de Lagemaat, *Ber. Bunsenges. Phys. Chem.* **100**, 616 (1996).

[24] S.M. Sze, *Semiconductor Devices: Physics and Technology*, Wiley, New York (1985).

[25] H. Oheda, *J. Appl. Phys.* **52**, 6693 (1981).

[26] R. Brüggemann, C. Main, J. Berkinand S. Reynolds, *Philos. Mag. B* **62**, 29 (1990).

[27] G.J. Adriaenssens, S.D. Baranovskii, W. Fuhs, J. Jansenand Ö. Öktü, *Phys. Rev. B* **51**, 9661 (1995).

[28] H. Cordes, G.H. Bauerand R. Brüggemann, *Phys. Rev. B* **58**, 16160 (1998).

[29] C. Longeaud and J. P. Kleider, *Phys. Rev. B* **45**, 11672 (1992).

[30] B.H. Erné, F. Ozanam and J.-N. Chazalviel, *Phys. Rev. Lett.* **80**, 4337 (1998).

[31] L.M. Peter, D.J. Blackwood and S. Pons, *Phys. Rev. Lett.* **62**, 308 (1989).

[32] J. van de Lagemaat and A.J. Frank, *J. Phys. Chem. B* **104**, 4292 (2000).

Samenvatting

Het belang van elektronen-geleiding in vaste stoffen zal iedereen onderkennen die iets afweet van elektriciteit. Elektriciteit voorziet een groot deel van de energie behoefte in het dagelijks leven. Bijvoorbeeld in zonnecellen wordt gebruik gemaakt van optische overgangen waarmee de energie van zonlicht in elektrische energie wordt omgezet. De zonnecel is hiertoe in staat door de bijzondere elektronische eigenschappen van het gebruikte materiaal. In dit proefschrift worden de elektronische eigenschappen van lagen van zinkoxide (ZnO) nanokristallen besproken die kwantum effecten vertonen. De elektronische eigenschappen betreffen het transport van elektronen door deze lagen, en de optische overgangen.

ZnO is een halfgeleidend materiaal; een halfgeleider gaat pas geleiden als elektronen door absorptie van warmte of licht in de aangeslagen toestand komen. De werking van een zonnecel is gebaseerd op de absorptie van licht door elektronen die in een hogere energietoestand komen. Het bijzondere van een zuivere halfgeleider is dat het twee energiebanden heeft die zijn gescheiden door een verboden zone, de bandafstand (band gap). De band met de laagste energie heet de valentieband en is compleet gevuld met elektronen. De band met de hoogste energie heet de geleidingsband en hier zijn geen elektronen aanwezig. In de verboden zone zijn geen energieniveaus en dus kunnen hier geen elektronen verblijven. Door een halfgeleider te belichten of te verwarmen kunnen elektronen vanuit de valentieband naar de geleidingsband worden geëxciteerd. Of dit al met warmte of alleen met licht gebeurt, hangt af van de grootte van de bandafstand en dus de hoogte van de energie. Het licht moet dan een energie hebben die groter of gelijk is aan de bandafstand. Het elektron bevindt zich nu in een geleidingsniveau en kan vrij bewegen in het materiaal. Een elektron heeft een eenwaardig negatieve lading. De positie waar het elektron zich eerst bevond in de valentieband is nu leeg en eenwaardig positief geladen. Dit lege niveau wordt een gat genoemd. Het gat kan ook voor geleiding zorgen net als een elektron in de geleidingsband.

De ZnO kristallen die worden beschreven in dit werk zijn heel erg klein en

worden daarom nanokristallen genoemd. Nano slaat op de afmeting van de kristallen. De diameter van de bijna bolvormige kristallen die in dit werk zijn gebruikt, varieert van 3 tot 6 nanometer. Een nanometer is een miljardste deel van een meter en verhoudt zich ongeveer tot de meter als een tafelvoetbal-balletje tot de aarde. Omdat de afmeting van de nanokristallen zo klein is, treden er eigenaardige effecten op. De banden houden op te bestaan; in plaats hiervan zijn er discrete energieniveaus. De afstanden tussen deze discrete energieniveaus en de verboden energiezone van de halfgeleider nemen toe naarmate de kristallen kleiner worden. Deze bijzondere eigenschap wordt ook wel het kwantum-effect genoemd en de nanokristallen die dit effect vertonen, kwantum dots.

In hoofdstuk 2 worden de kwantum dots stapsgewijs opgevuld met elektronen. Dit wordt bereikt met een elektrochemisch systeem. Hiertoe worden de lege ruimtes in de laag van de bolvormige ZnO kristallen opgevuld met een elektroliet-oplossing. Vervolgens wordt er met behulp van een elektrische spanning lading in de ZnO laag geïnjecteerd welke gecompenseerd wordt door positieve ionen in het elektroliet. De elektronen bevinden zich in de geleidings-energie niveaus van de kwantum dots. De hoeveelheid lading die in de laag kan worden gebracht wordt gemeten als functie van de toegevoegde energie. Deze capaciteits-karakteristiek geeft ons de ligging van de discrete energieniveaus van de ZnO kwantum dots. Omdat de ligging van deze niveaus afhankelijk is van de grootte van de nanokristallen en onze lagen bestaan uit kwantum dots met een spreiding in de deeltjesgrootte, zien we ook een spreiding in de energieniveaus. Voor de metingen van de geleiding in de ZnO lagen worden twee geleidende goudcontacten op een niet geleidend substraat aangebracht (glas). Het ene contact wordt de bron genoemd (source) en het andere de afvoer (drain). Het geleidingsvermogen wordt bepaald door de elektronenstroom tussen de bron en de afvoer te meten bij een klein spanningsverschil tussen deze twee contacten. In hoofdstuk 2 wordt gevonden dat er twee kwantum gebieden zijn met een specifieke elektronenmobiliteit: als de electronenconcentratie $\langle n \rangle$ tussen 0 en 2 ligt, en als $\langle n \rangle$ tussen 2 en 8 ligt. Dit wordt verklaard met het feit dat het eerste discrete energieniveau (dit wordt het *S* niveau genoemd) tweevoudig ontaard is (twee niveaus met dezelfde energie) en dus twee elektronen kan bevatten. Het tweede discrete energieniveau (dit wordt het *P* niveau genoemd) is zesvoudig ontaard en kan zes elektronen bevatten. Deze volgorde van energieniveaus wordt ook gevonden bij atomen. ZnO kwantum dots bezet met een aantal elektronen, kunnen dus ook opgevat worden als kunstmatige atomen.

In hoofdstuk 3 wordt de invloed van het elektroliet op de elektronische eigenschappen van de ZnO lagen bekeken. In een waterige elektroliet oplossing blij-

ven de *S* en *P* niveaus twee- en zesvoudig ontaard. Nu worden deze resultaten vergeleken met de oplading van de ZnO kwantum-dot lagen doordrenkt met een organisch elektroliet (propyleen carbonaat). Het blijkt dat het nu extra energie kost om het tweede elektron in het *S* niveau te krijgen. Dit komt omdat de elektronen in deze niveaus elkaar afstoten, de zogenaamde Coulomb-repulsie. In het waterige elektroliet werd geen Coulomb-repulsie waargenomen. Dit wordt toegeschreven aan het feit dat er protonen aanwezig zijn in water. Het proton is het kleinst mogelijke positieve ion en kan zich waarschijnlijk prima aan het oppervlak van het ZnO hechten om daar de negatieve lading van de elektronen te compenseren. In propyleen carbonaat zijn geen protonen aanwezig. De Coulomb-repulsie zorgt ervoor dat met hetzelfde relatieve spanningsverschil en dus dezelfde energie veel minder elektronen in de ZnO laag kunnen worden gebracht dan in het waterige elektroliet. De Coulomb-repulsie kan worden bepaald uit de capaciteitskarakteristiek. De Coulomb-repulsie kan ook worden bepaald door het geleidingsvermogen te meten als functie van de temperatuur. Hiertoe werd een ZnO laag in propyleen carbonaat of alcohol afgekoeld tot een temperatuur van maximaal -120°C. De Coulomb-repulsie wordt vervolgens berekend uit de temperatuursafhankelijkheid van het geleidingsvermogen. Er wordt ook een verandering van de mobiliteit waargenomen bij dezelfde waarde van $\langle n \rangle$ in de verschillende elektrolieten. In propyleen carbonaat is de mobiliteit twee- tot driemaal hoger dan in water. Een mogelijke oorzaak hiervoor is een verandering van de chemische samenstelling van het ZnO oppervlak.

De discrete energieniveaus van de kwantum dots kunnen ook op een directe manier onderzocht worden. In hoofdstuk 4 wordt hiervoor gebruik gemaakt van infrarood (IR) straling. IR heeft een energie die lager is dan het rode licht uit het zichtbare gebied; het wordt ook wel warmtestraling genoemd. De energiescheiding tussen de discrete energieniveaus valt precies in het IR-energiegebied. Elektronen die zich in de discrete energieniveaus bevinden kunnen nu met IR-straling naar een ander (hoger) discreet energieniveau worden gebracht. Een elektron in het *S* niveau kan bijvoorbeeld naar het daarbovenliggende *P* niveau worden gebracht. Er zijn nog meer discrete energieniveaus in de geleidingsband behalve het *S* en *P* niveau, namelijk het *D, F* en *S'* niveau. De overgangen tussen deze energieniveaus zijn niet allemaal toegestaan. Voor het wel of niet optreden van deze overgangen bestaan regels. Met behulp van deze regels wordt de IR-absorptie (het opnemen van energie) van de ZnO lagen verklaard. Deze absorptie is sterk afhankelijk van de gemiddelde hoeveelheid elektronen die zich per ZnO nanokristal in de laag bevindt. Met de resultaten van de IR-metingen wordt het energieverschil tussen de discrete energieniveaus bepaald, en ook de waarschijn-

lijkheid van de optische overgang tussen deze niveaus.

Halfgeleiders kunnen licht absorberen maar na absorptie van licht ook weer licht uitzenden (emissie). In hoofdstuk 5 maken we gebruik van dit effect. Het is al meer dan een eeuw bekend dat ZnO een groene emissie bezit die veelvuldig gebruikt is in vacuüm fluorescerende schermen. Zoals eerder vermeld kan een elektron vanuit de valentieband naar de geleidingsband worden gebracht (het aanslaan van een elektron) als genoeg energie wordt toegevoegd. In geval van ZnO moet dit ultraviolet (UV) licht zijn. UV heeft een hogere energie dan zichtbaar licht. Door het aanslaan van een elektron ontstaat een gat in de valentieband. Dit elektron en gat worden samen een exciton genoemd (van exciteren of aanslaan). Het exciton kan weer recombineren, oftewel het elektron kan zijn oude positie in de valentieband weer innemen door het uitzenden van een UV-foton (lichtdeeltje) met een energie gelijk aan de bandafstand; dit wordt de exciton-emissie genoemd. Het gat kan echter ook gevangen worden in een energieniveau dat tussen de geleidings- en valentieband in ligt, dus in de verboden zone. Dit soort energieniveaus ontstaan door fouten in het ZnO kristal. Het gat verliest hierdoor een deel van zijn energie en als het elektron vervolgens met het gat recombineert wordt daarom een foton uitgezonden met een energie kleiner dan de bandafstand. Deze energie valt in het zichtbare gebied en de emissie is meestal blauw of groen. Door met behulp van elektrochemie de elektronenconcentratie in de laag te veranderen kan de emissie worden gestuurd van volledig UV tot volledig zichtbaar.

In het laatste hoofdstuk, hoofdstuk 6, wordt een materiaal beschreven dat niet vermeld wordt in de titel van dit proefschrift, namelijk galliumphosphide (GaP). GaP is ook een halfgeleider net als ZnO. Het materiaal wordt poreus gemaakt met behulp van hoge spanningen en een zuur elektroliet. Door de duur van het etsen te variëren kan de dikte van de poreuze laag worden gevarieerd van ongeveer één tot honderd micrometer. Dit poreuze materiaal bezit niet de kwantum eigenschappen die zijn beschreven voor ZnO. Met deze poreuze lagen wordt het transport van elektronen in ongeordende strukturen bestudeerd. Met licht worden er elektron-gat paren gegenereerd aan het oppervlak van de poreuze laag. De gaten worden afgevangen door het elektroliet dat de poreuze laag doordrenkt. De elektronen moeten echter de hele poreuze laag doorreizen om het achtercontact te bereiken. Het transport van de elektronen door de GaP structuur werd onderzocht met behulp van een optische techniek: intensiteit-gemoduleerde fotostroomspectroscopie (IMPS). Hierbij wordt een karakteristieke frequentie gevonden die de gemiddelde tijd aangeeft die een elektron nodig heeft om het achtercontact te bereiken. Hieruit bleek dat de elektronen er ongewoon lang over deden om het achtercontact te bereiken. Dit wordt enerzijds veroorzaakt door de labyrint-

achtige structuur van het poreuze GaP en anderzijds door de aanwezigheid van vele energieniveaus in de verboden zone die de elektronen in hun reis naar het achtercontact kunnen vangen.

Publications and presentations

Publications related to this thesis

- A.L. Roest, P.E. de Jongh and D. Vanmaekelbergh, Nondispersive trap-limited electron transport in macroporous GaP, *Phys. Rev. B*, **2000**, *62*, 16926. Chapter 6.
- A.L Roest, J.J. Kelly, D. Vanmaekelbergh and E.A. Meulenkamp, Staircase in the electron mobility of a ZnO quantum-dot assembly due to shell filling, *Phys. Rev. Lett.*, **2002**, *89*, 036801. Chapter 2.
- A. Germeau, A.L. Roest, D. Vanmaekelbergh, G. Allan, C. Delerue and E.A. Meulenkamp, Optical transitions in few-electron artificial atoms strongly confined in ZnO nanocrystals, *Phys. Rev. Lett.*, **2003**, *90*, 097401. Chapter 4.
- A.L. Roest, A.J. Houtepen, J.J. Kelly and D. Vanmaekelbergh, Electron-conducting quantum-dot solids with ionic charge compensation, *submitted to Faraday Discussions*, **2003**.
- A.L. Roest, A. Germeau, J.J. Kelly, D. Vanmaekelbergh, G. Allan and E.A. Meulenkamp, Long-range electron transport in an assembly of ZnO quantum dots: the effects of quantum confinement, Coulomb repulsion and structural disorder, *accepted for publication in ChemPhysChem*. Chapter 3.
- A.L Roest, J.J. Kelly, D. Vanmaekelbergh and E.A. Meulenkamp, Temperature dependence of the electron tunnelling activation energy in a ZnO quantum-dot solid, manuscript in preparation. Chapter 3.

Other publications

- J.A. van Bokhoven, A.L. Roest, D.C. Koningsberger, J.T. Miller, G.H. Nachtegaal and A.P.M. Kentgens, Changes in structural and electronic properties of the zeolite framework induced by extra-framework Al and La in H-USY and La(x)NaY: A ^{29}Si and ^{27}Al MAS NMR and ^{27}Al MQ MAS NMR study, *J. Phys. Chem. B*, **2000**, *104*, 6743.

- E.P.A.M. Bakkers, A.L. Roest, A.W. Marsman, L.W. Jenneskens, L.I. de Jong-van Steensel, J.J. Kelly and D. Vanmaekelbergh, Characterization of photoinduced electron tunneling in gold/SAM/Q-CdSe systems by time-resolved photoelectrochemistry, *J. Phys. Chem. B*, **2000**, *104*, 7266.

Oral presentations

- *Using an electrochemical field-effect transistor to determine electron mobilities in quantum-dot layers*, 2001 Joint International Meeting of the Electrochemical Society and the International Society of Electrochemistry, San Fransisco, September 2001.

- *Nondispersive trap-limited electron transport in macroporous n-GaP*, 2001 Joint International Meeting of the Electrochemical Society and the International Society of Electrochemistry, San Fransisco, September 2001.

- *A staircase in the electron mobility of a ZnO quantum-dot assembly due to shell filling*, Joint meeting of the CW study sections Kristal- en Struktuuronderzoek en Chemie van de Vaste Stof en Materiaalkunde, Lunteren, March 2002.

- *Quantum regimes in the electron mobility of a ZnO quantum dot transistor*, 19th General Conference of the EPS Condensed Matter Division held jointly with CMMP 2002-Condensed Matter and Materials Physics, Brighton, April 2002.

Poster

- *Nondispersive trap-limited electron transport in macroporous n-GaP*, The International Workshop on Nanostructures in Photovoltaics, Dresden, July 2001.

Dankwoord

Aan het einde van mijn promotietijd kijk ik terug op vier goede jaren (en drie dagen). Graag wil ik op deze plaats iedereen bedanken die heeft bijgedragen aan het tot stand komen van dit proefschrift.

Als eerste wil ik mijn ouders bedanken. Zij hebben mij geleerd om gebruik te maken van mijn capaciteiten. Ik wil jullie bedanken dat jullie mij de mogelijkheid hebben geboden om te leren en studeren zoals ik heb kunnen doen.

Ik wil mijn begeleiders van mijn groot bijvak (derde jaar) en hoofdvak (vierde jaar) bedanken die met veel enthousiasme hun onderzoek en mijn begeleiding verzorgden. Erik en Jeroen zijn een belangrijke stimulans geweest om zelf te gaan promoveren.

Het onderzoeksvoorstel voor mijn promotie was een lange lijst van mogelijke interessante experimenten. Met behulp van mijn beide promotoren, Daniël en John heeft dit uiteindelijk geleid tot het werk gepresenteerd in dit proefschrift. Het hebben van twee promotoren is een bijzonder luxe situatie gebleken. De verschillen in aanpak, interesse, ervaring, expertise en karakter heb ik altijd als erg positief ervaren. Hooggeleerde heren, waarde promotoren, bedankt!

Het werk in dit proefschrift aan ZnO is gebaseerd op werk van Eric. Dit verschafte mij een solide basis waarop ik verder kon bouwen. De vele gesprekken over practische en theoretische zaken waren voor mij altijd erg stimulerend en naast John en Daniël heeft Eric de grootste invloed gehad op de uiteindelijke inhoud van dit proefschrift. Eric, bedankt voor je enthousiaste en waardevolle begeleiding!

De tight-binding berekeningen werden uitgevoerd door onze Franse vrienden. Je tiens à remercier Christophe Delerue et Guy Allan pour leurs calculs précis des états d'un électron dans une boîte quantique.

Ik heb tijdens mijn onderzoek veel gebruik gemaakt van de expertise van mijn vakgroepsgenoten. Hier wil ik in het bijzonder Sander, Paul en Alexander noemen. De sfeer in onze groep is mij altijd goed bevallen. François, Peter, Floris,

Bert, Marcel, Celso, Cees, Andries en Jessica, hartelijk bedankt voor alle hulp en gezelligheid de afgelopen jaren. Ook de reeds afgezwaaide groepsgenoten verdienen nog een vermelding in dit dankwoord. Liesbeth, Addy, Ageeth, Arjan, Petra, Koert, René, Xinghua, Willem en Freek jullie hebben natuurlijk net zoveel bijgedragen aan de goede sfeer als de huidige vakgroepsgeneratie. Net als de vele studenten die onze vakgroep hebben bevolkt tijdens mijn aanwezigheid en waarvan velen bereid waren mij te helpen bij het stillen van mijn dagelijkse tafelvoetbal behoefte. Ik heb studenten en zelfs scholieren mogen begeleiden in allerlei fasen van hun studie en dit is mij altijd erg goed bevallen. Marieke is de enige hoofdvak student geweest in deze verzameling en zij heeft een belangrijke bijdrage geleverd aan de luminescentie resultaten beschreven in mijn proefschrift.

Er is natuurlijk ook een speciale plaats voor mijn vier kamergenoten: Ferry, Erik, Zeger en Arjan. Ferry was een enthousiast medetafelvoetballiefhebber en een gezellige aanvulling op ons kamergezelschap. Erik is al eerder genoemd en ik wil hieraan toevoegen dat vooral de squashpartijen, zowel op de squashbaan als in onze zitkamer, mij zeer goed zijn bevallen. Zeger was mijn theoretische vraagbaak bij uitstek die in vloeiend Vlaams al mijn problemen deed verdwijnen. Arjan als laatste, mijn huidige kamergenoot. Het was wel erg stil geworden in mijn eentje; bedankt voor je interesse in mijn werk (en je computer met geluidskaart).

Een belangrijk aspect van mijn onderzoek wordt niet of nauwelijks beschreven in dit proefschrift. Voor ieder experiment wordt gebruik gemaakt van technische voorzieningen zoals speciaal op maat gemaakte meetcellen en computerprogramma's. Hans was de man waarbij ik vier jaar bijna wekelijks over de vloer kwam voor de meeste van mijn technische problemen. Zijn goede contacten met de technische afdelingen van de faculteiten scheikunde en natuurkunde zijn een waardevol bezit. Stephan heeft veel ondersteuning verleent door meetprogramma's te schrijven voor onze computergestuurde opstellingen. Ook persoonlijke computerproblemen werden meestal snel opgelost. Nico, Jan en Johan verzorgen onder meer het vloeibare helium en alle andere gassen die je maar kunt wensen. Ook Paul, Cees en Gerrit, de technici van de fysische groepen, hebben kleinere en grotere technische problemen helpen oplossen. Heren bedankt!

Als laatste wil ik mijn familie en vrienden bedanken die ook tijdens de afgelopen vier jaar hebben bijgedragen aan mijn geestelijke welzijn en een belangrijke bijdrage hebben geleverd aan het leven naast mijn promotie. En als laatste Myra. Sinds september gaan we 'geringd' door het leven en samen met jou ben ik klaar voor de volgende uitdaging.

Curriculum Vitae

Aarnoud Roest werd op 26 maart 1976 geboren te Amersfoort. Het VWO diploma werd in juni 1994 behaald aan het Maerlantcollege te Brielle.

In augustus 1994 begon hij aan de studie Scheikunde aan de Universiteit Utrecht en in mei 1995 werd het doctoraal diploma behaald. Tijdens de doctoraalfase werd een groot bijvak bij de sectie Gecondenseerde Materie verricht onder begeleiding van Prof. Dr. J.J. Kelly. Het afstudeeronderzoek werd uitgevoerd bij de sectie Anorganische Chemie onder begeleiding van Prof. Dr. Ir. D.C. Koningsberger. Tijdens zijn studie was hij actief als bestuurs- en commissielid van de Utrechtse Scheikundige Studentenvereniging Proton.

In juni 1999 trad de auteur van dit proefschrift als onderzoeker in opleiding in dienst van de Universiteit Utrecht bij de sectie Gecondenseerde Materie. De meeste resultaten van het onderzoek zijn beschreven in dit proefschrift. Tijdens het promotieonderzoek werd een bijdrage aan het onderwijs geleverd door het begeleiden van practica voor eerste-, tweede-, en derdejaars studenten. Ook werden VWO-scholieren begeleid in het kader van het profielwerkstuk van het examenjaar. De auteur is tevens twee jaar actief (bestuurs)lid geweest van de Debye AiO commissie.